

LOW ENERGY ELECTRON TRANSPORT BY RECONNECTED
MAGNETIC FIELDS AROUND MARS

A DISSERTATION
SUBMITTED TO THE DEPARTMENT OF ELECTRICAL
ENGINEERING
AND THE COMMITTEE ON GRADUATE STUDIES
OF STANFORD UNIVERSITY
IN PARTIAL FULFILLMENT OF THE REQUIREMENTS
FOR THE DEGREE OF
DOCTOR OF PHILOSOPHY

Demet Uluşen

December 2008

© Copyright by Demet Uluşen 2009
All Rights Reserved

I certify that I have read this dissertation and that, in my opinion, it is fully adequate in scope and quality as a dissertation for the degree of Doctor of Philosophy.

(Umran Inan) Principal Adviser

I certify that I have read this dissertation and that, in my opinion, it is fully adequate in scope and quality as a dissertation for the degree of Doctor of Philosophy.

(Ivan Linscott)

I certify that I have read this dissertation and that, in my opinion, it is fully adequate in scope and quality as a dissertation for the degree of Doctor of Philosophy.

(Howard Zebker)

Approved for the University Committee on Graduate Studies.

*This dissertation is dedicated to my parents, Meryem Uluşen and Yakup Uluşen;
and to my sister, Derya.*

Abstract

The solar wind interaction with Mars has been studied extensively through satellite observations and numerical models. From these studies it is well known that Mars lacks a global dipole field nonetheless presents a significant ionospheric obstacle to the solar wind. Moreover, the presence of strong crustal magnetic sources makes the interaction spatially and temporally variable as the planet rotates on its axis and causes local transient particle events. In data from the Mars Global Surveyor orbiter's Electron Reflectometer (MGS/ER) instrument, we discover a new local event of particle enhancements: A seasonal, nighttime clustering of electron flux enhancements at low-energy levels is observed over a localized geographical region in the southern hemisphere of Mars. This enhancement phenomenon is interpreted as the transportation of photoelectrons above the crustal magnetic sources on the dayside to the magnetotail on the nightside of Mars along the lines of the reconnected Interplanetary Magnetic Field (IMF). In order to explain the origin of this phenomenon, a semi-empirical-analytical model is developed to describe the magnetic field configuration of the Martian solar wind interaction. In this model, crustal fields are represented by spherical harmonic expansion, and the perturbed solar wind field is derived from the deviation of a proton flow around a conducting spherical obstacle. Overall magnetic field is obtained from the vector superposition of the crustal fields and perturbed solar wind field. Results of this semi-empirical-analytical model account for the observed electron enhancements. Furthermore, the primary conclusions

of this model are validated by simulations obtained from a self-consistent Magnetohydrodynamic model, allowing for a more accurate and reliable description of the exact nature of the Martian solar wind interaction.

Acknowledgements

First and foremost, I want to express my deep appreciation to my advisors Ivan Linscott and Umran Inan. I would like to thank my principal thesis advisor, Professor Umran Inan, for his wise guidance and steady support in the most difficult times of my PhD life, which have been essential for the completion of this dissertation. I also would like to thank my research advisor, Doctor Ivan Linscott, for his leadership and financial support from the start. I am extremely grateful to him for his patience toward me and his steady encouragement through the years. I will always endeavor to follow his wise approach toward science and research for the rest of my life.

I would like to express my special thanks to Professor Howard Zebker for his invaluable support as a member of my reading committee. I am deeply grateful to Professor Martin Walt for our glimmering discussions and his invaluable comments on my research. I am also grateful to Professor Phillip Scherrer, for serving as chairman, and to Professor John Pauly, for serving as the member of my defense committee. I would especially like to acknowledge Doctor Yingjuan Ma and her colleagues at UCLA, for their generous contributions to my research. I was very fortunate to have the crucial support of the MHD group who dedicated themselves to the development of high fidelity 3D MHD computational simulations.

My special thanks go to Hüsrev Tolga İlhan who has been my officemate for about four years but has always been my friend and mentor during my entire tenure at Stanford. I owe him tremendous thanks for his encouragement and help in almost

any aspect of my life. I will always remember his endless support and goodwill. I am also thankful to all VLF and Radio Science Group members for their assistance and friendships during my entire graduate life in the STARLab at Stanford.

This dissertation would not have been possible without the support and love of my family, which gave me the will for success after strong internal struggles. I would like to express my special thanks to my parents, Meryem Uluşen and Yakup Uluşen, for a lifetime of encouragement and unconditional love. I also thank to my sister, Derya, and my brother-in-law, Hakan, who have been the most patient and the most generous in their belief in my potential for success. Finally, I am grateful to my dearest friends Türev Dara Acar, Özgen Karaer, Enis Kayış, and Ekin Kocabaş and all others for their understanding during the hard times making my life bearable and for their sharing the best times making my life more enjoyable, full of energy and excitement at Stanford.

Demet Uluşen
Stanford, California
December 12, 2008

This research was supported by a grant from the Bosack-Kruger Foundation. I also thank the Planetary Data System for providing the data used in this research.

Contents

Abstract	v
Acknowledgements	vii
1 Introduction	1
1.1 Review of the Current Knowledge of the Martian Solar Wind Interaction	2
1.1.1 The Solar Wind and the Interplanetary Magnetic Field	2
1.1.2 Near Mars Magnetic and Plasma Environment	4
1.1.3 The Interaction of the Solar Wind with Mars	7
1.1.4 The Detailed Description of the Martian Plasma Environment	10
1.1.5 Local Transient Events due to the Crustal Fields	13
1.2 Contributions of this Research	16
1.3 Thesis Organization	17
2 Extraordinary Electron Flux Enhancements	19
2.1 Mars Global Surveyor Data Set	19
2.1.1 Mars Global Surveyor	19
2.1.2 The Magnetometer and the Electron Reflectometer	21
2.1.3 Data Selection	22
2.2 Observation of the Electron Flux Enhancements	22

2.2.1	Characteristics of the Electron Flux Enhancements	27
2.2.2	Distinct Spectra	27
2.2.3	Periodic Nature of the Electron Flux Enhancements	29
2.2.4	Magnetic Field Perturbations	31
2.3	Summary	36
3	Physical Explanation of the Electron Flux Enhancements	38
3.1	Introduction	38
3.1.1	Discussion of the Possible Source Mechanisms	39
3.2	Proposed Source and Transport Mechanism	42
3.2.1	Event Spectra	43
3.2.2	Magnetic Reconnection	44
3.2.3	Estimation of the Draping Direction of the Interplanetary Mag- netic Field	48
3.2.4	Explanation for the Seasonal Nature	54
3.3	Effect of the Sun Illumination on the Local Electron Flux	58
3.3.1	Summary	62
4	Model of the Solar Wind Interaction with Mars	65
4.1	Introduction	65
4.2	Semi-empirical-Analytical Modeling	66
4.3	Mars Global Magnetic Field	68
4.4	Perturbed Solar Wind Magnetic Field	71
4.4.1	Interaction Boundaries	72
4.4.2	Velocity Field of the Proton Flow	76
4.4.3	Streamlines of the Protons around Mars	83
4.4.4	Perturbed Solar Wind Magnetic Field	84
4.5	Results: Combined Global Field	90

5	Magnetohydrodynamic Modeling Results	94
5.1	Introduction	94
5.1.1	MHD Modeling of Solar Wind Interaction with Mars	96
5.2	Model Details	96
5.3	Results	100
5.4	Summary	108
6	Conclusion	109
6.1	Summary of the Contributions	109
6.2	Suggestions for Future Research	112
A	Spherical Harmonic Expansion of Global Magnetic Fields	114
	Bibliography	117

List of Tables

1.1	Typical solar wind parameters near Earth and Mars	3
4.1	Conic function parameter values of <i>Vignes et al.</i> [2000] fits	74
5.1	Transfer integrals for elastic and inelastic collisions	98
5.2	List of chemical reactions and rates considered in the model [Ma et al., 2004]	103

List of Figures

1.1	Spiral structure of the solar wind.	2
1.2	Orthographic projections of the three components of the magnetic field (B_r , B_ϕ , B_θ) at a nominal 400 km mapping orbit altitude, viewed from 30° S and 180° E (after <i>Connerney et al.</i> [2001]).	5
1.3	Density profiles of the major charged particles in the Martian ionosphere (after Shinagawa, 2000).	6
1.4	Major regions and boundaries in the Martian plasma environment (after Bagenal, 2000).	9
1.5	Detailed structure of the interaction of Mars with the solar wind and major regions and boundaries in the interaction environment (after Nagy et al., 2004).	11
2.1	(a) Mars Global Surveyor (MGS) spacecraft. (b) The orbit geometry of MGS in different phases of the mission.	20

2.2	The geometry of MGS orbit and the orientation of Mars in the Sun-State coordinate system at the time of an enhancement event (MGS MAG/ER data recorded during this event is shown in Figure 2.3). The thick arrowed line shows the Mars rotation axis which is tilted towards the Sun for this case (northern hemisphere is in summer). The dashed red line indicates the orbit of MGS, and the marked region on the orbit shows the region where enhancement is observed. The color scale maps the radial component of the crustal magnetic fields observed at 400 km altitude and projected onto the Martian surface. (a) View from the nightside. (b) View from the dawnside in order to show the relative position of the strong crustal sources with respect to enhancement site.	23
2.3	An example of a significant electron flux enhancement observed over the region between $30^{\circ}\pm$ and $120^{\circ}\pm$ E, at $\sim 70^{\circ}\pm$ S. The horizontal axis represents the time evolution as MGS moves from north to south on the nightside over the region of interest. The top panel is the logarithm of the omnidirectional electron fluxes at 19 energy levels, six of which are indicated on the curves, (the energy levels from top (10 eV) to bottom (20 keV) with energy resolution of 25%). The bottom plot shows the magnetic field components in the Sun-State coordinate system at the time MGS records the significant enhancement.	24
2.4	The map of the percentage of the significant enhancements in the 61 eV energy band among all nightside observations over the southern hemisphere superimposed on the contours of the radial component of the crustal magnetic fields. This map represents the general characteristics of all low energies below a few hundred eV.	26

2.5	Comparison of electron energy spectra of two different regions in each figure obtained from the MGS ER data. (a) The red line shows the averaged spectrum of the significant enhancements observed between $30^\circ \pm$ and $120^\circ \pm$ E at $\sim 70^\circ \pm$ S, and the blues line shows the typical tail spectrum observed in the region of absent of crustal fields. (b) The red line shows the averaged spectrum of the significant enhancements observed between $30^\circ \pm$ and $120^\circ \pm$ E at $\sim 70^\circ \pm$ S and the green line shows the averaged spectrum of aurora observed at around $150^\circ \pm$ E, $70^\circ \pm$ S.	28
2.6	Periodic nature of the electron enhancements. (a) Temporal distribution of the occurrence of the electron enhancements with respect to time. (b) Seasonal variation of the occurrence of the electron enhancements with respect to the areocentric longitude of the Sun, L_s (Martian northern hemisphere seasons). (Note: Occurrence of the enhancements selected by criteria detailed in Section 2.2)	30
2.7	Fourier transform of the temporal distribution of the enhancements. The curve indicates the normalized spectral magnitude of the 116 eV omnidirectional electron flux, obtained from the Fourier transform and plotted as a function of fluctuation period. The 116 eV energy level lies almost near the geometric center of the energy band between 11 eV and a few hundred eV, over which the enhancements are observed. This energy band represents the general characteristics of the entire band.	31
2.8	Averaged magnetic field components in the Sun-State coordinate system, obtained using the MAG data recorded at the times of enhancements.	32

2.9	An example model of current sources at the time of an enhancement observed on the 196th day of 2000. a) The view is in the SS coordinate system. Current dipoles are displayed in blue and parameters were estimated using the MGS MAG data recorded along the portion of the orbit, marked in green. The red ring at the bottom is the $65^\circ \pm$ S parallel at an altitude of 400 km. The red rectangle on the ring represents the crustal magnetic fields at $\sim 150^\circ \pm$ E, $65^\circ \pm$ S. b) Zoomed-in view of the current dipoles of the model example on the 196th day of 2000.	35
3.1	(a) MGS crossing of a current sheet at Mars. Draping IMF carries photoelectrons from the ionosphere to the tail and causes magnetic reversals on the tail. (Adapted from [<i>Halekas et al.</i> , 2006]) (b) The interaction of solar wind plasma with the dayside ionosphere produces clouds of plasma which may become detached and swept downstream in the ionosheath or may remain attached to the ionopause. (Adapted from [<i>Brace et al.</i> , 1982]).	40
3.2	Relative positions of Mars, the MGS orbit, the crustal sources, and the draped field lines in the SS coordinate system at the time an enhancement is observed. The first panel shows the side view while the second panel shows the view from an angle on the nightside. Reconnected and draped IMF lines carry the photoelectrons from the dayside to the nightside, and a current form in the tail. The MGS orbit traverses the current obliquely on the nightside. The marked region shows the portion of the MGS orbit over which the enhancement is observed and the magnetic reversals are recorded in the middle of this marked region.	42

3.3	2-D steady-state interpretation of the reconnection process. (a) Convection of oppositely directed field lines. (b) Reconnection of the field lines in the diffusion region. (c) Changed magnetic topology after reconnection.	46
3.4	Definition of the IMF angle. The θ and ϕ components of the local magnetic field are shown. The dashed line indicates the MGS orbit, and the black rectangular box covers the portion of the orbit from 50° to 60° N. (Adapted from [<i>Brain et al.</i> , 2006])	50
3.5	The direction and magnitude of the draped IMF obtained from the MGS MAG data between $50^\circ \pm$ and $60^\circ \pm$ N. a) Mean of the draped IMF angle at each pass during six year time period. The red dots mark the passes on which the significant enhancements are observed over the region of interest. b) The histogram of the mean angles obtained from all observations in six year time period (blue curve), and the histogram of the mean angles obtained from the observations at the times of the enhancements (red curve). c) The histogram of the mean magnitude of the draped IMF obtained from all observations in six year time period (blue curve), and the histogram of the mean draped IMF magnitude obtained from the observations at the times of enhancements (red curve).	51
3.6	Maps of the radial component of the Martian crustal magnetic fields at 400 (+/- 30) km altitude, and colorbar scaled to (+/-)220 nT. (After <i>Connerney et al.</i> [2001])	53

3.7	Variability of the occurrence of the reconnection conditions and the enhancements with respect to time (years). a) Histogram of the passes when the reconnection conditions were met, and the significant enhancements were expected. b) Histogram of the passes when the significant enhancements were observed. c) Common points of a) and b) indicating the passes on which reconnection was expected and an enhancement was observed.	54
3.8	Variability of the occurrence of the reconnection conditions and the enhancements with respect to Martian seasons (L_s). a) Histogram of the passes when the reconnection conditions were met, and the significant enhancements were expected. b) Histogram of the passes when the significant enhancements were observed. c) Common points of a) and b) indicating the passes on which reconnection was expected and an enhancement was observed.	55
3.9	a) The solar zenith angles of the potential crustal sources at the time of enhancements. b) The temporal distribution of the midlatitudes of the enhancements (red dots) and of the latitudes of the source region (blue dots) at the times of the enhancements, in the SS coordinate system.	57

3.10	Temporal electron flux distribution over the closed crustal fields between $180^\circ \pm$ and $210^\circ \pm$ E at $\sim 65^\circ \pm$ S. a) The logarithm of the omnidirectional electron fluxes at 19 energy levels (logarithmically spaced from 10 eV (top) to 20 keV (bottom) with an energy resolution of 25%). b) Zoomed-in view of the electron flux during CY 2003. In Sun shadow, the electron flux drops to or below instrument background level revealing plasma voids (region marked under "shadow"). As the region is illuminated by the Sun, electron fluxes increase gradually filling the voids with photoelectrons (region marked under "sunlit"). "Spikes" seen in shadow are either due to the ambient electrons that can reach the voids such as aurora over nearby cusp regions or the disturbances driven by the transient solar ejections.	59
3.11	Temporal electron flux distribution over the geographical region for the significant enhancements (between $60^\circ \pm$ and $90^\circ \pm$ E at $\sim 70^\circ \pm$ S.) a) The logarithm of the omnidirectional electron fluxes at 19 energy levels (logarithmically spaced from 10 eV (top) to 20 keV (bottom), with an energy resolution of 25%). Spike-like outgrowths at the low energy levels are attributed to the significant enhancements. The enhancements are mostly observed in shadow, and there is a gradual increase in the typical nightside electron flux levels as the region starts to see the Sun (area marked as "sunlit") b) Expanded view of the estimated draped IMF angle during CY 2003 (from Figure 6a). The red dots mark the enhancements. c) Expanded view of the electron flux during CY 2003. The enhancements are recognized by two orders of magnitude increase at the low energy levels and occur on a nearly 25 day periodic timescale coinciding with the westward alignment of the draped IMF.	61

4.1	Two components of the magnetic field around Mars, resulting from the Martian solar wind interaction: Mars global field and Perturbed solar wind field. The average magnetic field configuration is derived from the vector superposition of these two fields.	67
4.2	Contours of the radial component of the crustal magnetic fields over a spherical surface at 400 km altitude at Mars, which is obtained using the coefficients spherical harmonic expansion model of <i>Cain et al.</i> [2003].	70
4.3	Bow shock and MPB fits in MSO coordinate at Mars obtained from MGS observations.	75
4.4	Axial symmetry in the velocity model with respect to the x -axis, which points at the Sun.	77
4.5	Relative velocity magnitude of the flow with respect to solar wind speed.	79
4.6	Direction of the flow velocity around Mars.	82
4.7	Path of the protons around Mars in the defined velocity field. Different colors represent the streamlines in different plasma regions: Red streamlines pass through the bow shock and remain in the magnetosheath. The blue lines pass through first the bow shock and then MPB and remain below the MPB. Similarly, green lines pass first the bow shock and then MPB but these lines are very close to the planet as they enter the magnetosheath at a point that is very close to subsolar point (a) View of the streamlines from the side of the planet. (b) View of the same streamlines in (a) from an angle.. . . .	83
4.8	Draping perturbed solar wind field lines around Mars.	87
4.9	Magnitude of the perturbed solar wind field around Mars over the xz plane in the MSO coordinate system.	89

4.10	Magnitude of the magnetic field over a surface formed by the field lines in Figure 4.8.	90
4.11	Two field line topologies shown in blue and magenta, which form the overall magnetic field around Mars resulting from the Martian solar wind interaction. (a) The blue lines are the perturbed solar wind field lines, obtained from <i>Kallio</i> 's model. The purple field lines are Mars global magnetic field lines, obtained from <i>Cain</i> 's spherical harmonic expansion model. Color indicates the map of the crustal fields at 400 km altitude and projected to the Martian surface. (b) Zoomed-in view of (a) over the potential crustal sources.	92
4.12	Overall magnetic field lines obtained from the vector superposition of Mars global field and perturbed solar wind field. Color indicates the map of the crustal fields at 400 km altitude and projected to the Martian surface. (b) Zoomed-in view of (a) over the potential crustal sources.	93
5.1	Strength of the calculated magnetic field on the equatorial (xy plane) and on the noon-midnight (xz plane) planes.	104
5.2	Strength of the calculated velocity field on the equatorial (xy plane) and on the noon-midnight (xz plane) planes.	105
5.3	The calculated ion and electron density profiles from the model results for the subsolar 0° N, 45° N, 45° S, and 70° N.	106

5.4	The magnetic field lines in black are drawn over the proposed crustal sources including the geometry of MGS orbit, orientation of Mars and relative position of the crustal sources for the case the model is run. The black solid line shows the Mars rotation axis which is tilted by 25° toward the Sun. The purple circle indicates the orbit of MGS, and the region marked on the orbit shows the enhancement observation site. The color map is the radial component of the crustal magnetic fields calculated from the model and plotted over a spherical surface at 300 km altitude.	107
-----	-------------------------------------------------------------------------------------------------------------------------------------------------------------------------------------------------------------------------------------------------------------------------------------------------------------------------------------------------------------------------------------------------------------------------------------------------------------------------------------------------------------------------------------------------------------------------------------------------------------	-----

Chapter 1

Introduction

The purpose of this dissertation is to report a novel local event of energetic particle enhancements observed over a localized geographical region on the nightside of Mars and provide a suitable physical explanation for its occurrence. This particle enhancement is one of the local events observed in the data from the Mars Global Surveyor orbiter's Magnetometer and Electron Reflectometer instrument (MGS MAG/ER) and is induced by strong crustal magnetic sources over the Martian surface in the course of the interaction of the planet with the solar wind. The present chapter begins with a background on the solar wind and the Interplanetary Magnetic Field (IMF) and follows with a summary of the current knowledge of the near plasma and magnetic environment of Mars. A review of the interaction of Mars with the solar wind is included to introduce the contributions of this dissertation. For a detailed review of the Martian environment from past and recent studies see, for example, *Luhmann and Brace* [1991], and *Nagy et al.* [2004].

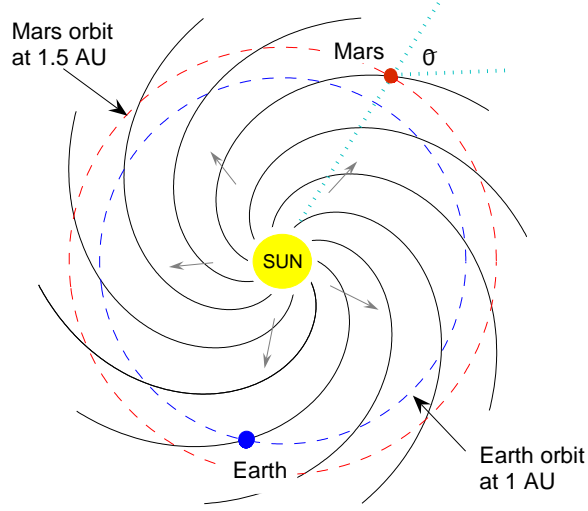


Figure 1.1: Spiral structure of the solar wind.

1.1 Review of the Current Knowledge of the Martian Solar Wind Interaction

1.1.1 The Solar Wind and the Interplanetary Magnetic Field

The solar wind is the continuation of the expansion of the Sun's outer atmosphere (corona) in interplanetary space [Neugebauer and Snyder, 1966] (see Figure 1.1). It is a fully ionized plasma composed of approximately equal numbers of ions and electrons. The ions consist predominantly of protons (90% H^+) and a small percentage of alpha particles ($\sim 10\%$ He^{++}). The average expansion speed of these charged particles is approximately 400 km-sec^{-1} at a few solar radii distances from the Sun, where it becomes a supersonic flow. In other words, the velocity of the flow is greater than the velocity of any plasma wave that can be generated in the solar wind, i.e., the mach number is greater than one. This property of the solar wind plasma is important for its interaction with other solar system bodies, as discussed later.

Table 1.1: Typical solar wind parameters near Earth and Mars

	Unit	Min (Earth)	Max (Earth)	Average (Earth)	Average (Mars)
Velocity	km-sec ⁻¹	200	900	400	400
Density	ion-m ⁻³	4 10 ⁵	10 ⁸	6.5 10 ⁶	4 10 ⁶
Magnetic field	nT	0.2	80	6	3
Parker spiral angle	degrees	0	90	45	53
Electron temperature	K	5 10 ³	10 ⁶	3 10 ⁵	3 10 ⁵
Proton temperature	K	3 10 ³	10 ⁶	5 10 ⁴	5 10 ⁴

Other major parameters that characterize the solar wind and its interaction with the solar system bodies are density, velocity, magnetic field strength, Parker spiral angle, and particle temperatures. Typical values of these parameters near Earth, with their range, are listed in Table 1.1. Variations in these parameters may be in response to changes in the solar cycle, heliographic latitude, heliocentric distance, and sudden changes in solar activity, such as solar flares and coronal mass ejections. For comparison, the values of these parameters near Mars are included in the same table [Luhmann and Brace, 1991].

$$\beta = \frac{\text{Kinetic energy density}}{\text{Magnetic energy density}} = \frac{n(\frac{1}{2}mv^2)}{B^2/2\mu_0} \quad (1.1)$$

The fundamental measure of a magnetic field's effect on a plasma is the *plasma beta*, β , which is defined as the ratio of the thermal energy density to the magnetic energy density (Equation 1.1). The average value of the solar wind plasma beta, obtained by using the parameters in Table 1.1, is about 60 at Earth and 100 at Mars. Since the beta value is much greater than one, the dominant mechanism is the plasma flow. In other words, the magnetic field lines are frozen into the plasma and carried outward from the Sun by the streaming charged particles. At far distances, this magnetic field accompanying the plasma motion forms an Archimedes spiral

structure due to the Sun’s rotation [Parker spiral; *Parker*, 1963], (see Figure 1.1), and this weak magnetic field is called the Interplanetary Magnetic Field (IMF). As seen in Figure 1.1, the angle between the radial direction and the field line at a point varies with distance from the Sun (the angle θ is $\sim 45^\circ$ at Earth and $\sim 53^\circ$ at Mars). In addition to this primary component in the ecliptic plane, there is also a small component normal to ecliptic plane, which also significantly influences the solar wind’s interaction with obstacles in its way. The interaction of the solar wind with the obstacles in the solar system will be detailed in the following sections.

1.1.2 Near Mars Magnetic and Plasma Environment

The initial magnetic field observations from early missions to Mars clearly showed that the magnetic moment of any likely internal dipole can not exceed $2.5 \cdot 10^{22} \text{ G}\cdot\text{cm}^{-3}$. However the existence of an internal magnetic field remained controversial for many years [*Dolginov et al.*, 1976; *Luhmann et al.*, 1992]. In 1998, the magnetic vector measurements of Mars Global Surveyor revealed that Mars has no detectable internal dipole field but has strong crustal magnetic sources on its surface [*Acuña et al.*, 1998]. These crustal sources are localized mainly over the southern hemisphere, and their magnitudes can reach 200 nT at 400 km altitude [*Connerney et al.*, 1999]. Figure 1.2 illustrates the map of the three components of these crustal magnetic sources over a spherical surface at 400 km altitude, obtained by *Connerney et al.* [2001] using the MGS magnetometer data. In their work, *Connerney et al.* [2001] concluded that crustal magnetizations on Mars were at least an order of magnitude greater than those observed on Earth [*Connerney et al.*, 2001], and that they are strong enough to locally modify the interaction of the planet with the solar wind [*Crider et al.*, 2003; *Nagy et al.*, 2004]. Today, there are many theories for the absence of a detectable global magnetic field and presence of crustal sources on Mars. The most commonly accepted one is that Mars had a strong dynamo in the past, which is no longer active today,

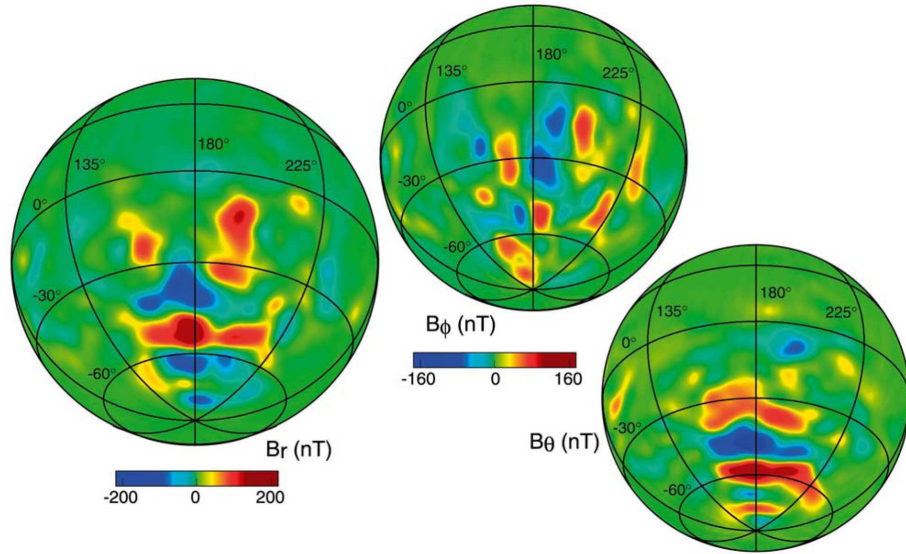


Figure 1.2: Orthographic projections of the three components of the magnetic field (B_r , B_ϕ , B_θ) at a nominal 400 km mapping orbit altitude, viewed from 30° S and 180° E (after *Connerney et al.* [2001]).

and that the strong crustal sources are the remnant magnetization of the surface rock on Mars produced when a strong dynamo-generated global field was present.

Mars has a very thin atmosphere. The uppermost boundary of the Martian atmosphere can be encountered at approximately 100–110 km altitude, above which the gas becomes sparse. Due to its thin nature, the atmosphere has a very low pressure on the surface (less than 1% of the average surface pressure on Earth). In 1976, the Viking 1 and 2 landers characterized the composition of the Martian atmosphere as 95.3% carbon dioxide, 2.7% nitrogen, and 1.6% argon, with smaller amounts of oxygen (0.15%) and water vapor (0.03%). Ionization of the particles in the neutral atmosphere due to solar radiation creates a conducting layer on the dayside of the planet and forms the Martian ionosphere.

The ionosphere of Mars has been studied through a large number of electron density profiles obtained from radio-occultation observations by the early US and

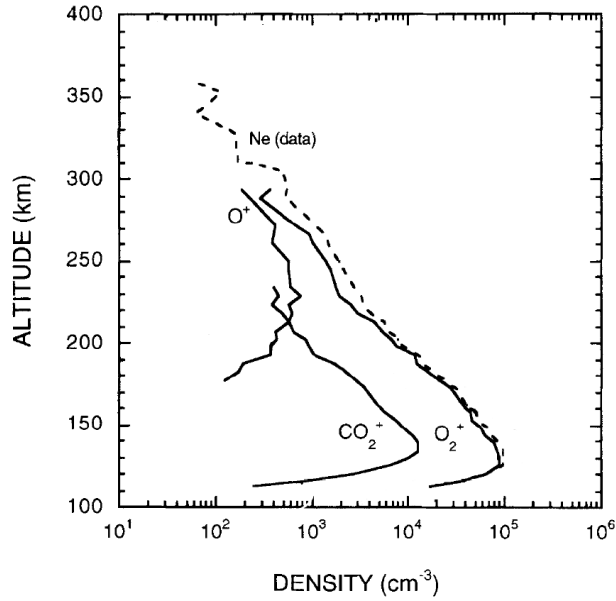


Figure 1.3: Density profiles of the major charged particles in the Martian ionosphere (after Shinagawa, 2000).

Soviet missions, Mariner 4, 6, 7, and 9; Mars 2, 4, and 6 [Kilore *et al.*, 1965; Fjeldbo *et al.*, 1996], but the most comprehensive and the only in-situ data has come from the Viking 1 and 2 landers [Hanson *et al.*, 1977]. The most recent ionospheric data is from Mars Pathfinder, Mars Global Surveyor, and Mars Express probes.

The in-situ density measurements of the O^+ , O_2^+ , CO_2^+ ions and electrons from the Retarding Potential Analyzer (RPA) on the Viking landers are shown in Figure 1.3. As inferred from these profiles, the Martian ionosphere begins at an altitude of approximately 110–120 km, and a typical value for the peak plasma density is $\sim 2 \times 10^5 \text{ cm}^{-3}$ at an altitude of 135 km. The principal daytime ion component is O_2^+ throughout the ionosphere because of the quick conversion of CO_2^+ to O_2^+ , where O_2^+ is produced by the photo-ionization of CO_2^+ [Hanson *et al.*, 1977]. At 300 km altitude, however, O^+ becomes comparable to O_2^+ . The ion profiles below 200 km are the typical result of the photochemical processes, but between 170 and 200 km

altitudes, the transport processes become dominant on the dayside of Mars [*Hanson et al.*, 1977; *Chen et al.*, 1978; *Fox*, 1993]. The only observations of the nightside ionosphere of Mars are from the radio-occultation experiments performed by Mars 4 and 5, as well as those of the Viking orbiters, which recorded an electron density peak of $\sim 5 \times 10^3 \text{ cm}^{-3}$ at 110–130 km altitudes. This minimal nightside ionosphere may be due to either the extension of the dayside ionosphere to the nightside or some direct nighttime ionization source.

1.1.3 The Interaction of the Solar Wind with Mars

The nature of the solar wind interaction with a solar system body is determined by the type of the obstacle that the body presents to the solar wind. There are two major types of obstacles in our solar system: magnetized bodies (such as our planet Earth) and non-magnetized bodies (such as Venus and Moon). For the magnetized bodies, the primary obstacle is the planet's global magnetic field, which presents a strong magnetic pressure to the solar wind flow. In this type of interaction, most of the solar wind is deflected around this magnetic barrier, forming a cavity inside. This cavity is called "the planetary magnetosphere," into which some solar wind plasma leaks, and the planetary magnetic field dominates the behavior of charged particles. On the dayside, the boundary of the magnetosphere is controlled primarily by the balance between the planet's magnetic field pressure and the solar wind ram pressure [*Spreiter and Alksne*, 1969]. On the nightside, the boundary is controlled by the stretch of the solar wind magnetic field lines downstream from the planet, which also form the magnetotail [*Van Allen and Bagenal*, 1999].

For non-magnetized bodies, the nature of the interaction with the solar wind is determined by the electrical conductivity of the obstacle. If the planet has an ionosphere, temporal variations in the direction and magnitude of the solar wind magnetic field induces electrical currents in this conducting region. In response to

these variations, the induced currents create magnetic field forces that exclude the solar wind particles and divert their incident flow [Luhmann, 1986]. By this diversion of the solar wind flow, the interplanetary magnetic field drapes around the planet and stretches out downstream, again forming a magnetotail [Russell and Vaisberg, 1983]. The general structure of this interaction is very similar to a magnetosphere for the magnetized bodies, and it is called an "induced magnetosphere." For non-magnetized obstacles without an ionosphere, such as the Earth's Moon, the solar wind interacts directly with the surface, where it is absorbed since there is not a sufficient current to deflect it. Therefore, a wake, or region absent of plasma, is formed close to the nighttime hemisphere downstream from the Moon, and at greater distances the solar wind particles fill the wake as they flow towards the center of the magnetotail.

The obstacle type that Mars presents to the solar wind was debated for many years [Russell *et al.*, 1984; Dolginov, 1986]. However, from the magnetic field measurements of MGS, it is now known that Mars lacks a large scale global magnetic field but has a substantial ionosphere, and thus it presents an ionospheric obstacle to the solar wind (i.e., a Venus-like obstacle) [Phillips and McComas, 1991; Acuña *et al.*, 1998; Cloutier *et al.*, 1999; Nagy *et al.*, 2004]. Figure 1.4 illustrates the general structure and major plasma regimes of this interaction. Due to the supersonic nature of the solar wind flow, an outermost boundary is formed on the dayside, called a bow shock. At this boundary, the solar wind flow decelerates, becomes heated, and is deflected around the obstacle, such as Mars [Russell, 1993]. The innermost boundary detectable in this interaction is the ionopause, characterized by a transition from hot, dense, solar wind dominated plasma to relatively cold, heavy ionospheric plasma. In between the bow shock and the ionopause, the interplanetary magnetic field piles up and drapes around the conducting surface formed by the ionosphere, as seen in Figure 1.4. All three boundaries, shown in Figure 1.4, are typical for the solar wind interaction with any non-magnetized obstacle having a substantial ionosphere. What makes Mars most

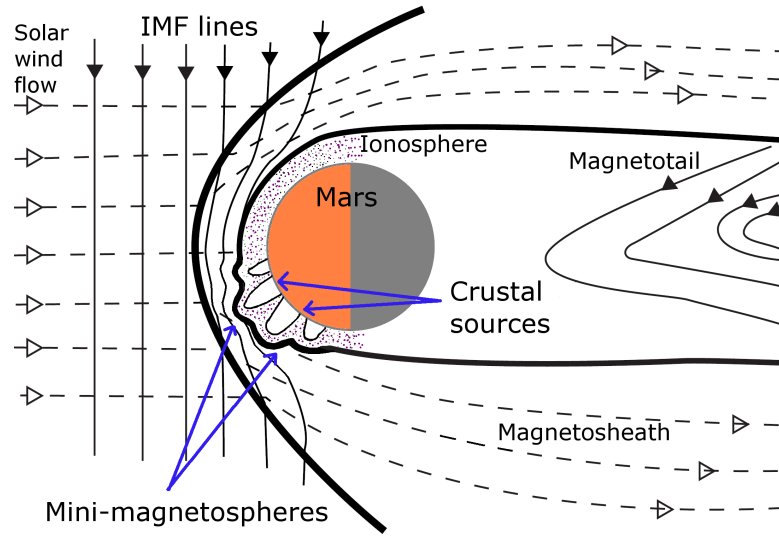


Figure 1.4: Major regions and boundaries in the Martian plasma environment (after Bagenal, 2000).

interesting and unique among these obstacles are its crustal magnetic sources, which are strong enough to cause local deviations from the typical interaction structure. As Mars rotates on its axis, these crustal sources present a variable obstacle to the solar wind and modify the interaction locally. The mini-magnetospheres above the crustal sources illustrated in Figure 1.4 indicate the deviation for Mars from the typical ionospheric interaction. In fact, these crustal sources yield many dynamic and transient particle events near, as well as far away from, these local structures. The exact nature and dynamics of this interaction are still not fully understood. Many fundamental questions about the generation of these events can be addressed with the data available from MGS magnetometer and electron reflectometer instruments.

In this dissertation, we study local particle events due to the crustal sources as revealed in the MGS magnetic field and electron flux data, and focus on a novel local particle event observed in this data and its physical explanation. The contributions of this research are summarized in the following section. Detailed information on

these local structures and further transient events induced by these crustal sources are addressed in the following chapter.

1.1.4 The Detailed Description of the Martian Plasma Environment

As stated previously, Mars lacks a global magnetic field but has a substantial ionosphere. Although the planet has strong local crustal magnetic sources on its surface, these local sources are not strong enough to influence the solar wind interaction with the planet on a global scale. Therefore, the general characteristics of an ionospheric obstacle dominate the interaction of the solar wind with Mars. Figure 1.5 illustrates typical plasma regions and boundaries observed in an ionospheric type of interaction.

As seen in Figure 1.5, the bow shock is the first boundary. At this boundary the supersonic solar wind flow becomes subsonic, and plasma begins to deflect around the Martian obstacle. Upstream of the bow shock, the flow is highly turbulent. As the plasma passes the boundary, it decelerates and becomes heated. The average terminator and subsolar stand off distances of the bow shock is calculated as $1.7R_M$ and $2.6R_M$, respectively, by *Vignes et al.* [2000] using 450 Martian bow shock crossings of MGS ($R_M=3390$ km). In their study, the shock position was found to be highly variable. One reason for this variation in the bow shock position is mass loading associated with the electric field of the IMF. On the other hand, solar activity does not play a major role in this variation, and it is not directly correlated with the relative location of the crustal magnetic sources with respect to the Sun [*Vignes et al.*, 2002]. The second boundary is called the Magnetic Pile-up Boundary (MPB) which sharply separates the magnetosheath and Magnetic Pileup Region (MPR). Within the magnetosheath significant mass-loading occurs, and low amplitude and turbulent magnetic fields dominate. On the other hand, in the MPR, planetary ions dominate

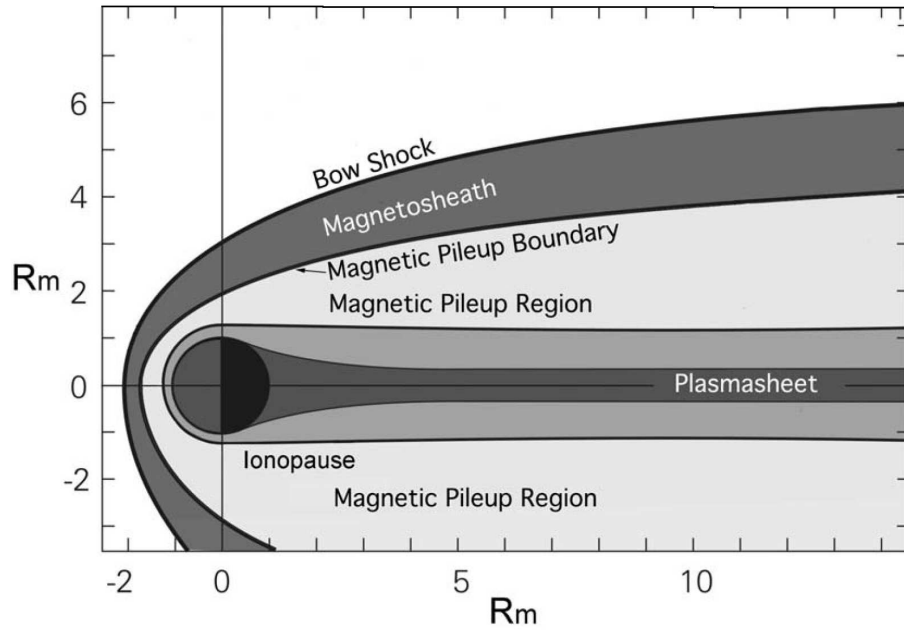


Figure 1.5: Detailed structure of the interaction of Mars with the solar wind and major regions and boundaries in the interaction environment (after Nagy *et al.*, 2004).

and the solar wind magnetic fields pile up as they drape about the ionosphere [Crider *et al.*, 2001 and 2002] (similar at Venus [Zhang *et al.*, 1991]). Due to this piling up of the field lines at the MPB, the magnetic field magnitude increases by two or three times of its magnetosheath value. Moreover, at the MPB, the magnetic field fluctuations decrease and are accompanied by magnetic field rotation, and the solar wind proton density decreases as planetary ion density increases. The average stand-off distance of the MPB was found to be about $1.3R_M$ at the subsolar point, and about $1.5R_M$ at the terminator from 488 MPB crossings of MGS [Vignes *et al.*, 2000]. However, the location of the MPB is highly variable. Crider *et al.* [2002] showed that the MPB position depends on the location of the strongest crustal magnetic fields with respect to the Sun. The variation of the MPB location may also be due to plasma processes associated with mass loading, such as the variation of the local convective electric field. On the dayside, the MPR is bounded by the ionosphere; and

on the nightside, it is bounded by a magnetotail and stretches far downstream from the planet.

The lowermost detectable boundary on the dayside of Mars is the ionopause where the planetary pressure is balanced by the total solar wind pressure. From in-situ measurements of Viking 1–2 landers, it is known that the ionospheric thermal pressure is insufficient to balance the total solar wind pressure when the dynamic component of the solar wind pressure is high or solar radiation is low. During these times, magnetic fields induced in the Martian ionosphere supply the sufficient pressure to the ionospheric thermal pressure and balance the total solar wind pressure. The typical altitude of this balance is 380 km [Mitchell *et al.*, 2001] but locally, the crustal magnetic fields modify the topology of the ionosphere and change the location of the ionopause. Another boundary, called the photoelectron boundary (PEB), may be collocated with the ionopause [Mitchell *et al.*, 2001]. This boundary is identified by a transition in the energetic electron flux from shocked solar wind electrons above the boundary to ionospheric photoelectrons below the boundary [Mitchell *et al.*, 2001].

Phobos-2 and MGS observations showed that similar to Venus, an induced magnetotail forms on the night side of Mars where two oppositely directed lobes are aligned away from Mars on the nightside as result of draping of the IMF lines around the ionospheric obstacle. Thus, the orientation of the lobes is determined by the orientation of the upstream interplanetary magnetic field [Yeroshenko *et al.*, 1990; Schwingschuh *et al.*, 1992; Crider *et al.*, 2002]. From the same measurements, the diameter of the Martian magnetotail was found to be $4.2R_M$ at $2.3R_M$, and $7.6R_M$ at $10R_M$ distance away from Mars on the Mars-Sun line [Verigin *et al.*, 1993]. However, it is also known that the magnetotail thickness varies significantly as the crustal sources move near the terminator [Verigin *et al.*, 2001]. Although these observations are not enough to accurately describe the effects of the crustal magnetic sources in the tail, Mitchell *et al.* [2001] proposed the formation of magneto-cylinders on the nightside

based on the MGS observations. These cylinders are the stretch of the closed field lines along the tail which excludes solar wind plasma traveling toward the magnetotail from the nightside neighboring regions and dayside ionosphere. Moreover, in 1989, using the Phobos 2 data *Rosenbauer et al.* [1989] discovered a plasma sheet in the Martian magnetotail, which consists mainly of planetary heavy ions [*Verigin et al.*, 1991b; *Lundin and Dubinin*, 1992]. Observation of nearly radial magnetic fields on the nightside of Mars implies the existence of nightside ionospheric holes at Mars similar to those on Venus [*Marubashi et al.*, 1985]. Ionospheric thermal ion flow towards tail is also observed in the Martian magnetotail, which may be another important escape mechanism at Mars [*Ma et al.*, 2002; 2004].

In the next subsection, the general plasma regions and boundaries around Mars are introduced to describe the global picture of the Martian interaction with the solar wind. Next, the local deviation from this global structure due to strong crustal sources are discussed in detail.

1.1.5 Local Transient Events due to the Crustal Fields

The presence of local strong crustal sources makes Mars unique among the other solar system bodies in regard to the interaction of the planet with the solar wind. These local but fairly widespread crustal magnetic sources may globally influence on the solar wind interaction. However, in this section our focus is on the local transient events induced by these sources.

Initial investigations of the nature of the crustal sources revealed that due to their strip-like structure they form closed field lines over the regions of alternating sign (see Figure 1.2). When these regions face sunlight, they are filled with photoelectrons [*Mitchell et al.*, 2001]. At the same time, they increase the total pressure locally presented to the solar wind and create an asymmetric obstacle. These localized crustal magnetic field dominated regions are called 'mini-magnetospheres', which

push the solar wind up to 1000 km altitude [*Mitchell et al.*, 2001; *Vignes et al.*, 2002; *Ma et al.*, 2002; *Krymskii et al.*, 2003; *Brain et al.*, 2003]. When the same regions rotate into shadow, the photoelectrons disappear as a result of recombination and atmospheric absorption, forming "plasma voids" comparable in size to the closed field regions. These voids are effectively cut off from solar wind plasma that is traveling towards to the magnetotail from the sunlit hemisphere [*Mitchell et al.*, 2001]. Furthermore, the outermost lines of the closed crustal magnetic fields should be able to reconnect with IMF lines, which drape over the mini-magnetospheres. During reconnection, the closed field lines become open, connecting the Martian surface with the solar wind magnetic field near the local sources, resulting in changes in the magnetic topology, similar to cusp-like regions at Earth [*Harnett et al.*, 2005; *Halekas et al.*, 2006]. The presence of cusp-like structures at Mars suggests that aurora occurs near these sources. In other words, near these sources sheath particles precipitate at lower altitudes penetrating into the ionosphere and neutral atmosphere; and cause heating and ionization in the atmosphere [*Ness et al.*, 2000; *Brain et al.*, 2003]. Auroral activity was discovered inside the ultraviolet spectrometer on board Mars Express by *Bertaux et al.* [2005]. *Brain et al.* [2006] correlated auroral emissions with the electron flux enhancements in the vicinity of the crustal sources at energy levels between 100 eV and 2.5 keV suggesting the reconnection of crustal magnetic fields with the draped IMF [*Mitchell et al.*, 2001; *Krymskii et al.*, 2002; *Brain et al.*, 2003].

The interaction of the crustal sources with the solar wind results in other transient events at Mars, such as local electron or ion density fluctuations [*Krymskii et al.*, 2002; *Soobiah et al.*, 2006]. Recent studies of *Ferguson et al.* [2005] and *Halekas et al.* [2006] showed that current sheets form in the Martian tail, which even extend to the altitudes of MGS (~ 400 km). Furthermore, these current sheets induce significant magnetic field perturbations in their neighborhood, and their strength may reach 25 nT. *Dubinin et al.* [2006] reported permanent localized strip-like structure of plasma densities on a

number of Mars EXpress (MEX) orbits, where the structures were aligned tailward of the terminator plane and composed of magnetosheath-like electrons and planetary ions. These structures affect the plasma inflow to the magnetosphere and planetary plasma transport to the tail [Dubinin *et al.*, 2006b]. Similarly, *Frahm et al.* [2006] reported photoelectron peaks recorded by the MEX EElectron Spectrometer (ELS), implying electron flows away from Mars near the terminator and in the tail. These flows are probably produced on the dayside and carried to the tail by the field lines [Frahm *et al.*, 2006b; Fedorov *et al.*, 2006].

Mars does not have a constant, stable, and permanent region of confined radiation like the Earth's radiation belts, but the discovery of the strong crustal magnetic sources raised the possibility that local regions of magnetic confinement might exist over the crustal sources. Based on the MGS MAG/ER observations, *Mitchell et al.* [2001] reported the possibility of the trapping of the ionospheric plasma in the magneto-cylinders which are effectively shielded from the solar wind. Using 326 selected electron density profiles of the Martian ionosphere derived from radio occultation data, *Krymskii et al.* [2004] discussed the electron confinement in the large-scale mini-magnetospheres. The variations in the electron density peak imply that electrons are hotter, and neutral atmosphere is cooler inside a large scale mini-magnetosphere than outside. In their work, this difference is explained as the shielding of the neutral atmosphere by the strong crustal sources from the solar wind preventing its heating and by the confinement of the hotter photoelectrons in the closed field lines. However, in the open configuration of the magnetic field lines in the small-scale magnetospheres near the cusp-like regions, photoelectrons are not trapped [Krymskii *et al.*, 2003; 2004].

In fact, these crustal sources yield many dynamic and transient particle events near as well as far away from these local structures. The exact nature and dynamics of this interaction are still not fully understood. Many fundamental questions about

the generation of these events can be addressed with the data available from MGS magnetometer and electron reflectometer instruments. In this dissertation, we study these local events due to the crustal sources using MGS magnetic field and electron flux data and focus on a novel local particle event we observe in this data and its physical explanation. The summary of the contributions about this research are listed briefly in the following section.

1.2 Contributions of this Research

The major contributions of this dissertation are summarized as follows:

1. Discovered nighttime low energy electron flux enhancements over a local geographical region in the southern hemisphere of Mars.
2. Characterized the nature of these electron flux enhancements:
 - (a) Electron enhancement events are clustered over a specific local region in the southern hemisphere on the nightside of the planet.
 - (b) Electron flux enhancements exhibit periodicities on both a 25 day time scale and a Martian season scale.
 - (c) Electron flux enhancements are accompanied by magnetic field perturbations recorded in the vicinity of the enhancement observation site.
3. Interpreted the observed electron flux enhancements as the transportation of the photoelectrons above the crustal sources on the dayside to the magnetotail on the nightside by the reconnected interplanetary magnetic fields.
4. Developed a novel semi-empirical-analytical model of the magnetic field configuration at Mars including the crustal sources and their reconnection to interplanetary magnetic fields.

5. Confirmed the results from the semi-empirical-analytical model by comparing them with the results obtained from a self-consistent four-ion single fluid Magnetohydrodynamic model, allowing for more accurate and reliable description of the exact nature of the solar wind interaction with Mars

1.3 Thesis Organization

This dissertation is organized as follows.

In Chapter 2, we report a new local event of particle enhancements in data from the Mars Global Surveyor orbiter's Electron Reflectometer (MGS/ER) instrument and characterize the nature of these events.

Chapter 3 describes our proposed mechanism for the source of the low energy electron flux enhancements. As this mechanism requires the reconnection of the crustal magnetic fields with the draping interplanetary magnetic field, a brief theoretical background for the magnetic reconnection process is provided. Correct alignment of the interplanetary magnetic field with respect to crustal sources at the times of the enhancements is searched and the results of this analysis are reported.

Chapter 4 introduces a novel semi-empirical-analytical model, developed for the description of the magnetic field configuration of the solar wind interaction with Mars. In this model, the overall magnetic field of the interaction is derived from the vector superposition of the crustal fields and the perturbed solar wind field around the obstacle. The description of these two components of the model is followed by the detailed derivation of the overall field. The results from the model account for the observed electron enhancements.

In Chapter 5, the primary results from our semi-empirical-analytical model are validated by the results obtained from a self-consistent Magnetohydrodynamic (MHD) model, allowing for more accurate and reliable description of the exact nature of the

solar wind interaction with Mars.

Overall conclusions are presented in the last chapter with a discussion of possible future extensions of this work.

Chapter 2

Extraordinary Electron Flux Enhancements

In this chapter, we report a novel transient phenomenon observed on MGS MAG/ER data, characterize the nature of the event, and provide a physical explanation for its occurrence. Before giving the details of our observations, we briefly introduce the Mars Global Surveyor mission and present details of the MGS MAG/ER data set.

2.1 Mars Global Surveyor Data Set

2.1.1 Mars Global Surveyor

Mars Global Surveyor (MGS) was the first mission of NASA's Mars Surveyor Program, a series of orbiters and landers to obtain global weather and surface topography of Mars (Figure 2.1a). MGS was launched on November 7, 1996, and after a 10-month cruise it entered an elliptical orbit around Mars on September 12, 1997. The spacecraft spent the next four months in aerobraking phase, during which it slowed down using the planet's atmosphere to enter its final circular mapping orbit (see Figure

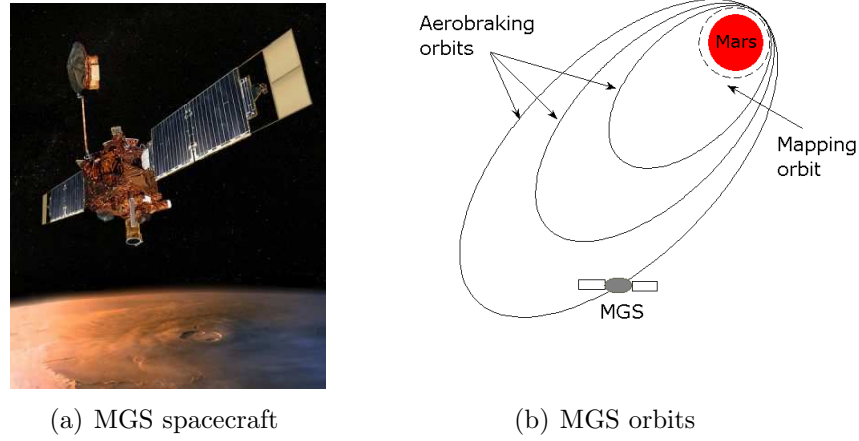


Figure 2.1: (a) Mars Global Surveyor (MGS) spacecraft. (b) The orbit geometry of MGS in different phases of the mission.

2.1b). A latch problem on the solar panels extended this phase about six months until September 1998. This extended period is called the Science Phasing Orbits (SPO) during which periodic observations were made with a 171 km periapsis. Finally, after six more months of careful and slower aerobraking, MGS reached its circular orbit in February 1999 and Science mapping phase began. During this phase, the polar orbit of MGS was nearly circular at an altitude of 400 km, fixed at 2 am–2 pm local time, with MGS completing an orbit every 2 hours and orbiting almost 12 times in one Martian day. The orbit had a seven-day near-repeat cycle, so that Mars could be mapped in 26-day cycles [Albee *et al.*, 2001].

Mars Global Surveyor operated in orbit around Mars for more than nine Earth years, longer than any other spacecraft to Mars and long enough to complete three extensions of its original two-year mission. Contact with Mars Global Surveyor was lost on 5 November, 2006. During this extended operation period, in addition to completing its science objectives, MGS observed changes with respect to Martian years and acted as a data relay station for the following Mars missions. There are

many important discoveries and contributions of this mission to current knowledge, but a particularly interesting one is that Mars has no detectable global magnetic field, but instead has local strong crustal sources mostly localized over the southern hemisphere.

2.1.2 The Magnetometer and the Electron Reflectometer

Mars Global Surveyor carried five science instruments onboard for investigation and mapping of the planet from the 400 km circular orbit. The observations that formed the foundation of this dissertation came from the MGS Magnetometer/Electron Reflectometer (MAG/ER) instrument. The MGS MAG/ER instrument consisted of two redundant triaxial fluxgate magnetometers (MAG) and an electron reflectometer (ER), and had a science objective of mapping near Mars magnetic environment and investigating the Martian solar wind interaction (for details see [Mitchell *et al.*, 2001]).

The MAG provided vector measurements of the in-situ magnetic field at rates up to 32 samples per second over a dynamic range from $(+/-)4$ nT to $(+/-)65,536$ nT with a digital precision of 12 bits. The dynamic range was automatically adjusted by the digital processor to deal with large changes in field amplitude. Typical instrumental noise levels were 0.01 nT. On MGS, all scientific instruments were mounted on the nadir instrument deck except the magnetometers, which were mounted near the ends of the solar panels for the minimization of spacecraft generated fields.

The ER measured the local electron flux (in $\text{cm}^{-2} \text{s}^{-1} \text{sr}^{-1} \text{eV}^{-1}$) averaged over a $360^\circ \times 4^\circ$ disk-shaped field of view in 19 different energy channels between 1 eV and 20 keV every 2 seconds, with an energy resolution of 25%. This energy range allowed for observation of ionospheric, sheath, and solar wind plasma. Detailed description of the MGS MAG/ER instrument and data processing can be found in [Acuña *et al.*, 1992] and [Acuña *et al.*, 2001].

2.1.3 Data Selection

As stated earlier, the mapping phase of MGS began in March 1999 and ended in November 2006. In this study, over six years worth of magnetometer and electron reflectometer (MAG/ER) data were used, acquired during the mapping phase between March 1999 and May 2005 and released by the Goddard Space Flight Center of NASA to the Planetary Data System (PDS) at the University of California, Los Angeles (UCLA). In other words, this study accessed 27,000 orbits of MAG/ER instrument data. During the mapping phase of the mission, the polar orbit of MGS was nearly circular at an altitude of 400 km, fixed at 2 am–2 pm local time, with MGS completing an orbit every 2 hours and orbiting almost 12 times in one Martian day. In order to remove redundancy and to reduce the size of six years worth of data, the vector measurements of magnetic field and omnidirectional electron flux data were first averaged to have a spatial resolution of a 1° by 1° grid on a spherical surface at 400 km altitude. This resolution was achieved by averaging the samples that fell into the same grid element along track using position information in MAG data files and time information in ER data files. This way the average sampling duration for both magnetic field and electron flux data was standardized to 10 seconds. Due to compression and expansion of the grid points in longitude going from the poles to the equator, the along-track samples are almost two seconds apart near the poles and twenty-one seconds apart near the equator. These averages were further labeled by factors that influence the plasma environment such as season and time of day.

2.2 Observation of the Electron Flux Enhancements

In examining the data sets produced by the above method, we found significant enhancements in the low-energy electron fluxes at the west edge of the crustal sources

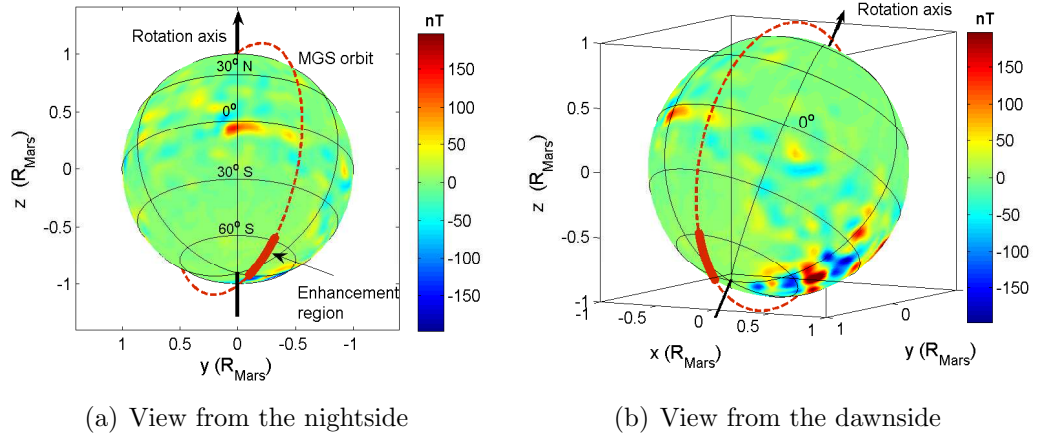


Figure 2.2: The geometry of MGS orbit and the orientation of Mars in the Sun-State coordinate system at the time of an enhancement event (MGS MAG/ER data recorded during this event is shown in Figure 2.3). The thick arrowed line shows the Mars rotation axis which is tilted towards the Sun for this case (northern hemisphere is in summer). The dashed red line indicates the orbit of MGS, and the marked region on the orbit shows the region where enhancement is observed. The color scale maps the radial component of the crustal magnetic fields observed at 400 km altitude and projected onto the Martian surface. (a) View from the nightside. (b) View from the dawnside in order to show the relative position of the strong crustal sources with respect to enhancement site.

during night time. In the ER data, low-energy omnidirectional electron fluxes (below \sim few hundred eV) exhibit sharp enhancements of approximately two orders of magnitude as MGS proceeds north to south at around 70° S on the nightside of the planet. Figure 2.2 shows the geometry of MGS orbit and the orientation of Mars for one of these events from two different view angles in the Sun-State coordinate system (SS) (which is the same as Mars Solar Orbital (MSO) coordinate system: the x -axis points at the Sun, the y -axis is anti-parallel to Mars' orbital velocity, and the z -axis completes the right-handed system). In Figure 2.2a, Mars is seen from the nightside. The thick arrowed line shows the Mars rotation axis which is tilted toward the Sun. In other words, for this case, the northern hemisphere is in summer. The dashed red

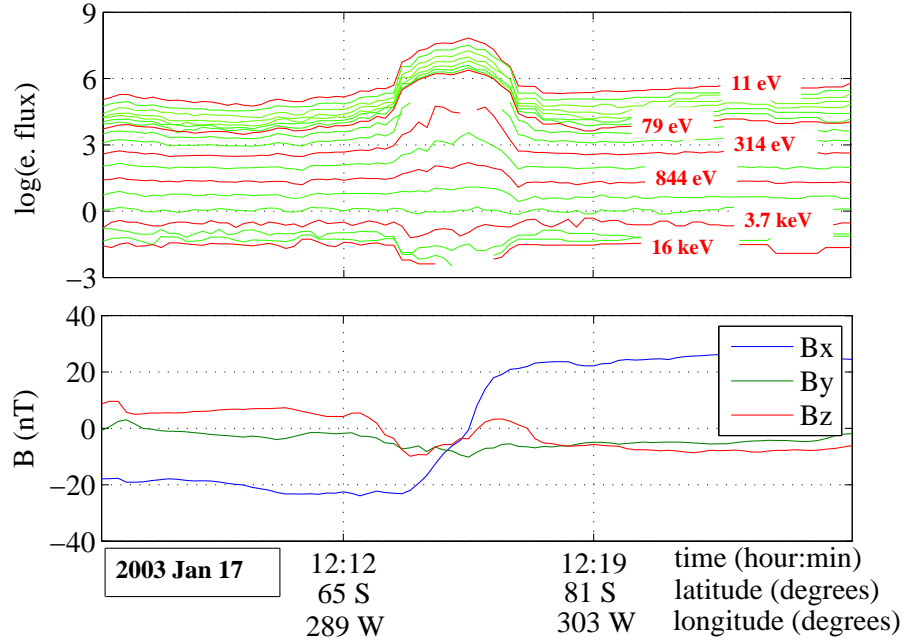


Figure 2.3: An example of a significant electron flux enhancement observed over the region between $30^\circ \pm$ and $120^\circ \pm$ E, at $\sim 70^\circ \pm$ S. The horizontal axis represents the time evolution as MGS moves from north to south on the nightside over the region of interest. The top panel is the logarithm of the omnidirectional electron fluxes at 19 energy levels, six of which are indicated on the curves, (the energy levels from top (10 eV) to bottom (20 keV) with energy resolution of 25%). The bottom plot shows the magnetic field components in the Sun-State coordinate system at the time MGS records the significant enhancement.

line indicates the orbit of MGS, and the region marked on the orbit shows the region where enhancement is observed. The color scale maps the radial component of the crustal magnetic fields observed at 400 km altitude and projected onto the Martian surface. Figure 2.2b shows the same figure viewed from the dawnside in order to show the relative position of the strong crustal sources with respect to enhancement site for this case. The top panel of Figure 2.3 shows the electron fluxes recorded by MGS as it passed over the marked region from north to south in Figure 2.3. The deviations in the magnetic field components during this event are shown at the bottom of Figure 2.3. The curves at the top of the figure present omnidirectional electron fluxes at

19 different energy levels between 11 eV and 16 keV on a logarithmic scale. (Only six energy levels are labeled in red on the plot for clarity.) Here the lowest energy electrons have the highest flux values. Electrons with energies below a few hundred eV exhibit the behavior we define as significant enhancements. The discontinuities seen in some of the energy levels are due to saturation of the ER instrument.

The curves at the bottom of Figure 2.3 show the three components of the magnetic field simultaneous to the ER flux records in the SS. As seen in this figure, the major change in the field strength is observed in the x component with a sign reversal from $-$ to $+$, which implies a significant azimuthal current flow in the negative direction. During the enhancement event, the z component of the magnetic field remains low while y component has a slight offset in the negative direction. These signatures in the magnetic field data are typical for any of the observed enhancements. Moreover, as can be inferred from the plot, the average time interval that MGS spends in the enhancement region is about 200 sec, during which it moves about 650 km along its orbit.

To reveal the extent and the likelihood of occurrences, the percentage of the enhancements occurring among all nightside southern hemisphere observations was mapped over six years for each of the 19 energy levels. This map was then superimposed on the contour plot of radial component of the crustal magnetic fields. One example of these maps is seen in Figure 2.4. On this plot, the blue shaded colorbar indicates the contours of the radial magnetic field strength. These curves are obtained from the spherical harmonic expansion representation of the crustal sources developed by *Cain et al.* [2003] using MGS MAG data (see appendix A). The green to red colorbar on the top indicates the percentage of occurrences of the enhancements on the corresponding location over the southern hemisphere. The energy band in which the significant enhancements are detected covers the range from 10 eV to a few hundred eV. In this band, at each energy level the corresponding percentage

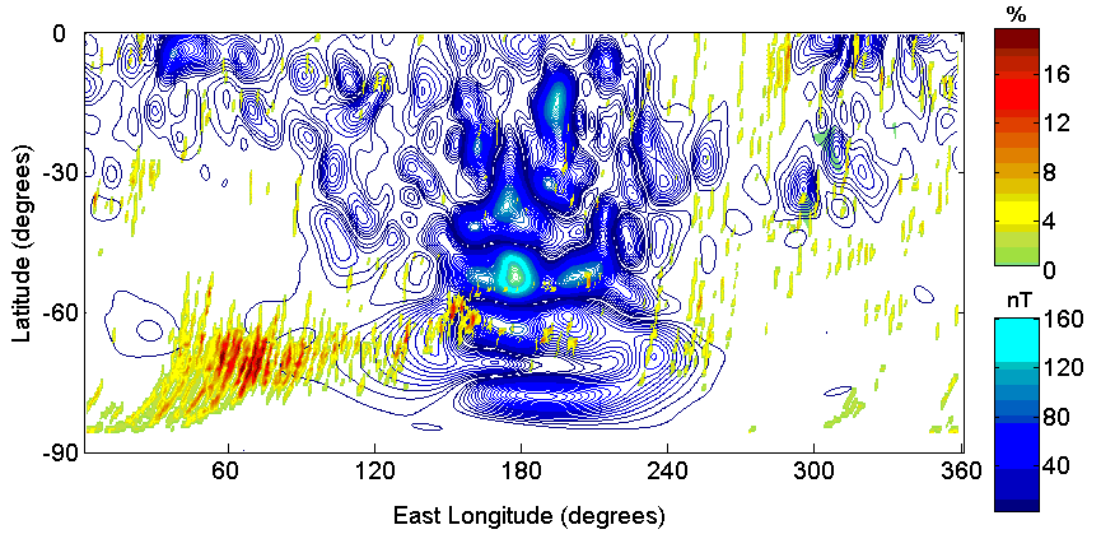


Figure 2.4: The map of the percentage of the significant enhancements in the 61 eV energy band among all nightside observations over the southern hemisphere superimposed on the contours of the radial component of the crustal magnetic fields. This map represents the general characteristics of all low energies below a few hundred eV.

occurrence map identifies an enhancement by selecting the observations having two orders of magnitude or more electron flux than the ambient flux. Figure 2.4 shows the map obtained for the 61 eV energy level. The features of this map are representative for the entire enhancement observation band. One evident feature in these maps, and displayed in Figure 2.4, is that at low-energy levels the significant enhancements appear to cluster in a local geographical area, between 30° and 120° E, and at around 70° S. Furthermore, this clustering region is absent of strong crustal sources. As can be inferred from the same figure, there are other locations scattered over the southern hemisphere where enhancements are observed at a lower rate. (This is also the case for the northern hemisphere.) However, typical properties of the enhanced energy distributions in the cluster (discussed in the following sections) are not statistically significant in the scattered regions due to the low observation rate. Thus, in this study, our focus is on the cluster seen on the bottom left corner of the map (between 30° and 120° E, and at around 70° S).

Statistical and spectral analyses of the electron flux enhancements in the cluster reveal common features of the enhancement events presented and characterized in the following section.

2.2.1 Characteristics of the Electron Flux Enhancements

The statistical analysis of the electron flux enhancements reveal that the enhancements have a periodic nature on both a Martian year scale and a ~ 25 day time scale. Moreover, the spectral analysis of the events demonstrate that their spectra are significantly different in nature from the spectra of other transient events observed on the nightside of Mars (such as auroras, strip-like plasma structure along the wake, plasma spikes, or plasma voids). Further the average magnetic fields in the enhancement region at times of the events have a common signature implying a significant current in the azimuthal direction. Each of these characteristics is discussed in detail in the following subsections.

2.2.2 Distinct Spectra

The enhanced low-energy distribution of the cluster suggests that the electrons in this region may have spectral characteristics that differ from those found in typical nightside spectra. In Figure 2.5a, the red shows that for a representative point in the cluster: the electrons in the cluster have a spectrum strongly enhanced at low energies [(1), red curve]. This representative spectrum is obtained by averaging over spectra from locations with significant enhancements. While passing through the enhancements, the ER instrument almost always saturates for energies above 79 eV and below few hundred eV (see Figure 2.3). The saturated measurements are not included in the averaging process; thus a kink near 100 eV is apparent in the spectrum (blue curve), implying higher electron fluxes in the vicinity of the kink. (Clustering

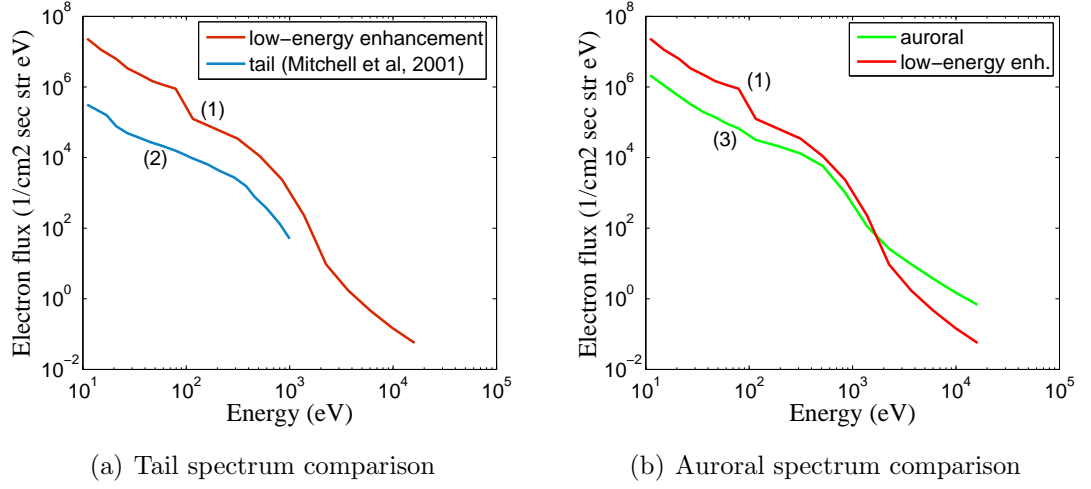


Figure 2.5: Comparison of electron energy spectra of two different regions in each figure obtained from the MGS ER data. (a) The red line shows the averaged spectrum of the significant enhancements observed between $30^\circ \pm$ and $120^\circ \pm$ E at $\sim 70^\circ \pm$ S, and the blue line shows the typical tail spectrum observed in the region of absent of crustal fields. (b) The red line shows the averaged spectrum of the significant enhancements observed between $30^\circ \pm$ and $120^\circ \pm$ E at $\sim 70^\circ \pm$ S and the green line shows the averaged spectrum of aurora observed at around $150^\circ \pm$ E, $70^\circ \pm$ S.

of low-energy electrons over the same region was noted by *Halekas et al.* [2006].) For comparison, on the averaged spectrum of the enhancements, the typical nightside spectrum is plotted [(2), blue curve]. This typical nightside spectrum was obtained by *Mitchell et al.* [2001] using MGS MAG/ER instrument data, which are recorded over the regions absent of crustal sources in the tail. As seen in the figure, the plots reveal that the spectrum of the enhancements is significantly intensified, more than two orders of magnitude, for the energy levels below few hundred eV.

The phenomenon we observe is different from the auroral events observed by *Bertaux et al.* [2005] and *Brain et al.* [2006a], which are mostly seen around the crustal fields and at higher energy levels. For comparison, a representative spectrum of auroral events is included with the representative spectrum of the significant enhancements in Figure 2.5b. The averaged spectrum of the auroral events ((3), green

curve) was obtained from the measurements having peaked electron spectra between 100 eV and 2.5 keV over the region centered near 150° E, 70° S, where most auroral events are accumulated [Brain *et al.*, 2006a]. As seen in Figure 2.5b, the spectra are significantly different from each other below a few hundred eV.

We also compare the electron energy distribution of the enhancements and of the plasma recorded in the permanent localized strip-like structures along the wake boundary reported by Dubinin *et al.* [2006a; 2006b]. The energy spectrum obtained using MEX electron flux measurements in these strip-like structures peak at ~ 80 eV, which is the typical energy of the magnetosheath electrons. This spectrum is not enhanced at low-energy levels, unlike the spectrum observed in the significant enhancements. Although the spectrum of these strip-like structures implies a magnetic connection of the IMF with the crustal field lines, Dubinin *et al.* [2006a; 2006b] found no evident correlation between the positions of the crustal sources and these localized strip-like structures.

2.2.3 Periodic Nature of the Electron Flux Enhancements

In the previous sections, it is mentioned that the enhancements are identified by an increase in the electron flux by two orders of magnitude from the ambient flux levels for the energies below 200 eV. Using this identification criterion, all the enhancement observations are selected between March 1999 and May 2005, and plotted as a function time. The first panel in Figure 2.6 illustrates this temporal distribution, and it clearly demonstrates the periodic nature of the events on a Martian year (which is almost two Earth years). Furthermore, the distribution of the enhancement occurrences with respect to Martian seasons is also obtained and plotted in the same figure. This seasonal variation is illustrated in the second panel of Figure 2.6 by presenting the variation of the occurrence of the events with respect to the areocentric longitude of the Sun, L_s . As inferred from the plot, enhancements are observed for the L_s

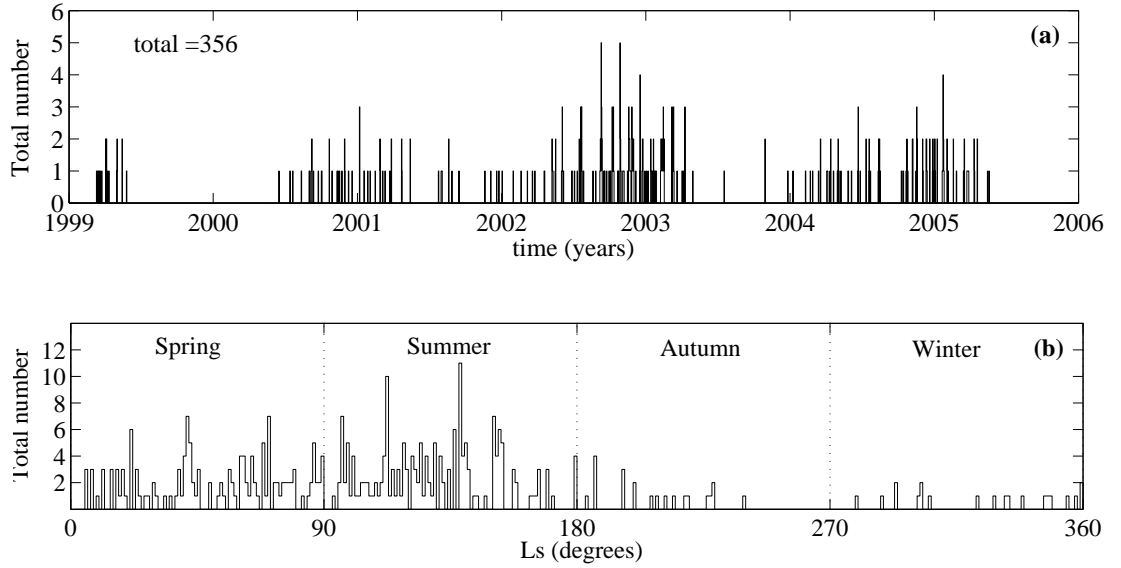


Figure 2.6: Periodic nature of the electron enhancements. (a) Temporal distribution of the occurrence of the electron enhancements with respect to time. (b) Seasonal variation of the occurrence of the electron enhancements with respect to the areocentric longitude of the Sun, L_s (Martian northern hemisphere seasons). (Note: Occurrence of the enhancements selected by criteria detailed in Section 2.2)

values ranging from 0° to 180° , which corresponds to the late Martian spring and early summer (i.e., Martian northern hemisphere seasons). This association implies that conditions for the significant enhancements are more favorable in the Martian northern hemisphere spring and summer.

Furthermore, for each electron flux level, the Fourier transform of the temporal variation of the enhancements is obtained, and the normalized spectral magnitude of the electron flux is plotted as a function of the fluctuation period. Through this spectral analysis, another periodicity on a ~ 25 day timescale becomes evident for the energies below few hundred eV. Figure 2.7 shows such a distribution for the ~ 116 eV electron flux level. The 116 eV energy level lies near the center of the energy band between 11 eV and a few hundred eV over which the enhancements are observed, representing roughly the general characteristics of the entire band. This secondary

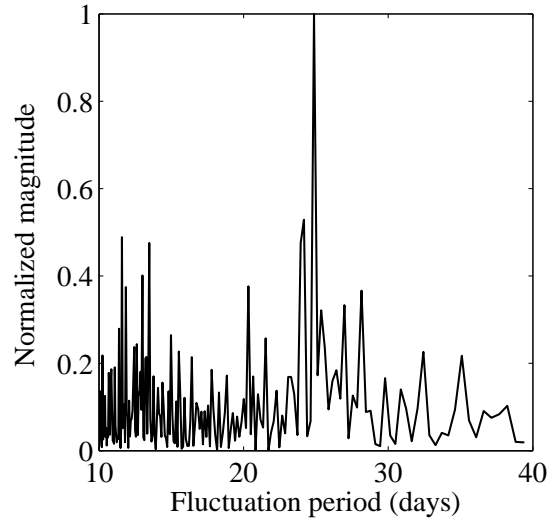


Figure 2.7: Fourier transform of the temporal distribution of the enhancements. The curve indicates the normalized spectral magnitude of the 116 eV omnidirectional electron flux, obtained from the Fourier transform and plotted as a function of fluctuation period. The 116 eV energy level lies almost near the geometric center of the energy band between 11 eV and a few hundred eV, over which the enhancements are observed. This energy band represents the general characteristics of the entire band.

periodicity is likely associated with the rotation period of the Sun.

2.2.4 Magnetic Field Perturbations

In Section 2.2 the existence of magnetic field perturbations in the vicinity of the enhancements simultaneous to the enhancements themselves is noted, and one typical example of these perturbations is illustrated in Figure 2.3. It is also stated that the implication of such a magnetic field configuration is a current flowing mainly in the negative azimuthal direction.

We searched for these magnetic perturbations over the clustering region by comparing the MAG measurements when the enhancements are present to the MAG measurements when the enhancements are absent. A map obtained by averaging the magnetic field components in the absence of the enhancements shows that B_x , B_y and

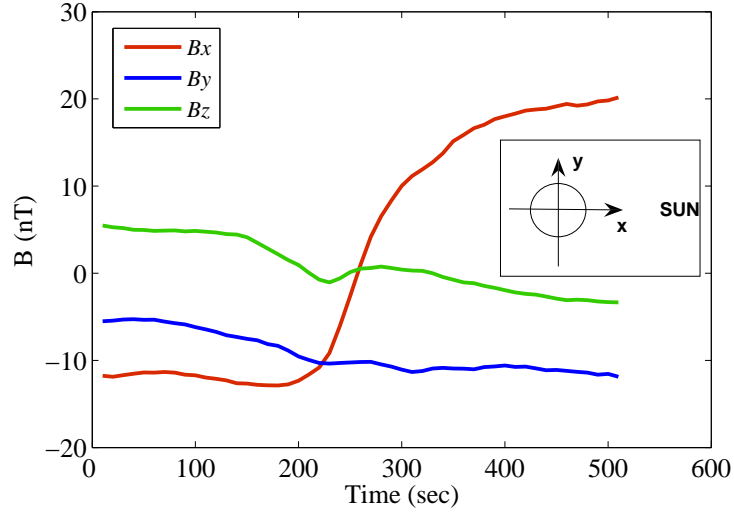


Figure 2.8: Averaged magnetic field components in the Sun-State coordinate system, obtained using the MAG data recorded at the times of enhancements.

B_z remain below 8 nT, 4 nT and 3 nT, respectively, over the enhancement region as expected because this region has no crustal sources [Cain *et al.*, 2003]. But, during an enhancement, the B_x and B_y components (in the SS coordinate system) can reach values of 15–25 nT and 5–10 nT, respectively. (The B_z component is still below 5 nT.) The nature of this behavior is shown in Figure 2.8. Note that the B_x and B_z components change sign from, $-B_x$ to $+B_x$, and $+B_z$ to $-B_z$, as MGS proceeds over the region where the enhancements occur. The overall magnetic field becomes almost zero at the time of the sign reversal, which coincides with the center of the enhancement region (Figure 2.3). Similar behavior in B_x was noted by Ferguson *et al.* [2005] and Halekas *et al.* [2006] during the MGS crossings across a two-lobe region induced by the current sheets in the tail. Reversals observed during the enhancements (shown in Figure 2.8) in B_x and B_z imply a current flowing mainly in the azimuthal direction while the offset in the averaged B_y component implies a current flowing in the z direction. The estimated width of such a current is a few hundred kms along the

latitudinal direction, while its azimuthal extent can reach 2000 km. The perturbations in B_x can be explained by a current aligned in the azimuthal direction, with a surface current density of $0.1 \mu\text{Am}^{-2}$.

Current Source Modeling of the Magnetic Field Perturbations

In this section, our objective is to model the current sources that may be responsible for the generation of the observed magnetic field disturbances. This model begins with the approximation that the current sources are current dipoles placed in the vicinity of the enhancements. In this model, dipole directions and their magnitudes are determined by a least squares estimation process. To obtain the model parameters, a linear system of equations is devised using the Biot-Savart law and the magnetic field measurements as follows.

Magnetic field produced at \mathbf{r} , by a current dipole at \mathbf{r}' , with a dipole moment \mathbf{Q} is given by the Biot-Savart law:

$$\mathbf{B} = \left(\frac{\mu_0}{4\pi} \right) \frac{\mathbf{Q} \times (\mathbf{r} - \mathbf{r}')}{|\mathbf{r} - \mathbf{r}'|^3} \quad (2.1)$$

The total magnetic field measured at \mathbf{r} is the vector sum of all the contributions from all N current dipoles:

$$\mathbf{B}_{i,\text{total}} = \sum_{n=1}^N \left(\frac{\mu_0}{4\pi} \right) \left(\frac{\mathbf{Q}_n \times (\mathbf{r}_i - \mathbf{r}'_n)}{|\mathbf{r}_i - \mathbf{r}'_n|^3} \right) \quad (2.2)$$

At each MGS pass in which an enhancement is observed, 50 magnetic field measurements are selected in the vicinity of the enhancement along the MGS path such that the midpoint of the measurements coincides with the center of the enhancement. Then, the expression above is applied for each magnetic field measurement, \mathbf{B}_i , yielding an over-determined linear system, $\mathbf{B}=\mathbf{A}\mathbf{x}$. In this system, \mathbf{B} is a vector of $M=50$ magnetic field measurements, $i=1 \dots 50$, ($3M$ samples since \mathbf{B} is a vector),

\mathbf{A} represents the $3M \times 3N$ matrix relating the current dipole moments to the field measurements, and \mathbf{x} represents the $3N$ unknowns, \mathbf{Q}_n , (the intensity and direction of N current dipole vectors) where $M > N$. The direct least squares solution of this system is non-unique and requires further constraint which is obtained by imposing the divergence free condition on the current (under static fields, $\nabla \cdot \mathbf{J} = 0$). Therefore, the model was constrained by assuming that the dipoles located near the enhancement are aligned on a conduit-like shape. This approach led us to place a number of current dipoles at equal distances in a volume grid centered where B_x , the magnetic field component along the x -axis in the SS coordinate system, is zero, i.e. the approximate center of the enhancement region. Both the distances between the dipoles and the number of dipoles are test parameters. Our primary focus was finding the direction of these sources rather than their magnitudes. Furthermore, to satisfy the divergence-free current requirement and to obtain meaningful flow direction for the sources, the current dipoles are forced to be continuous by applying a regularization method:

$$\mathbf{F} = \|\mathbf{A}\mathbf{x} - \mathbf{B}\|^2 + \mu\|\mathbf{C}\mathbf{x}\|^2 \quad (2.3)$$

In this expression, \mathbf{C} represents the matrix used in order to force the current continuity. The solution for \mathbf{x} that minimizes \mathbf{F} requires the matrix \mathbf{A} to be full rank. This constraint limits the number of the current sources, which for our case is 30. The solution to our problem becomes,

$$\mathbf{x} = (\mathbf{A}^T \mathbf{A} + \mu \mathbf{C}^T \mathbf{C})^{-1} \mathbf{A}^T \mathbf{B} \quad (2.4)$$

The directions of all dipoles, i.e., the flow direction of the possible current that can generate the magnetic field perturbations associated with each enhancement, are determined using Equation 2.4. It is found that almost every time an enhancement occurs, the current dipoles are aligned in the direction of the crustal magnetic source

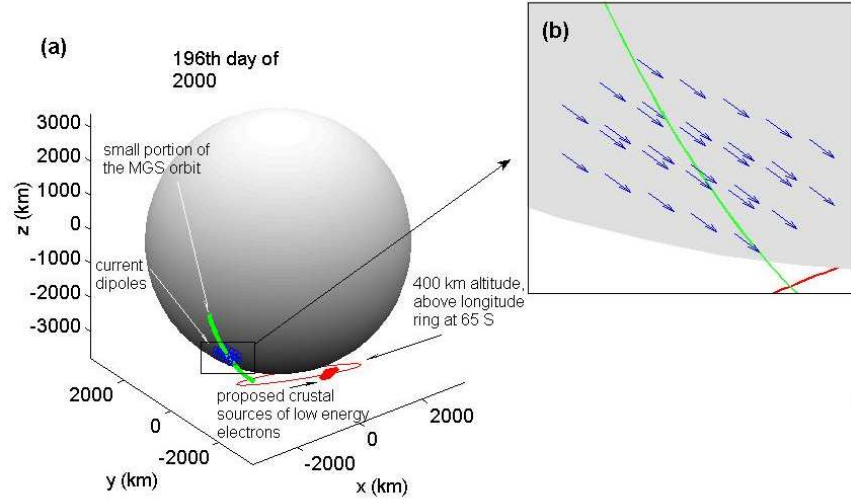


Figure 2.9: An example model of current sources at the time of an enhancement observed on the 196th day of 2000. a) The view is in the SS coordinate system. Current dipoles are displayed in blue and parameters were estimated using the MGS MAG data recorded along the portion of the orbit, marked in green. The red ring at the bottom is the $65^\circ \pm$ S parallel at an altitude of 400 km. The red rectangle on the ring represents the crustal magnetic fields at $\sim 150^\circ \pm$ E, $65^\circ \pm$ S. b) Zoomed-in view of the current dipoles of the model example on the 196th day of 2000.

region (the electron flow should be opposite to current direction, i.e., away from the crustal sources). Figure 2.9 illustrates the geometry, orbit, and current dipoles associated with a sample enhancement observed in the spring of 2000. In Figure 2.9, results are shown in the SS coordinate system. The green line shows the part of the orbit of MGS as it proceeds from north to south on the nightside. The same line also represents the magnetic field measurement positions used in the model. The red ring at the bottom is at the latitude of 65° S and an altitude of 400 km in the body-fixed coordinate system. The marked region (red rectangle) on the ring indicates the relative location of the strong crustal sources. As illustrated, the marked crustal fields see the Sun at the time an electron density enhancement is observed along the path of MGS marked in green. The estimated current source vectors (30 dipoles in

this model) are shown in blue in the middle of the portion of the MGS path, and their zoomed view can be seen in the box next to Figure 2.9. The distance between neighboring current dipole sources was chosen to be 150 km. Note that the dipole sources point toward the crustal sources and have a major component in the $-y$, a small component in $+x$, and a relatively small component in the $(+/-)z$ direction. Similar method is applied to each enhancement, and in each case the ensemble of current dipoles, as determined from the optimization discussed above, was remarkably similar in orientation and magnitude.

2.3 Summary

In this chapter, we report a new transient phenomenon which is observed in the Mars Global Surveyor electron omni-directional flux data over a specific geographical region at the west edge of the crustal fields on the nightside of Mars (at around 70° S and between 30° E and 150° E). As MGS passes over this geographical region from north to south on the nightside, the low-energy omnidirectional electron fluxes below a few hundred eV exhibit sharp enhancements, an increase of approximately two orders of magnitude over the ambient flux levels.

The statistical and spectral analyses of the electron flux enhancements reveal three critical features of the phenomena. (i) The enhancement events exhibit two periodicity on a Martian year scale and a ~ 25 day time scale, (ii) The spectra of the events are different in nature from the spectra of any transient event observed at the nightside of Mars such as auroras or strip like plasma structure along the wake boundary or plasma spikes, or plasma voids. (iii) The magnetic fields recorded in the enhancement region at time of the events have common a signature which imply a significant current in the azimuthal direction.

The current sources, as candidates for the generation of the magnetic disturbances accompanied by the electron enhancements, are modeled by current dipoles. The orientations of the dipoles are estimated using a least squares method under the divergence free current condition. Determining the model parameters for each enhancement event, the flow direction of current that can generate the magnetic field perturbations is estimated and found that almost every time an enhancement occurs, the current dipoles are pointing toward the crustal magnetic source region.

Chapter 3

Physical Explanation of the Electron Flux Enhancements

3.1 Introduction

In the previous chapter, we described a new transient phenomenon which is observed in the Mars Global Surveyor electron omni-directional flux data over a specific geographical region at the west edge of the crustal magnetic fields (at around $70^\circ \pm S$ and between $30^\circ \pm E$ and $150^\circ \pm E$). As MGS passes over this local region from north to south on the nightside, the low-energy omnidirectional electron fluxes below a few hundred eV exhibit sharp enhancements, approximately two orders of magnitude above the ambient flux levels. In this chapter, possible physical explanations for the observed electron flux enhancements are discussed and a mechanism is proposed for the source of the particles.

3.1.1 Discussion of the Possible Source Mechanisms

In this section, we discuss the possible source region and physical explanations for the electron flux enhancements.

As discussed in Chapter 2, auroral activity has been discovered in Mars Express ultraviolet spectrometer data by *Bertaux et al.* [2005], and auroral-like events have been found on MGS MAG/ER instrument data near the crustal sources by *Brain et al.* [2006]. Since the typical feature of an auroral event has a local peak in the energy spectrum, the intensifications at certain energy levels seen in the spectra of the enhancements (Figure 2.5b) suggest that these events might be aurora occurring on the nightside of Mars. Furthermore, as in the case of the auroral events, the acceleration of the electrons during these enhancements can be explained by the field aligned electric fields that are generated during the reconnection of the draped IMF with the crustal sources. However, as we concluded in Chapter 2, the enhancement phenomenon we observe is different from previously reported auroral events at Mars, since typically the spectrum of an auroral event has a peak between 100 eV and 2.5 keV, while our observations have intensifications above few hundred eV in their spectra (see Figure 2.5b). Moreover, the typical observation region of the enhancements is localized away from the crustal sources, while the auroral events are seen close to these sources and are more likely where the radial component of the magnetic field is the highest.

The fact that the enhancements are observed on the nightside and the magnetic field reversals occur in the vicinity of the enhancement site suggests that the phenomenon may be due to ionospheric electron carriage by the IMF. The draping IMF lines may carry the ionospheric electrons, dragging them through the ionosphere, and slipping them around the poles and/or the sides of Mars. Then, electrons might be accelerated by the field aligned electric fields and pushed toward the central tail under the influence of the magnetic field tension forces $\mathbf{J} \times \mathbf{B}$. This process is also one of

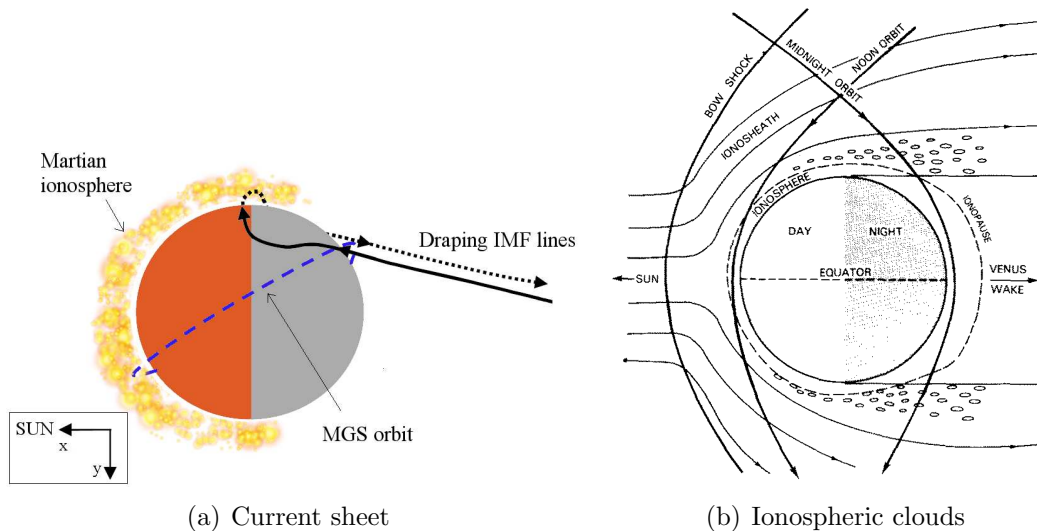


Figure 3.1: (a) MGS crossing of a current sheet at Mars. Draping IMF carries photoelectrons from the ionosphere to the tail and causes magnetic reversals on the tail. (Adapted from [Halekas *et al.*, 2006]) (b) The interaction of solar wind plasma with the dayside ionosphere produces clouds of plasma which may become detached and swept downstream in the ionosheath or may remain attached to the ionopause. (Adapted from [Brace *et al.*, 1982]).

the probable mechanisms responsible for the formation of the current sheets (Figure 3.1a) observed in the tail [Halekas *et al.*, 2006]. However, this by itself cannot be adequate because, if it were, the enhancements would be observed over the entire nightside hemisphere of Mars rather than just clustering in a localized region in the southern hemisphere. Moreover, they would occur anytime during the entire Martian year rather than only in the northern hemisphere's late spring and early summer.

An alternative scenario that takes into account the local clustering of the enhancements would be to stretch the closed field lines from the location of the crustal sources on the dayside toward magnetotail around the dawnside of Mars. In this case, electrons already trapped in the closed fields would follow the same lines, while remaining trapped moving in both directions along these lines. However, this bi-directional

motion is inconsistent with the magnetic field data recorded in the vicinity of the enhancements, which imply a current dominant in one direction (in the (+) azimuthal direction) (Figure 2.8). Furthermore, this current is also confirmed by current source modeling of the magnetic field perturbations in Section 2.2 of Chapter 2.

The existence of a regular temporal variation in the occurrences of the enhancements and simultaneous magnetic field perturbations also make it unlikely that ionospheric irregularities or plasma clouds are the source for this phenomenon. The interaction of the solar wind with the dayside ionosphere produces clouds of plasma (see Figure 3.1b) which may become detached and swept downstream from the flanks of the planet or remain attached to the ionosphere [Brace *et al.*, 1982]. These ionospheric plasma irregularities exhibit enhanced photoelectron spectra having local peaks and primarily observed near the terminator and further downstream, where electrons are accelerated by magnetic forces [Perez, 2000]. These features suggest that the electron enhancements we observe may be ionospheric clouds. However, observations of ionospheric clouds at Venus reveal that clouds are scattered around the periphery of the planet in the terminator plane, and there is no evidence of a concentration of clouds only over one hemisphere of the planet [Ong *et al.*, 1991]. Since electron flux enhancements are clustered over a specific region over the southern hemisphere and have a periodic nature, it is unlikely that these events are correlated with the ionospheric clouds. Moreover, the regularity in the temporal and spatial variation of the enhancements makes it less probable that these events originate from sudden energy releases or disturbances, associated with solar flares or coronal mass ejections (CMEs).

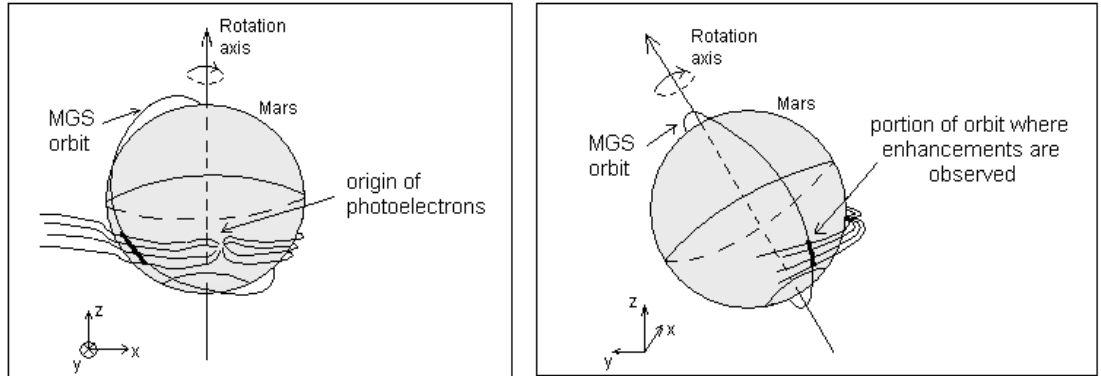


Figure 3.2: Relative positions of Mars, the MGS orbit, the crustal sources, and the draped field lines in the SS coordinate system at the time an enhancement is observed. The first panel shows the side view while the second panel shows the view from an angle on the nightside. Reconnected and draped IMF lines carry the photoelectrons from the dayside to the nightside, and a current form in the tail. The MGS orbit traverses the current obliquely on the nightside. The marked region shows the portion of the MGS orbit over which the enhancement is observed and the magnetic reversals are recorded in the middle of this marked region.

3.2 Proposed Source and Transport Mechanism

The following mechanism is proposed as the source of the observed electron flux enhancements: The photoelectrons generated over the crustal sources on the Martian dayside are transported along reconnected IMF lines to the nightside and populate the currents formed in the tail. During this process, solar wind electrons have access to the lower magnetospheric or upper ionospheric regions, and they may also be carried by the reconnected field lines, forming a mixture of sheath and planetary plasma. The interpretation of this mechanism is shown in Figure 3.2, where the relative positions of Mars, reconnected field lines, MGS orbit, and the enhancements are illustrated from two view angles in the SS coordinate system. As can be inferred from this figure, at the time of the enhancements, the MGS orbit crosses the reconnected and draped field lines, in which the low-energy photoelectrons flow from the dayside to the nightside. The field reversals, seen in Figure 2.3, occur in the middle of

the marked region on the MGS orbit over which enhancements are observed. Given this interpretation, three essential criteria are needed all of which can be validated by direct measurements: (i) The enhancements are most likely to occur when the draped IMF direction and the field line orientation of the crustal sources are aligned for reconnection. (ii) The magnitudes of the fields are comparable at the reconnection site. (iii) The source region of the low-energy electrons should be exposed to the Sun at the time the enhancements are recorded. During this process, field aligned electric fields and magnetic tension forces may accelerate the electrons to higher energy levels, and movement of the electrons toward central tail may be due to draping of the field lines.

3.2.1 Event Spectra

The proposed scenario requires the transfer of photoelectrons from the dayside to the nightside of the planet and thus implies that the signatures of ionospheric photoelectrons should be present in the spectra recorded during the enhancements. Two major photoelectron peaks at ~ 20 eV and ~ 30 eV are produced in the CO₂ dominated atmosphere of Mars, which are due to ionization of O and CO₂ [Frahm *et al.*, 2006a]. However, the energy resolution of the ER instrument (25%) is too coarse to resolve the photoelectron peaks, and they unfortunately cannot be distinguished in the data (e.g., Figure 2.5a). Dispersion at low energies due to further particle interactions during the photoelectrons' travel from the dayside to the nightside may also contribute to loss of the peaks in the observed spectra. Furthermore, assuming the acceleration mechanism for aurora is operating most of the time during the enhancements, the smoothed peak between 100 eV and 2.5 keV implies the presence of sheath plasma along with the planetary plasma during these events.

3.2.2 Magnetic Reconnection

The proposed scenario requires reconnection of the draping IMF lines with the local crustal magnetic fields. This section gives an overview of magnetic reconnection and describes a simplified two-dimensional (2-D) steady-state model of the process (for more detailed description see [*Priest and Forbes*, 2000; *Biskamp*, 2000; *Sonnerup*, 1979] and references therein).

Magnetic reconnection is a process of breaking and rejoining magnetic field lines at the boundary between two magnetized plasmas, through which magnetic energy is converted into thermal and kinetic plasma energy. This process is found in many dynamic processes in space, such as the interaction of the solar system bodies with the solar wind, the generation of the Sun's magnetic field, coronal heating on the Sun, solar flares, and coronal mass ejections.

The first use of magnetic reconnection as a source of particle acceleration in magnetized plasmas was proposed by *Giovanelli* in 1946. In the 60 years since, many theoretical models have been developed to describe the magnetic reconnection based on magnetohydrodynamics (MHD) or on collisionless plasma theory [*Priest and Forbes*, 2000]. These models are grouped into 2-D or 3-D and steady-state or transient models. In this thesis, a model based on MHD approximation is introduced for the description of the magnetic reconnection, and a two-dimensional 2-D steady-state model is illustrated for the interpretation of the process. Although this description and interpretation is over-simplified, it provides good physical insight and is essentially consistent with the observations at Mars.

In the MHD approximation, the plasma is treated as a conducting fluid, and the electric field in this fluid is expressed by the Ohm's law as

$$\mathbf{J} = \sigma(\mathbf{E} + \mathbf{u}_m \times \mathbf{B}) \quad (3.1)$$

where σ represents the finite conductivity, and \mathbf{u}_m is the bulk velocity of the plasma. An equation governing the magnetic field in this conducting fluid can be derived from the curl of the electric field and Maxwell's equations.

$$\frac{\partial \mathbf{B}}{\partial t} = \nabla \times (\mathbf{u}_m \times \mathbf{B}) + \frac{\nabla^2 \mathbf{B}}{\mu_0 \sigma} \quad (3.2)$$

This equation is called the induction equation where μ_0 is the permeability of vacuum. The two terms on the right hand side are called the flow and the diffusion term, respectively, and ratio of the flow to the diffusion term gives the magnetic Reynolds number:

$$R_M = \sigma \|\mathbf{u}_m\| \mu_0 L \quad (3.3)$$

where L denotes the characteristic dimension of the system. The value of the magnetic Reynolds number of the system indicates whether the system is diffusion or flow dominated. For highly conducting plasma or in the absence of collisions, this number is high ($R_M \gg 1$), and the system is flow dominated. In mathematical terms in a highly conducting plasma magnetic field can be describe as

$$\frac{\partial \mathbf{B}}{\partial t} = \nabla \times (\mathbf{u}_m \times \mathbf{B}) \quad (3.4)$$

$$\frac{d}{dt} \left(\int_A \mathbf{B}(\mathbf{r}, t) \cdot d\mathbf{A} \right) = 0 \quad (3.5)$$

Another interpretation of Equation 3.5 is that, in highly conducting plasma, flow dominates the evolution of the magnetic field and forces it to move with the plasma. In other words, magnetic flux and plasma particle density contained in a flux tube remains constant and independent of the motion of the flux tube. This formulation is known as a frozen-in magnetic field condition. As stated previously, magnetic reconnection is a process of changing magnetic topology at the boundary between two magnetized plasmas. Considering the MHD formulation above, it is assumed that

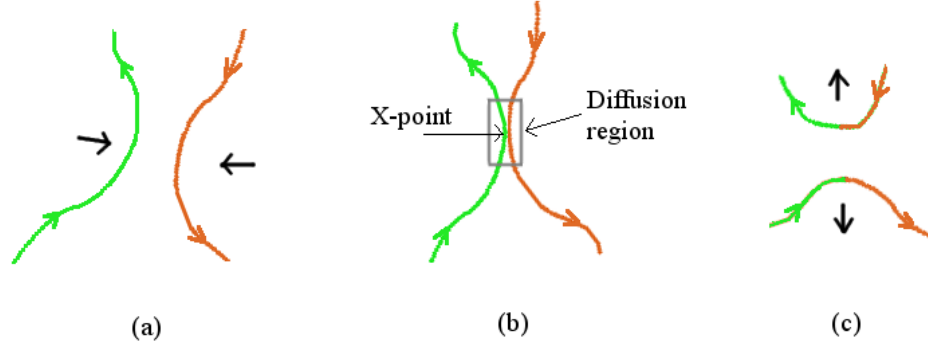


Figure 3.3: 2-D steady-state interpretation of the reconnection process. (a) Convection of oppositely directed field lines. (b) Reconnection of the field lines in the diffusion region. (c) Changed magnetic topology after reconnection.

the two neighboring plasmas are flow dominated. Under these conditions, Figure 3.3 illustrates a 2-D steady-state interpretation of this process. When oppositely directed magnetic field lines from these two magnetized plasmas come closer (Figure 3.3a), they are convected toward each other and are interconnected in the X-point located in the center of an area called the diffusion region (Figure 3.3b). This area is defined by the boundary where the frozen-in condition of ideal MHD approximation is broken, and the magnetic fields can diffuse through the plasma. Outside this boundary, the magnetic fields are still frozen-in, resulting in a new class of reconnected field lines and changing the initial magnetic field topology, as seen in Figure 3.3c. Realization of this process is possible only by a force which is the parallel electric field, E_{\parallel} , generated within the diffusion region. Furthermore, the Lorentz force:

$$\mathbf{J} \times \mathbf{B} = \frac{1}{\mu_0} \nabla \cdot (\mathbf{B}\mathbf{B}) - \nabla \left(\frac{B^2}{2\mu_0} \right) \quad (3.6)$$

accelerates the plasma away from the X-point, converting magnetic energy into plasma

kinetic energy and partially into plasma thermal energy. Moreover, the magnetic tension forces push the particles to reduce the curvature of the newly created reconnected field lines contributing to the energy conversion.

Although a 2-D steady-state model of magnetic reconnection is introduced above, reconnection is in fact a 3-D and time dependent process having a more complicated physical structure than the simplified interpretation above. General magnetic reconnection is a tear of connected field lines due to a localized non-idealness and their rejoining in a localized diffusion region in the presence of a parallel electric field [Schindler and Hesse, 1988]. Schindler [1988] showed that the presence of a non-zero parallel electric field in the diffusion region is necessary and sufficient for general magnetic reconnection. In recent years, more complicated and accurate descriptions of magnetic reconnection have been developed to account for the dynamics of electrons and ions by the application of different modeling approaches, such as hybrid and kinetic models as well as resistive MHD models. [Birn *et al.*, 2001; Hesse *et al.*, 2004; Drake *et al.*, 2005;2006; Gosling *et al.*, 2005; Mozer *et al.*, 2005]. All these models and general descriptions of the magnetic reconnection imply that the realization of this process is more likely when the field lines from the two neighboring plasma domains are aligned anti-parallel and similar in magnitude. In addition, the primary reason for the acceleration of the particles is the parallel electric field generated in the reconnection site during the process.

In 1961, Dungey applied the magnetic reconnection mechanism described here to the Earth's magnetosphere, and obtained the first direct evidence of this process at the Earth's magnetopause in 1979 [Paschmann *et al.*, 1979]. Today, reconnection is known to be the source of auroral events, and the particle accelerations observed during these events both on the dayside and in the magnetotail at Earth. Although Mars has no global magnetic dipole field, topological similarities between the Earth's dipole field and local crustal fields imply that similar physical processes would be

present over the strong crustal sources on Mars. In other words, reconnection of the draping IMF lines with the crustal magnetic sources is expected to occur on both the dayside and the nightside of Mars. As mentioned in the introduction, based on the MGS electron observations at Mars, *Mitchell et al.* [2001] proposed that magnetic reconnection occurs above the strong crustal sources on the nightside. This was followed by the proposal of cusp-like formations near the crustal sources by *Krymskii et al.* [2002], implying magnetic reconnection over them. The first observation of auroral emission at Mars was detected on Mars Express data above a strong crustal source at 177° E and 52° S by *Bertaux et al.* [2005]. Furthermore, *Brain et al.* [2006] correlated auroral-like events with the electron flux enhancements in the vicinity of the crustal sources suggesting the reconnection of crustal magnetic fields with the draped IMF.

As stated previously our physical explanation for the electron flux enhancements calls for reconnection of the crustal field lines with the IMF lines as IMF drapes over the local sources on Mars. Therefore, when the draping IMF lines properly align with respect to the local crustal fields, magnetic reconnection may take place. In the following section, we investigate the existence of the condition of reconnection by estimating the draping direction of the IMF at the time of the enhancements and comparing it to the alignment with the proposed crustal sources.

3.2.3 Estimation of the Draping Direction of the Interplanetary Magnetic Field

The description of the magnetic reconnection process in the previous section suggests that reconnection of the crustal field lines with the draped IMF would be best facilitated if the IMF were aligned anti-parallel with respect to the field above the crustal sources at the time of the enhancements. In order to see whether this condition holds

during the enhancements, direction of the draped IMF is estimated at MGS orbit altitude, 400 km, over the surface of Mars. *Brain et al.* [2006b] first proposed a method of estimating the draped IMF direction using magnetic field data recorded on the dayside over the northern hemisphere (where crustal fields are absent in the latitude band between 50° and 60° N). Applying the same method, the angle between local magnetic field component parallel to the MGS orbit and the component perpendicular to the orbit plane is obtained (i.e., local phi and theta components in a body-centered spherical coordinate system) and this angle is used as the approximate direction of the draped IMF. These angles are illustrated in Figure 3.4. In the calculation of the IMF direction, only the horizontal component of the magnetic field with respect to the Martian surface is used since we show that on the MGS MAG data between 50° and 60° N, the horizontal component of the draped field reaches 100 nT while the magnitude of the radial components is below 4(+/- 2) nT 75% of the time. In other words, the inclination angle (the angle that the magnetic field makes with the local horizontal) is very small most of the time, and the draping direction of the IMF at this altitude is mostly determined by the azimuthal and longitudinal components. Moreover, using MGS MAG elliptical orbit mission phase data, *Crider et al.* [2001] estimated the general draping structure of IMF around Mars away from the crustal sources and concluded that the local magnetic field is mostly horizontal close to the planet on the dayside. They showed that average inclination angle increases from 0° at local noon to 10° at the terminator [*Crider et al.*, 2001]. Thus, in order to estimate the direction of the draped IMF, the angle is defined as in the following expression (see Figure 3.4).

$$\alpha_{\text{IMF}} = \arctan \left(\frac{B_{\phi}}{B_{\theta}} \right) \quad (3.7)$$

Note that when the draped IMF is fully southward, this angle is 0°, and when the draped IMF is fully eastward, this angle is 90°.

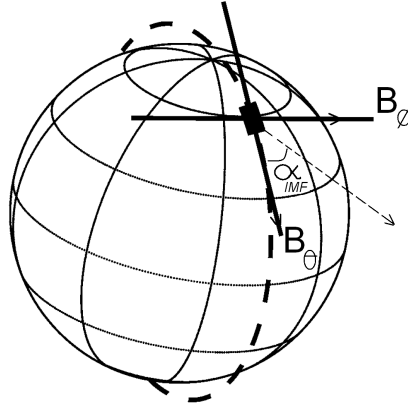


Figure 3.4: Definition of the IMF angle. The θ and ϕ components of the local magnetic field are shown. The dashed line indicates the MGS orbit, and the black rectangular box covers the portion of the orbit from 50° to 60° N. (Adapted from [Brain *et al.*, 2006])

Figure 3.5a shows the mean of the direction of the draped IMF estimated using Equation 3.7 at each pass, over six years, determined over the latitude band (50° – 60° N) in the northern hemisphere. The time period between each pass of MGS is about 2 hours, which adds up to $\sim 27,000$ passes in the time period of interest. Furthermore, at each pass there are many measurements (10 samples on average) in this latitude band. The mean of the angle, α_{IMF} , for each pass is obtained by summing the unit direction vectors of these magnetic field measurements. In this averaging process, erroneous outliers are eliminated, which are defined to be the ones that lie outside of the $\pm 90^\circ$ band centered at the mean. Following this approach, the standard deviation of the mean angle is less than 60° , 80% of the time. It should be noted that the IMF direction changes on many timescales, and thus an estimate obtained from a small portion of the orbit does not necessarily represent the orientation throughout the entire orbit. However, for our purpose, the IMF was assumed to be constant over an orbit and represented by the estimate obtained from the 50° – 60° N latitude band. Figure 3.5a displays the periodicity in the mean angle on almost two Earth year

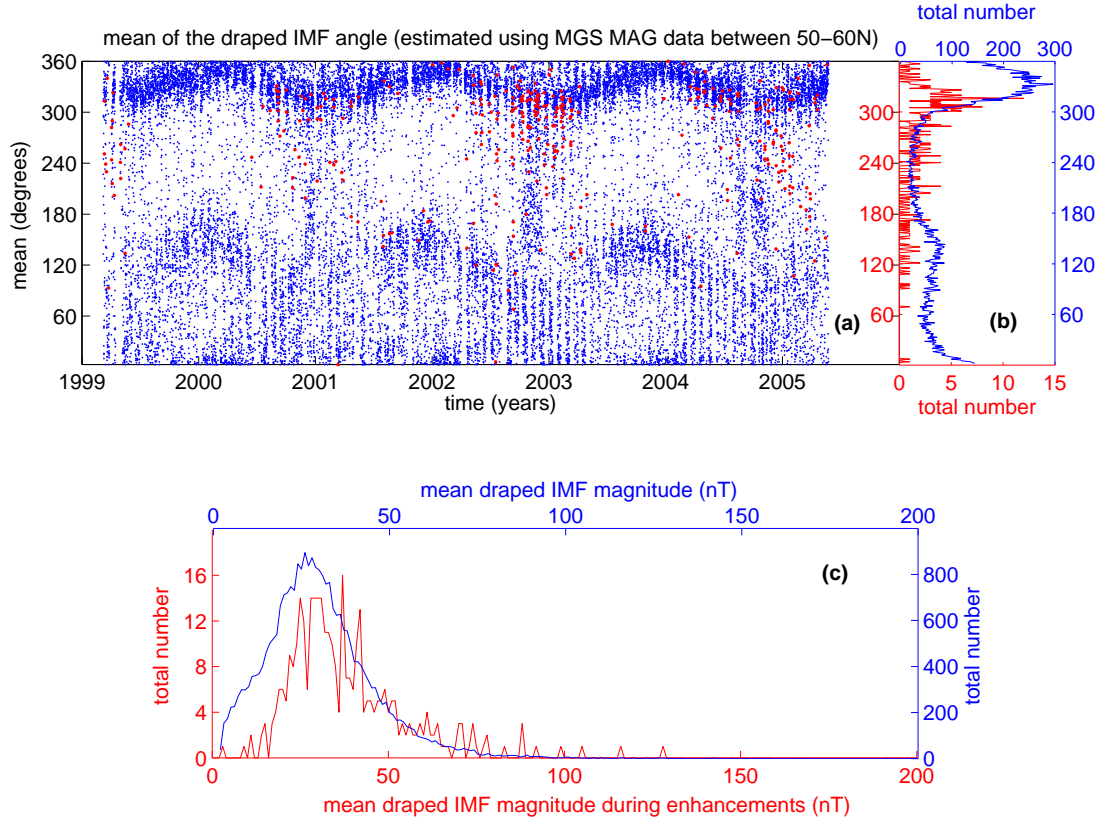


Figure 3.5: The direction and magnitude of the draped IMF obtained from the MGS MAG data between $50^\circ \pm$ and $60^\circ \pm$ N. a) Mean of the draped IMF angle at each pass during six year time period. The red dots mark the passes on which the significant enhancements are observed over the region of interest. b) The histogram of the mean angles obtained from all observations in six year time period (blue curve), and the histogram of the mean angles obtained from the observations at the times of the enhancements (red curve). c) The histogram of the mean magnitude of the draped IMF obtained from all observations in six year time period (blue curve), and the histogram of the mean draped IMF magnitude obtained from the observations at the times of enhancements (red curve).

timescale corresponding to one Martian year. This variation is caused by the change of the orientation of the rotation axis of Mars with respect to the Sun in a year. If it is zoomed-in to a time in CY 2003 in Figure 3.5a (Figure 2.7), another periodicity, on a ~ 25 day timescale, becomes evident. This is again associated with the solar rotation period [Brain *et al.*, 2006b]. In the IMF mean angle vs. time plot in Figure

3.5, the red dots mark the passes on which the significant enhancements are observed over the region of interest. Their total number is 356 out of $\sim 27,000$. Figure 3.5b presents the histogram of the mean angles obtained by the projection of the data on the right hand side of the plot in Figure 3.5a. The blue curve in Figure 3.5b shows the histogram produced by using all observations over a six year time period while the red curve shows the histogram obtained from the observations at times of enhancements. This plot reveals that the draped IMF angle lies mostly between 230° and 330° (thus oriented westward) during the enhancements. Similarly, the magnitude of the draped IMF is calculated in six years and two histograms are obtained similar to projections shown in Figure 3.5b for the magnetic field magnitude, which are plotted in Figure 3.5c. As seen in this figure, the maximum and the minimum strength of the draped IMF is 100 nT and 5 nT, respectively. Furthermore, the magnitude of the draped IMF lies mostly between 10 and 50 nT in general (blue curve), while it is between 20 and 60 nT at times of the enhancements (red curve).

Having estimated the draping direction of the IMF at the time of the enhancements, next the location of the candidate crustal fields where the low energy electrons originate is discussed in this section. These proposed crustal field candidates also reconnect to the IMF where the photoelectrons start following the field lines which stretch towards tail around the planet resulting in the observed enhancements. The clustering location of the enhancements and the orientation of Mars during late spring and early summer (seasons in which the enhancements occur) suggest that the magnetic crustal fields at 65° S, 150° E are the most probable candidates for the source of the photoelectrons. This location is closest to the enhancements and most active in terms of auroral events. (Most of the auroral events are observed over the region centered at 70° S, 150° E [Brain *et al.*, 2006a].) In Connerney *et al.* [2001], these sources are oriented eastward in the body fixed coordinate system (see Figure 3.6, radially outward field at the west of 150° E and radially inward field at the east of

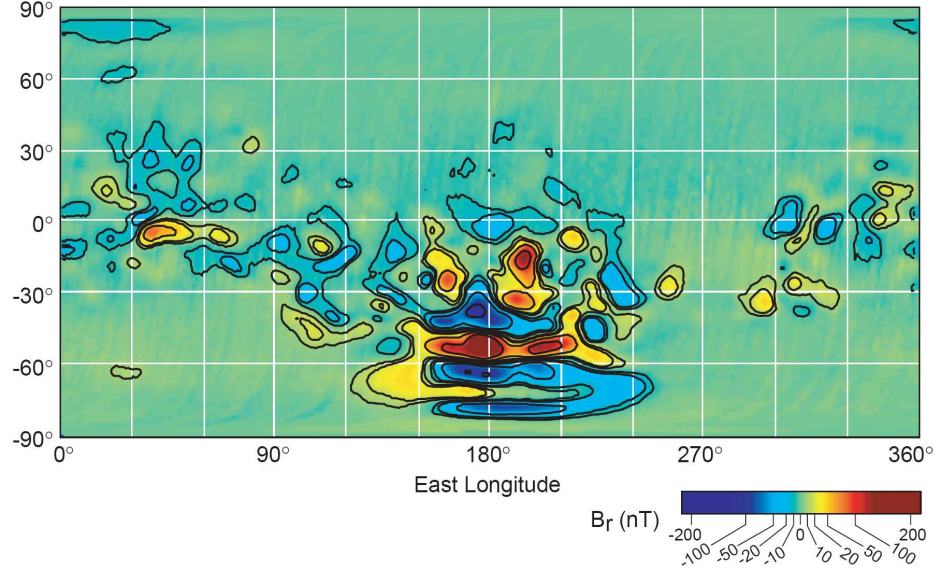


Figure 3.6: Maps of the radial component of the Martian crustal magnetic fields at 400 (+/- 30) km altitude, and colorbar scaled to (+/-)220 nT. (After *Connerney et al.* [2001])

150° E along 65° S). In the above analysis, the direction of the draped IMF at the time of the enhancements is estimated to be westward. This opposite alignment of the draped IMF direction with respect to the proposed crustal fields centered at around 150° E, 65° S verifies the existence of favorable conditions for their reconnection at the times of the enhancement events. Furthermore, the strength of these proposed crustal sources is about 50 nT at 400 km altitude which is also comparable to the strength of the draped IMF at the same altitude. Therefore, the geometry of the planet, the orientation of the crustal sources with respect to the clustering region, and the direction of the draped IMF at the time of the enhancements show that the crustal sources at around 150° E, 65° S may be the origin of the electrons. This conclusion is also what we assume in the rest of the thesis.

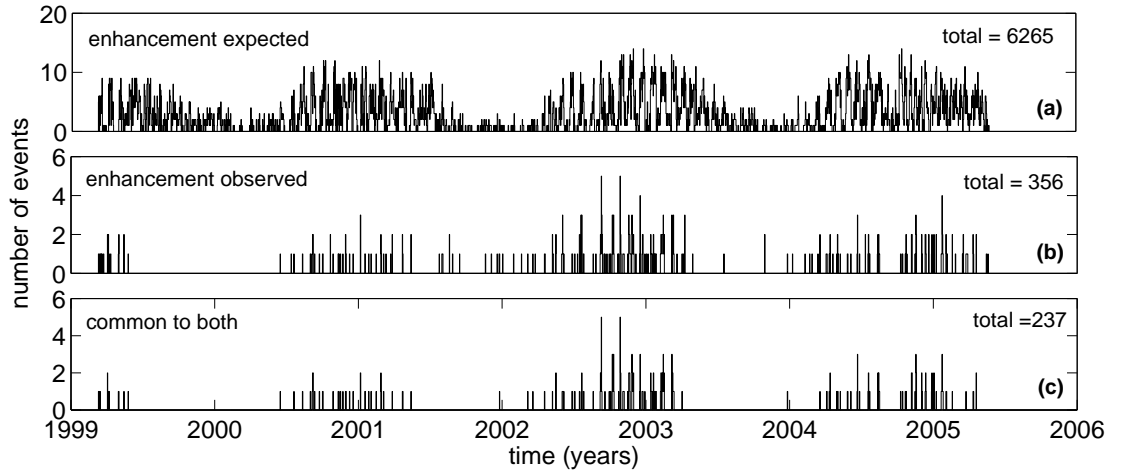


Figure 3.7: Variability of the occurrence of the reconnection conditions and the enhancements with respect to time (years). a) Histogram of the passes when the reconnection conditions were met, and the significant enhancements were expected. b) Histogram of the passes when the significant enhancements were observed. c) Common points of a) and b) indicating the passes on which reconnection was expected and an enhancement was observed.

3.2.4 Explanation for the Seasonal Nature

The seasonal nature of the occurrence of the enhancements (Figure 2.6) can be explained by the seasonal variation of the draped IMF direction. The six histograms presented in Figure 3.7 and 3.8 illustrate the relationship between the draped IMF direction and the seasons. Each histogram was constructed by identifying the passes that met our detection criteria (see below) among all data in an approximately six year time period (all passes are about 27,000 in total). The first three panels in Figure 3.7 are histograms with respect to time while the three in Figure 3.8 are with respect to areocentric longitude of the Sun (L_s , i.e., the Martian northern hemisphere seasons). Figure 3.7a shows the number of the MGS passes when the conditions for reconnection are met, in other words when the IMF is aligned westward; i.e., $230^\circ < \alpha_{\text{IMF}} < 330^\circ$ and the magnetic field strengths are comparable. The total number of these passes is ~ 6200 . Note the seasonal periodicity in the distribution. Figure 3.7b shows the

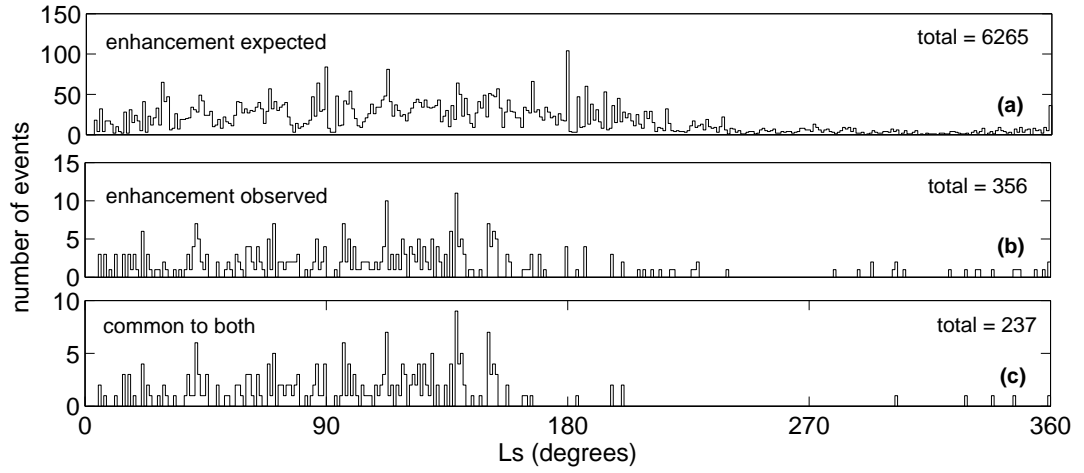


Figure 3.8: Variability of the occurrence of the reconnection conditions and the enhancements with respect to Martian seasons (Ls). a) Histogram of the passes when the reconnection conditions were met, and the significant enhancements were expected. b) Histogram of the passes when the significant enhancements were observed. c) Common points of a) and b) indicating the passes on which reconnection was expected and an enhancement was observed.

number of passes with respect to time in which the enhancements are clearly observed, in a total of 356 passes. Finally, Figure 3.7c shows the common points of Figure 3.7a and 3.7b, which is 237 passes in total. Nearly 70% of the time, when the enhancements are observed, the expected conditions for reconnection were met. The three panels presented in Figure 3.8 illustrate the distribution of the number of the passes with respect to Ls rather than time, with the same criteria used in Figure 3.7. Thus Figure 3.8a shows the number of the MGS passes in which the conditions for reconnection were met, where we also infer the westward alignment of the draped IMF occur most frequently in the late spring and early summer, and least frequently in the late autumn and early winter. Figure 3.8b shows the number of passes in which the enhancements are clearly observed, and Figure 3.8c shows the common points of Figure 3.8a and 3.8b with respect to Ls , indicating clear preference of the enhancements for the first half of the year.

In addition to being the region closest to enhancements and the most active in terms of auroral events, the location of the crustal field sources at $\sim 150^\circ$ E, $\sim 65^\circ$ S is attractive, as it supports our proposal illustrated in Figure 3.2. Accordingly, these sources need to be illuminated by the Sun when the enhancements occur on the nightside. The highest solar zenith angles (SZAs) at which the upper ionosphere and exobase are illuminated are 120° and 110° , respectively, thus requiring that the SZAs of the proposed crustal sources must lie below these values at the times the enhancements are observed. Figure 3.9a illustrates the temporal distribution of the solar zenith angle of this source region at the time of the enhancements (top plot). As shown, most of the time, the SZA of the sources lies below 120° . Furthermore, the eastward foot of the closed field lines should have even lower SZAs considering the relative position of the eastward foot with respect to the center of the source during the northern late spring and early summer (the time period in which the enhancements are observed). This means that the requirement of illumination stated above is satisfied most of the time. Moreover, need for illumination of the potential source region may also be why the enhancements occur mostly in the region from 30° E to 120° E but rarely between 120° and 150° E, and between 330° and 30° E. When MGS samples between 120° and 150° E, the source region resides in the east but still resides in shadow. As Mars rotates, MGS then samples from the region in the west (the region from 30° E to 120° E), and the potential sources move further toward the dayside and become illuminated. It is during that time that MGS records the enhancements. As Mars rotates further, the source region moves toward dusk on the dayside. Thus the enhancements are not observed between 330° and 30° E through 0° . Furthermore, Figure 3.9b shows the temporal distribution of the midlatitude of each enhancement (red dots) and the latitude of the source region (blue dots) at the time of the enhancement in the SS coordinate system. As the Martian season changes from spring to autumn the latitudes decrease. During spring, the source

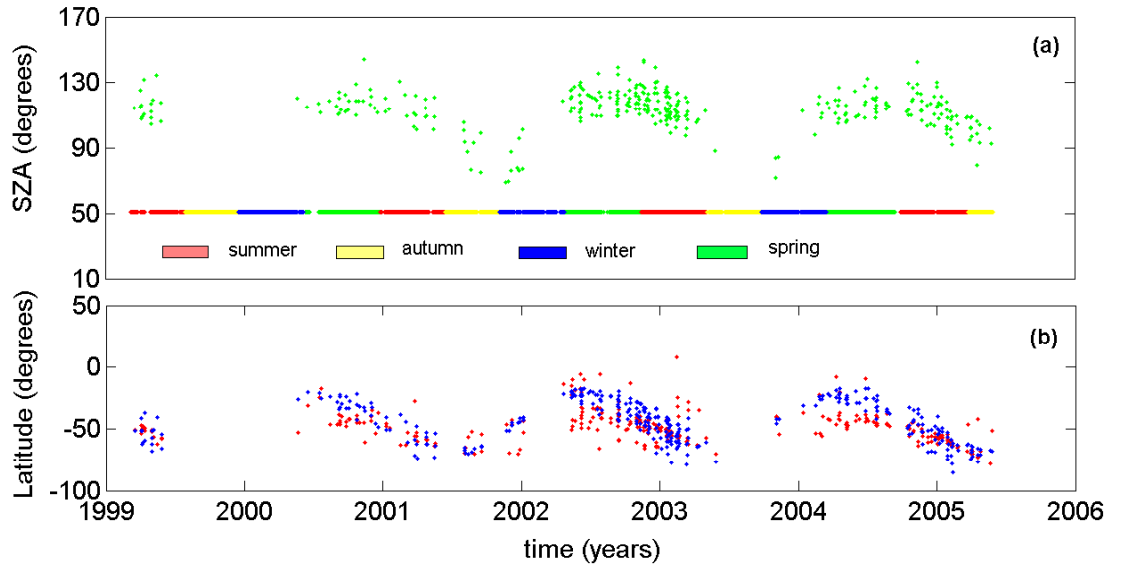


Figure 3.9: a) The solar zenith angles of the potential crustal sources at the time of enhancements. b) The temporal distribution of the midlatitudes of the enhancements (red dots) and of the latitudes of the source region (blue dots) at the times of the enhancements, in the SS coordinate system.

region remains at relatively high latitude at the time it first sees the Sun each day. The source region's position moves to lower latitude in the SS coordinate system as the Martian season changes from spring to autumn due to Mars' axial tilt. Thus Figure 3.9 clearly demonstrates the correlation between the observation location of the enhancements and the relative position of the candidate crustal sources during the events, strengthening the proposal of these sources as the origin of the low-energy electrons seen in the nightside enhancements.

3.3 Effect of the Sun Illumination on the Local Electron Flux

It would be interesting to observe how the electron flux varies in the enhancement region during the day. But, the MGS orbit is fixed at 2 am–2 pm local time, and observing the daily variations in the electron flux distribution directly is not possible with MGS. However, over any given local geographical area, the temporal effect of the solar illumination may indeed be obtained from the MGS data. This is because the position of a local geographical point with respect to the Sun, at the time MGS samples on the 2 am–2 pm meridian, changes due to precession of Mars' tilted rotation axis during the course of a Martian year. Thus MGS samples at the same geographical point over a year can be mapped to samples over one Martian day. Thus a local region between 180° and 210° E, and at around 65° S is chosen to be sampled as described. This region is most interesting in terms of its magnetic and plasma environment where the crustal fields can exceed 200 nT at 400 km, [Connerney *et al.*, 2001] and form closed fields and plasma voids on the nightside [Mitchell *et al.*, 2001]. MGS orbits Mars about every 2 hours and thus passes somewhere over this 30° wide crustal region once a day on the tail side of the terminator plane. The electron flux sequence obtained once a day on the nightside over the six year time period, is plotted in Figure 3.10a (the 19 energy levels from top (10 eV) to bottom (20 keV) with an energy resolution of 25%; six of the energy levels are indicated next to corresponding curves on the right). During the northern late autumn and early winters, the region resides on the dayside of the terminator plane. Since the plot in Figure 3.10a includes only the nightside data, the sequence has gaps corresponding to the times of northern late autumn and early winters. In late spring and early summer, the region is in the deep dark at the time MGS takes samples, and thus the electron flux drops to the instrument background level due to loss of electrons via recombination and absorption

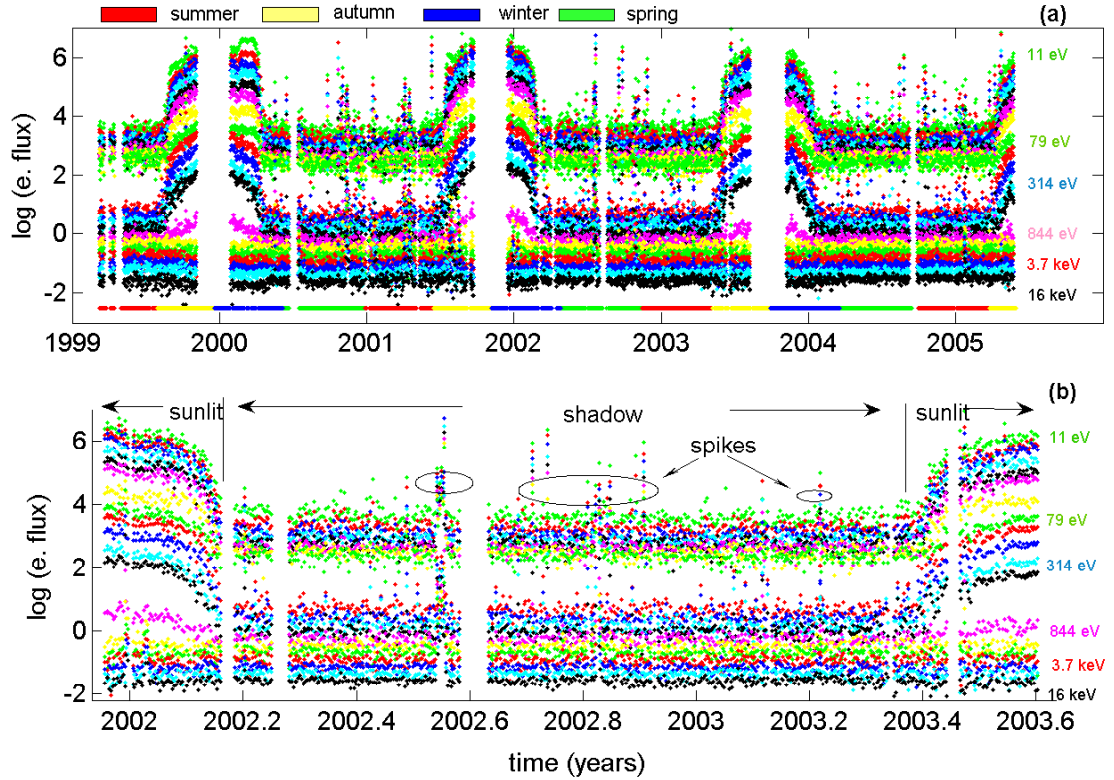


Figure 3.10: Temporal electron flux distribution over the closed crustal fields between $180^\circ \pm$ and $210^\circ \pm$ E at $\sim 65^\circ \pm$ S. a) The logarithm of the omnidirectional electron fluxes at 19 energy levels (logarithmically spaced from 10 eV (top) to 20 keV (bottom) with an energy resolution of 25%). b) Zoomed-in view of the electron flux during CY 2003. In Sun shadow, the electron flux drops to or below instrument background level revealing plasma voids (region marked under "shadow"). As the region is illuminated by the Sun, electron fluxes increase gradually filling the voids with photoelectrons (region marked under "sunlit"). "Spikes" seen in shadow are either due to the ambient electrons that can reach the voids such as aurora over nearby cusp regions or the disturbances driven by the transient solar ejections.

[*Mitchell et al.*, 2001]. As the region moves from deep dark towards the edge of the terminator plane in late winter and early autumn, it starts to receive solar radiation at $\sim 60^\circ$ S, and the corresponding rise in the low-energy electron flux is apparent on the plot (see the zoomed-in view of the sequence during CY 2003 in Figure 3.10b). The spike-like fluctuations in the night time may be either due to ambient electrons

that can reach void regions, as explained in *Mitchell et al.* [2001], or to aurora seen in the neighborhood of the void [*Brain et al.*, 2006a]. These impulses in the intensity may also be driven by a sudden energy release or disturbance associated with solar flares or coronal mass ejections (CMEs) as they reach Mars or may even be caused by penetrating particles leading to anomalously high instrument background during certain periods such as passing CMEs.

To observe the time evolution of the significant enhancements, we further investigated the enhancement region by using the same method described above. In Chapter 2, we showed that the geographical area for the significant enhancements lies between 30° and 120° E at $\sim 70^\circ$ S. Furthermore, in this area most of the enhancements reside in a narrower band between 60° and 90° E (see Figure 2.4). To see the effect of the Sun striking this region, the electron fluxes (sampled on the tailside of the terminator plane once a day over the six year time period) are plotted in Figure 3.11a. In this figure, each sample represents the average of the data that fall in the 5° wide latitude band around 70° S. During the northern late autumn and early winters, the region resides on the dayside of the terminator plane. Since the plot in Figure 3.11a. includes only the nightside data, the sequence has gaps corresponding to the times of northern late autumn and early winters. A very interesting property of this plot is the emergence of the significant enhancement as spike-like outgrowths of the low-energy electron fluxes. Zoomed-in view of the draped IMF direction (Figure 3.11a) at around CY 2003 is plotted in Figure 3.11b over the electron flux distribution plot in Figure 3.11c. A closer look at Figure 3.11b and 3.11c reveals that when the reconnection conditions are periodically met (top panel, red dots), the low-energy flux enhancements occur periodically on an approximately 25 day timescale. (Note also that during some enhancements the highest energy channels, have elevated fluxes as well, which may be the result of passing transients in the solar wind such as CMEs, possibly penetrating particles artificially elevating the instrument count rate.) This

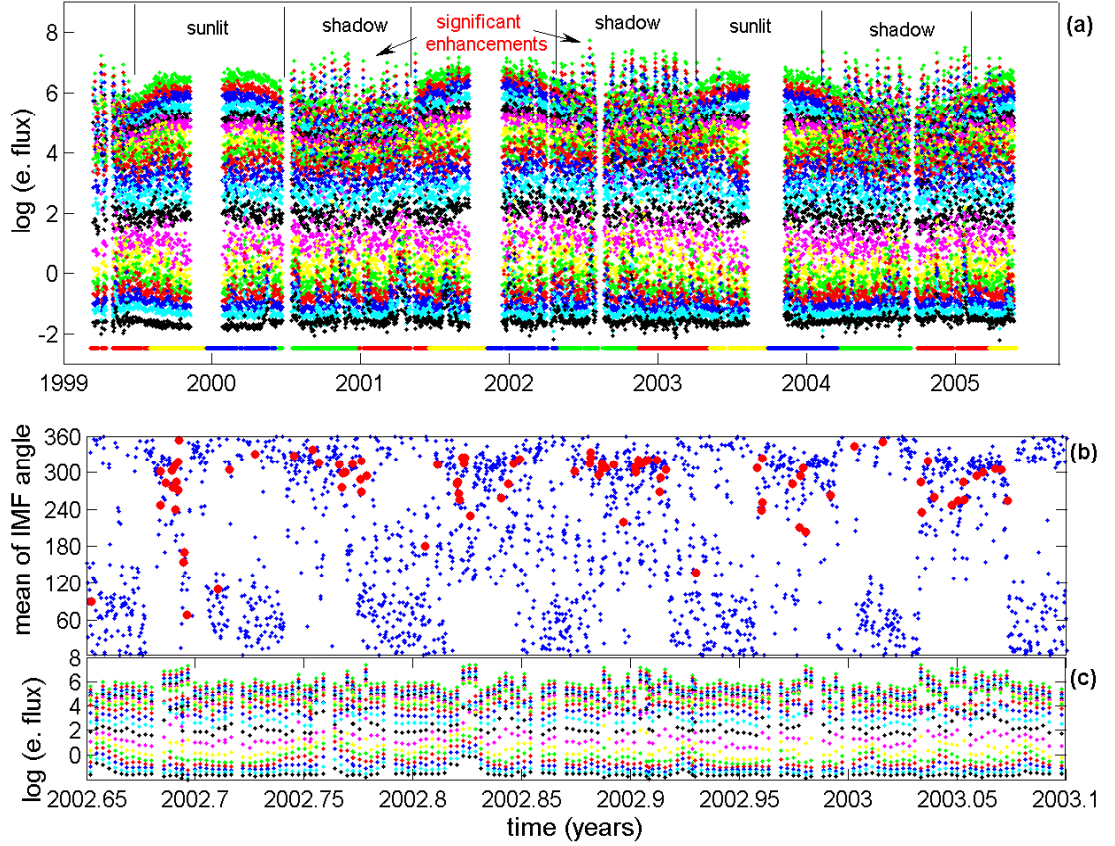


Figure 3.11: Temporal electron flux distribution over the geographical region for the significant enhancements (between $60^\circ \pm$ and $90^\circ \pm$ E at $\sim 70^\circ \pm$ S.) a) The logarithm of the omnidirectional electron fluxes at 19 energy levels (logarithmically spaced from 10 eV (top) to 20 keV (bottom), with an energy resolution of 25%). Spike-like outgrowths at the low energy levels are attributed to the significant enhancements. The enhancements are mostly observed in shadow, and there is a gradual increase in the typical nightside electron flux levels as the region starts to see the Sun (area marked as "sunlit") b) Expanded view of the estimated draped IMF angle during CY 2003 (from Figure 6a). The red dots mark the enhancements. c) Expanded view of the electron flux during CY 2003. The enhancements are recognized by two orders of magnitude increase at the low energy levels and occur on a nearly 25 day periodic timescale coinciding with the westward alignment of the draped IMF.

feature of the events was revealed in Chapter 2 in a different way, by calculating the normalized magnitude of the ~ 116 eV omnidirectional electron flux as a function of the fluctuation period, and the ~ 25 day periodicity was evident in the plot in Figure

2.7. This evident correlation of the draped IMF direction with the enhancements suggests that the occurrence of enhancements is more likely when the draped IMF has a westward direction than when the IMF is oriented elsewhere. Moreover, in Figure 3.11a, note the effect of solar illumination on the density of the electrons: as the season changes from early summer to late autumn, the region moves from deep dark towards the terminator plane and thus the electron flux level increases from the typical nightside value to typical dayside value. This increase corresponds to the time when this region reaches $\sim 60^\circ$ S in the SS coordinate system and is illuminated by the Sun. This effect is similar to that seen over the crustal fields mentioned previously but less pronounced. These two examples in Figures 3.10 and 3.11 clearly demonstrates the general Sun illumination effect on the near Mars plasma. The first example (Figure 3.10) explicitly shows the voids, and the second example (Figure 3.11) explicitly shows the enhancements observed on the nightside.

3.3.1 Summary

In this chapter, the possible physical explanations for the observed electron flux enhancements are discussed and it is concluded that these events are different from the auroras and current sheets previously observed at Mars. Moreover, the local and periodic nature of the events makes other possible sources such as ionospheric irregularities, plasma clouds, or sudden energy release or disturbances from the Sun unlikely to be the source for this phenomenon. The phenomenon is interpreted as the transportation of the photoelectrons above the crustal magnetic sources on the dayside to the magnetotail on the nightside of Mars along the lines of the reconnected IMF. Although this interpretation of the events implies the existence of signatures of ionospheric photoelectrons in the spectra of the enhancements, the MGS ER instrument can not distinguish the peaks. One reason may be that the energy resolution of the ER instrument is too coarse to resolve their peaks, and the other reason may be

the dispersion at low energies due to further particle interactions during the events. However, a smoothed peak between 100 eV and 2.5 eV is detected in the averaged spectrum, and it implies the presence of sheath plasma along with the planetary plasma during the enhancements supporting our interpretation.

Moreover, our proposed scenario requires reconnection of the draping IMF lines with the local crustal magnetic fields. With the fact that reconnection is more likely when the field lines from two neighboring plasma domains are aligned anti-parallel and similar in magnitude, the draping direction of the IMF was estimated at the time of the enhancements using the dayside magnetic field data over the northern hemisphere where crustal fields are absent. The results showed that at the time of the events, the draped IMF mostly oriented westward, and its strength ranges from 20 and 60 nT. The crustal sources at 65° S, 150° E are proposed to be the origin of the low energy electrons observed during the enhancements. There are four critical reasons why these crustal fields are proposed to be the source: (i) The geographic location is closest to the enhancements. (ii) It is most active in terms of auroral events. (iv) The strength of these sources is about 50 nT at 400 km altitude. (iii) The sources in this location are oriented eastward, i.e., anti-parallel to the IMF. The opposite alignment of the draped IMF with respect to these sources and similarity of the field strengths confirms the existence of favorable conditions for magnetic reconnection at the time of the events. In addition, the seasonal nature of the enhancements are explained by the seasonal variation of the draped IMF direction. And finally, by determining the SZAs of the proposed crustal source location, we showed that these sources are illuminated by the Sun during the time enhancements occur, which is also what our interpretation requires.

In conclusion, during the enhancements, the draped IMF and the crustal sources at 65° S, 150° E are mostly aligned anti-parallel, and the strength of the draping IMF and the crustal sources are similar at 400 km altitude. This condition favors

reconnection of these two fields and supports our proposal of electron transport from dayside to the nightside by these reconnected field lines around Mars. Moreover, the geometry of Mars, orientation of the sources with respect to clustering region at the time of the enhancements, and the low energy and periodic nature of the events further supports our physical explanation of the events.

Chapter 4

Model of the Solar Wind Interaction with Mars

The present chapter introduces a model which describes the average magnetic field configuration around Mars resulting from its solar wind interaction using a semi-empirical-analytical approach to account for the observed electron flux enhancements.

4.1 Introduction

In the last three decades, several models in a variety of complexity have been developed for the description of the Martian solar wind interaction. The simplest model applies gasdynamic theory in order to derive the plasma flow around the Martian obstacle by assuming that Mars is weakly magnetized [*Spreiter and Stahara*, 1980; 1992]. In this model, magnetic field configuration and plasma parameters are derived from the plasma flow and only in the magnetosheath. The gasdynamic model description does not give results for the part of the dayside and all of the nightside of the planet. Furthermore, this simple model is not adequate to describe the physics of the interaction accurately as it excludes the effects of dominant magnetic fields

A more accurate description of the interaction of the solar wind with Mars can be obtained by using MHD models, which treat the plasma as a single conducting fluid by solving the hydrodynamic equations with Maxwell's equations simultaneously [Tanaka, 1993; Liu *et al.*, 1999; Shinagawa and Bougher, 1999; Ma *et al.*, 2002; Harnett and Winglee, 2003; Ma *et al.*, 2004; Harnett and Winglee, 2006]. This formulation is particularly useful in modeling large scale and relatively low frequency plasma phenomena. In other words, in MHD formulation, the particles in the plasma are assumed to stick together so that their motion is represented by the motion of local center of mass. Therefore, even fluid treatment of the flow may not be adequate as the kinetic effects are ignored in this approach. Hybrid models accounting for the kinetic effects have been developed as well and allowed for more reliable description of the exact nature of the interaction [Brecht, 1997]. The solution of these sophisticated models require super computers using parallel computation techniques for long run time periods. These models describe the interaction more accurately and reliably, but they are computationally much more demanding and time-consuming.

In this thesis, another approach is taken for the description of the Martian solar wind interaction based on a semi-empirical-analytical formulation of the interaction. A computationally simple model is developed by utilizing as much physical information as possible and by employing analytical expressions for reproducing the physical features of the interaction.

4.2 Semi-empirical-Analytical Modeling

In this section, a semi-empirical-analytical model is developed to describe the magnetic field around Mars that reflects the general features of its solar wind interaction. The final outcome of the model is the description of the magnetic field configuration around Mars. As stated in the previous chapter, our explanation of the electron

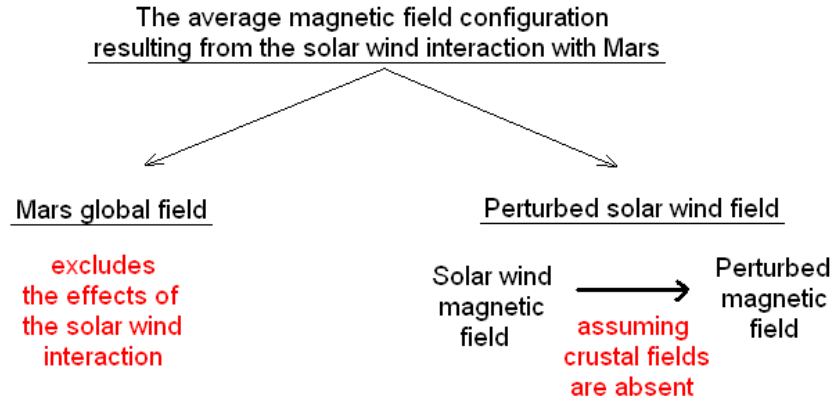


Figure 4.1: Two components of the magnetic field around Mars, resulting from the Martian solar wind interaction: Mars global field and Perturbed solar wind field. The average magnetic field configuration is derived from the vector superposition of these two fields.

enhancements involves reconnection of the IMF with the local crustal fields. Thus the principle objective of this modeling is to obtain physically reasonable solution for the magnetic field resulting from the solar wind and crustal field interaction. In this model, the general magnetic field configuration is obtained from the combination of two separate field topologies. The first is the global magnetic field of Mars, due primarily to the regional crustal sources and with the assumption that excludes all external effects induced during the solar wind interaction. The second component is the perturbed solar wind field, which is derived from the proton flow around the Martian obstacle, assuming Mars has neither global field nor local crustal fields. An overall magnetic field is then obtained from the vector superposition of these two fields. The diagram shown in Figure 4.1 illustrates this approach schematically and in the following sections, each of these steps is explained separately.

Before providing the details of each step, it should be noted that although this model reproduces the main features of the Martian solar wind interaction, it is not self-consistent. In reality, the solar wind plasma passes through the field of strongest crustal sources, and the motion of the plasma alters the magnetic field over the crustal

sources. Simple vector superposition of the two fields does not accurately reproduce this dynamic feature. Additionally, our model neglects other dynamic processes such as mass loading of the solar wind planetary pick-up ions and the outflow of ions in the Martian tail. However, with the current simple model, rather than describing the details of the plasma-field interaction, we aim to approximate the magnetic field configuration over the proposed crustal sources. The vector sum of two field topologies that fill the same volume over the sources gives the first order approximation of the overall magnetic field and thus predicts reconnection regions. Because over the regions where the two field lines are anti-parallel and equal in strength, the overall field will be canceled, similar to the case in Figure 3.3. Over the regions where one of the field topologies is dominant, the other field will be negligible. Therefore, by summing the two field topologies (Mars global and perturbed solar wing magnetic fields) over the crustal sources, the regions where reconnection may take place can be predicted. Further, the results from our semi-empirical-analytical model have been compared with the results obtained from a self-consistent four-ion single fluid MHD model, developed previously by colleagues at University of California, Los Angeles (UCLA). The description of this model, and the analysis and discussion of the results are included in a separate chapter (Chapter 5).

4.3 Mars Global Magnetic Field

The first component of our magnetic field model is the global magnetic field of Mars. Since the discovery of the crustal fields (by *Acuña et al.* [1999]), many different models with different complexity and source data have been developed for their representation, most of which are mainly adaptations of models used for the Earth's global field. The first of the Martian global field representations is constructed by *Purucker et al.* [2000], who used an equivalent source technique to produce a map

of the radial field at 200 km altitude. In this model, the magnetization of each of 11,550 radially oriented equally spaced magnetic dipoles is obtained using the low altitude pre-mapping phase and nighttime mapping phase magnetometer data of MGS. In order to minimize the effects of the external fields, only the radial component of the magnetic field measurements is used in his model. However, this approach is not sufficient to remove external effects completely. Another drawback of this model is the non-zero divergence over any closed surface near the crustal sources. In the light of these drawbacks, another model is chosen for the representation of the internal global field of Mars.

Cain et al. [2003] created an internal potential field model for Mars using a selection of full-vector MGS MAG observations. In this model, the Martian crustal sources are represented by modifying the spherical harmonic expansion (SHA) model that was first developed for the Earth's global field (for more information about SHA models, see Appendix A) . Since the Martian field is local and more complicated than the Earth's global field, this expansion for Mars has a much higher degree (up to 90). This high degree yields 8280 independent parameters to determine from the MGS MAG measurements. Therefore, in their model they used nearly 120,000 low altitude (below 200 km) aerobraking (AB) and the Science Phase (SPO) orbits, and high altitude (367–435 km) nighttime Mapping Phase (MPO) orbits vector measurements. As they report in their work, use of low and high altitude data at the same time allows for a more accurate representation of the field and better exclusion of the external effects: The low-altitude dayside AB data provide finer detail in describing the crustal fields while using the nighttime MPO data reduces the contributions of the external effects that may be present in AB and SPO data. Moreover, in this model, the values of the highest degree coefficients are individually and statistically insignificant, but their combined use provides adequate representation of the small-scale variations of the magnetic field. The details of their work can be found in [*Cain et al.*, 2003].

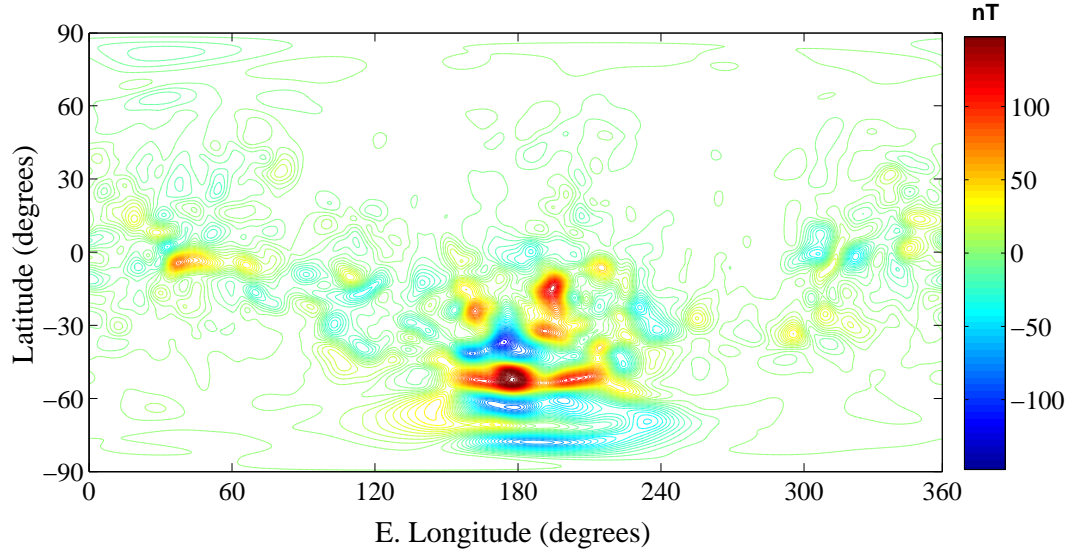


Figure 4.2: Contours of the radial component of the crustal magnetic fields over a spherical surface at 400 km altitude at Mars, which is obtained using the coefficients spherical harmonic expansion model of *Cain et al.* [2003].

Another reason that makes this model attractive is the agreement of this model to previously published maps and models. In their work, *Cain et al.* [2003] shows that that this model is in general agreement with the other models at around 400 km altitude. However, below 200 km altitude, errors can reach 20 nT, which is also the value close to the reported model uncertainty [*Cain et al.*, 2003]. Moreover, this potential function reproduces the Martian magnetic field more closely to the observations than any existing representation because, as reported in the same paper, *Cain's* model reduces the largest misfits to the AB and SPO data by a factor of 5 from prior published models [*Cain et al.*, 2003]. Therefore, we chose this model to use in our model for the representation of the Martian internal global field assuming that it excludes the external effects completely. Figure 4.2 illustrates a map of radial component of the magnetic field obtained over a surface at 400 km altitude using the 8280 coefficients of *Cain's* spherical expansion model.

4.4 Perturbed Solar Wind Magnetic Field

The perturbed solar wind magnetic field is the second component of our model. This field represents the modified solar wind magnetic field as the solar wind flows around the Martian obstacle when Mars is assumed to have neither global nor local crustal magnetic fields but a substantial ionosphere.

Several techniques (MHD, hybrid, gas-dynamic, empirical models) exist to simulate the solar wind flow around an ionospheric obstacle [*Spreiter and Stahara*, 1992; *Kallio*, 1996]. As stated previously, we chose to apply a simple semi-empirical-analytical model for this representation. A similar approach was first applied to Mars by Wallis and Johnstone in 1983. In their study, velocity of the solar wind flow around the obstacle is represented by analytical functions, and the plasma parameters are derived from these analytical functions. Similarly, in 1996, *Kallio* developed a model to describe the proton flow around Mars using the Automatic Space Plasma Experiment with a Rotating Analyzer (ASPERA) 3-D vector velocity observations of Phobos-2 mission [*Kallio et al.*, 1993;1994]. At the time of his study, Martian crustal sources were not discovered yet, but from Phobos-2 observations, it was known that Mars has a very weak intrinsic magnetic field compared to the Earth's dipole field [*Lundin et al.*, 1991]. Therefore, based on the Phobos-2 velocity observations, *Kallio* assumed Mars is weakly magnetized in his model. In this thesis, we use the same model as that of *Kallio*'s but modify some of the functions and update the parameters of the analytical expressions using recent Mars orbiter observations. The details of *Kallio*'s work can be found in *Kallio* [1996]; however, all necessary details and updates of his model are included in this chapter.

There are three important features of this model: The first is that it is simple and not computationally costly, which makes it easy to analyze its responses to different model parameter variations. The second is that it enables us to describe the field

in all plasma regions where the solar wind plasma can reach near Mars. The last is that it describes the field in three dimensions. As it will be clearer in the following sections, this feature is only possible by assuming that velocity of the flow is axially symmetric with respect to the line passing through the Sun and Mars. Although in reality, the plasma velocity near Mars is not axially symmetric, the Martian solar wind interaction can still be derived to good approximation from this first order approximation of the flow.

Following the same strategy in *Kallio's* model, the major plasma boundaries near Mars are determined in mathematical representations. The flow velocity is defined between these boundaries using the same analytical functions of the *Kallio's* model, and the parameters of these expressions are updated utilizing the most recent information. And eventually, the magnetic field configuration is obtained around Mars from the flow velocity by applying the Ohm's law, which is valid only when the magnetic field is frozen-in the plasma flow. Each step used for the derivation of the perturbed solar wind field is explained in detail in the following sections.

4.4.1 Interaction Boundaries

Previously, it is discussed that Mars presents primarily an ionospheric obstacle to the solar wind. Although strong crustal sources cause local deviations from this simple ionospheric structure, the basic features of ionospheric interaction dominate near Mars. The two major boundaries typical in this type of interaction are the Bow Shock (BS) and the Magnetic Pile-up Boundary (MPB) as introduced in Chapter 2. In this section, the analytical expressions for these two major plasma boundaries near Mars are determined in order to use them in the foundation of the flow velocity in the next section. As explained in Chapter 2, the bow shock position is not influenced by the crustal fields, but the location of the MPB varies significantly as the crustal fields' position changes. Therefore, in our model, a representation of the MPB is used

which is obtained far from these sources.

In his analytical model, *Kallio* used a conic function and an even fourth order polynomial for the representation of the bow shock and the MPB (which was called magnetopause by *Kallio*), respectively. The parameters of these functions are based on the observations of Phobos 2, Marinar 4, and Mars 2, 3, and 5 missions [*Slavin et al.*, 1991]. In our study, two conic sections are used for the representation of these two boundaries, and the parameters of these functions are adapted from the *Vignes et al.* [2000]. In their work, these parameters are obtained from the statistical study of 450 boundary crossings on 290 MGS orbits. Moreover, in their paper, comparison of the position and shape of these boundaries to previously published estimations presents good agreement, which gives us further confidence in using these expressions in our model.

$$r_f = r_f(\theta_f) = \frac{L}{1 + e \cos(\theta_f)} \quad (4.1)$$

Equation 4.1 gives the formula of a conic function. It is expressed in polar coordinates with a cylindrical symmetry along the x -axis, which points at the Sun. θ_f is the angle measured about the focus from the x -axis and r_f is the distance between a point on the bow shock surface at an angle θ_f and the focus of the function, located at x_0 (see Table 4.1). The value of r_f is L (the semi-latus rectum) when θ_f is 90° . e represents the eccentricity of the boundary surface.

In our model, both the bow shock and the MPB are represented by two conic functions. The first line of Table 4.1 shows the value of the parameters used for the representation of the bow shock [*Vignes et al.*, 2000]. A total of 480 bow shock crossings of MGS were used in the linear regression to fit the geometric characteristics of this boundary. Bow shock crossings are identified in MGS data by an increase in the interplanetary magnetic field over a short period of time. During the same period, the electron fluxes, with energy ranges between 11 eV and 300 eV, increase by a factor

Table 4.1: Conic function parameter values of *Vignes et al.* [2000] fits

	Mission	Number of crossings	Subsolar stand-off	Terminator stand-off	x_0 (R_M)	ϵ	L (R_M)
Bow shock	MGS	450	$1.65(R_M)$	$2.6(R_M)$	0.7	1	2
MPB	MGS	488	$0.96(R_M)$	$1.29(R_M)$	0.78	0.9	0.96

10. This boundary is shown by the green line in Figure 4.3. In this figure, the Sun is on the right, and the x -axis points at the Sun. Axial symmetry applies with respect to the x -axis, and r represents the radial distance from the x -axis. For the rest of the chapter, all figures are shown in the same coordinate system (MSO). As can be inferred from the figure, the bow shock is the outermost boundary from the planet and its distance to Mars is greater near the terminator plane: The subsolar stand off distance is $1.65R_M$ while the terminator stand off distance is $2.80R_M$ ($R_M=3390$ km). The second line of Table 4.1 shows the value of the conic function parameters for the representation of the MPB. A total of 450 MPB crossings of MGS are used in the boundary fitting analysis. The MPB crossings are identified in MGS data by three simultaneous signatures: a sharp increase of the magnetic field magnitude, a decrease in the fluctuations of the magnetic field, and a decrease of the electron fluxes greater than 10 eV [*Vignes et al.*, 2000]. The electron flux decrease is sharp, which is typically about one order of magnitude and interpreted as a consequence of electron impact ionization by *Crider et al.* [2000]. The increase in magnitude and decrease in the fluctuations of the magnetic field were previously identified in the Phobos 2 data by *Riedler et al.* [1989], and thus *Kallio's* boundary representations are similar to the ones we use in our model. The subsolar stand-off distance of the MPB is $\sim 1.29R_M$ while the terminator stand-off distance is $1.47R_M$. This asymmetric nature of this boundary is evident in Figure 4.3, where the MPB is shown by the red curve. Here, it should be noted that although we used these average representations for both boundaries (the bow shock and MPB), they are highly variable in reality. It should

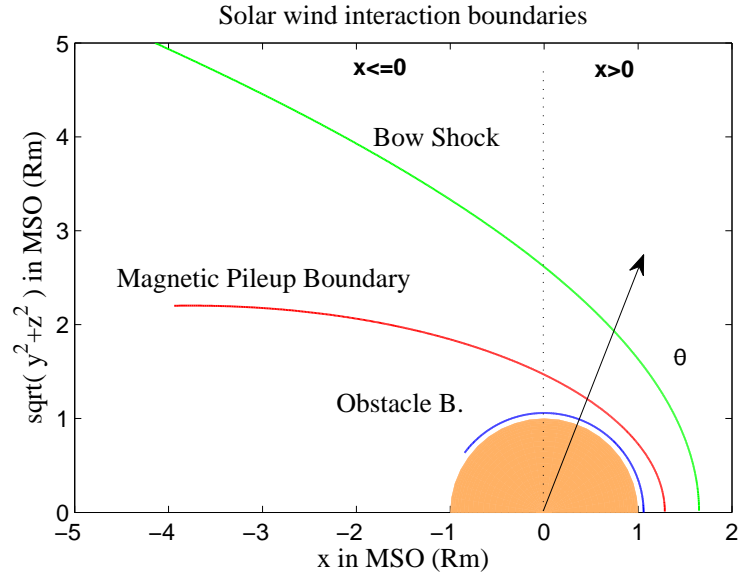


Figure 4.3: Bow shock and MPB fits in MSO coordinate at Mars obtained from MGS observations.

also be noted that this representation of the boundaries imply cylindrical symmetry along the x -axis which is not actually true. The asymmetry observed in the solar wind flow velocity at Mars implies an asymmetry in the draping of the flow around obstacle, resulting in global asymmetry in the interaction boundaries. However, this large scale variation seen in the draping of the flow does not change the dominant draping direction of IMF, which is $-y$ in our case. Since the principle purpose is to investigate the reconnection conditions over the proposed crustal sources, it is still assumed that this large scale asymmetry does not significantly influence the draping IMF direction and thus the results.

$$x^2 + \rho^2 = R_{OB}^2 \quad (4.2)$$

$$\rho = 1400 \left[\tanh \left(\frac{3270 - |x|}{600} \right) + 1 \right] \quad (4.3)$$

In our model, a third boundary is used for the representation of the ultimate

obstacle at Mars to the solar wind plasma. This boundary is located between the MPB and the surface of Mars and forms a tangential discontinuity by preventing solar wind plasma from passing through. For the analytic representation of this boundary, a hemi-spherical surface at 170 km altitude is used on the dayside, similar to *Kallio's* model (see Equation 4.2). The altitude of this dayside boundary coincides with the upper boundary of the exosphere at Mars, and it is shown by the blue curve in Figure 4.3. On the nightside, this hemispherical surface is elongated by using the expression in Equation 4.3, which will serve as a guiding line for the convergence of the flow on the nightside. The details of this approach are explained in the following section while defining a velocity flow model.

4.4.2 Velocity Field of the Proton Flow

In this section, the velocity field of the proton flow around Mars is described analytically, which reproduces the observed features of the observed flow, in particular the sharp decrease in the velocity magnitude at the bow shock and MPB. Another observation is that the velocity field presents a tangential discontinuity at the obstacle boundary, where the solar wind plasma can not move closer to the planet and deviate around it. Moreover, the velocity field should be capable of describing the plasma flow on the nightside, as the satellite observations at Mars show that the particle flux observed on the Martian tail is nonzero. In order to describe a velocity field that carries these physical features, the strategy used by *Kallio* was employed here: First the velocity jumps are determined on previously defined plasma boundaries, and then the direction and the magnitude of the velocity are determined between these boundaries both on the dayside and the nightside. This strategy also requires axial symmetry of the velocity model with respect to the x -axis as shown in Figure 4.4.

Considering the axial symmetry, the velocity vector is expressed in two different field components: V_x , representing the velocity along the x -axis, and V_ρ , representing

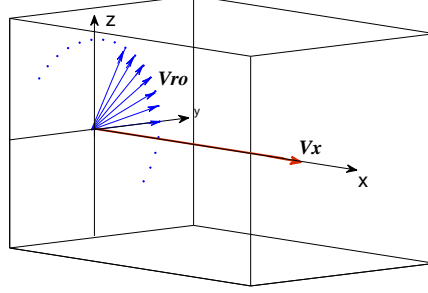


Figure 4.4: Axial symmetry in the velocity model with respect to the x -axis, which points at the Sun.

the velocity perpendicular to V_x (see Figure 4.4). Furthermore, in the description of these components, the magnitude and the direction of the velocity is defined separately. In mathematical terms:

$$V_x(\mathbf{r}) = V(\mathbf{r}) \cos [\varphi_{v_{Lc}}(\mathbf{r})] \quad (4.4)$$

$$V_\rho(\mathbf{r}) = V(\mathbf{r}) \sin [\varphi_{v_{Lc}}(\mathbf{r})] \quad (4.5)$$

where V is the magnitude of the velocity at a point, \mathbf{r} , and $\phi_{v_{Lc}}$ is the angle that the velocity vector makes with the $-x$ axis at the point \mathbf{r} . Here, Lc in the subscript is an independent parameter which represents the plasma passing through the MPB. In *Kallio's* model the MPB is called magnetopause, and it is used for modeling an open magnetosphere, which means that the part of the solar particles penetrate the magnetopause. In our model, as it will be clearer in the following paragraphs, Lc controls the amount of the plasma that pass through the MPB.

Magnitude of the flow velocity

The analytical expressions for the velocity magnitude, V , are adapted from *Kallio* [1996], which are developed using Phobos-2 ASPERA velocity observations. Because the spacecraft measured the dayside magnetosheath and then penetrated deep inside

the Martian tail, these expressions define the velocity in all plasma regions at Mars. The magnitude of the velocity is defined by the product of two velocity fields:

$$V = V_{\text{BS}} V_{\text{MPB}} \quad (4.6)$$

These separate fields, V_{BS} and V_{MPB} , are used to imitate the jumps in the velocity magnitudes at the bow shock and the MPB, respectively. Therefore, hyperbolic tangent functions that can reflect these jumps are chosen for the description of both V_{BS} and V_{MPB} . In addition, both functions represent the velocity magnitude relative to solar wind bulk speed, and thus their magnitudes range from 0 to 1. Thus overall velocity magnitude, V , also takes values between 0 and 1. Here it should also be noted that, for the simplicity of the analysis, *Kallio* used different coordinate systems to describe the flow on the dayside and nightside. Spherical coordinates are employed for the dayside flow description, and cylindrical coordinates are used for the nightside (see Figure 4.3). The following expressions (Equations 4.7 and 4.8) illustrate these velocity magnitude functions in their corresponding coordinate systems.

$$V_{\text{BS}}(r, \theta) = \frac{h_{\text{BS}}(\theta)}{2} \left[\tanh \left(\frac{r - r_{\text{BS}}(\theta)}{L_{\text{BS}}} \right) - 1 \right] + 1, x > 0 \quad (4.7)$$

$$V_{\text{BS}}(\rho, x) = \frac{h_{\text{BS}}(x)}{2} \left[\tanh \left(\frac{\rho - \rho_{\text{BS}}(x)}{L_{\text{BS}}} \right) - 1 \right] + 1, x \leq 0 \quad (4.8)$$

In these functions, h_{BS} represents the decrease in the velocity magnitude at the bow shock while the solar wind plasma approaches Mars. L_{BS} is the width of the bow shock which is chosen to be constant and 0.5. r_{BS} is the radial distance of the bow shock on the dayside while r_{BS} is the distance of the bow shock on the nightside. r and ρ show the distance of a general point on the dayside and on the nightside,

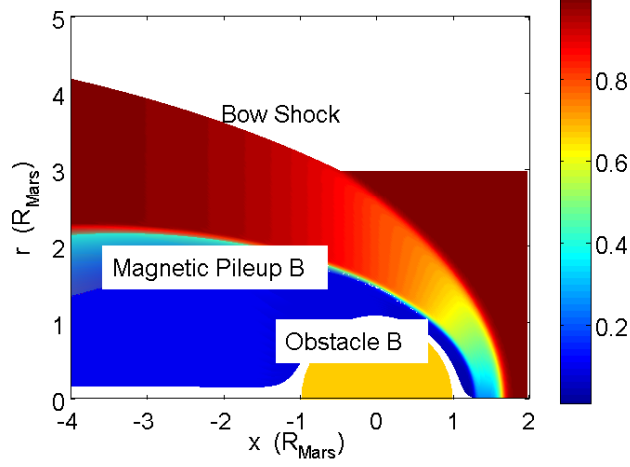


Figure 4.5: Relative velocity magnitude of the flow with respect to solar wind speed.

respectively.

$$V_{\text{MPB}}(r, \theta) = \frac{h_{\text{MPB}}}{2} \left[\tanh \left(\frac{r - r_{\text{MPB}}(\theta)}{L_{\text{MPB}}} \right) - 1 \right] + 1, x > 0 \quad (4.9)$$

$$V_{\text{MPB}}(\rho, x) = \frac{h_{\text{MPB}}}{2} \left[\tanh \left(\frac{\rho - \rho_{\text{MPB}}(x)}{L_{\text{MPB}}} \right) - 1 \right] + 1, x \leq 0 \quad (4.10)$$

Similarly these functions represent a velocity magnitude having a jump at the MPB which is constant, h_{MPB} . The width of the MPB is L_{MPB} , and r_{MPB} and ρ_{MPB} describe the distances of the MPB on the dayside and the nightside, respectively.

The relative speed of the plasma flow around Mars with respect to solar wind speed obtained by using the expressions above is plotted in Figure 4.5. As seen in the figure, the relative magnitude of the velocity is 1 upstream from the bow shock, and the speed decreases as plasma approaches the planet. The jumps at the bow shock and MPB are evident in the figure. At the bow shock, it drops to one forth of its upstream value, and at the MPB it decreases by a factor of 10. The plasma speed in the magnetosheath drops dramatically close to subsolar point. Toward the terminator plane, plasma speed increases gradually and reaches its upstream value at

the terminator plane, which is consistent with the observations.

Direction of the flow velocity

Having determined the magnitude of the velocity field of the flow, next we determine the direction of the flow. As mentioned previously, our strategy is to define the velocity angle first on the boundaries and then to derive it between the boundaries by applying linear interpolation, same as in *Kallio's* model. At the bow shock, normal component of the velocity is assumed to decrease to one fourth of its upstream value (assuming infinite Mach number) while the tangential component is assumed to remain constant.

At the MPB, the direction of the velocity vector is defined by the amount of the plasma that passes through the boundary. If all particles pass through, the velocity normal component with respect to the MPB surface remains zero if no flux passes through the velocity vector will be tangential to the surface. When the solar wind plasma partially penetrates the boundary, the velocity normal component of the flow becomes nonzero at the MPB. In order to control the amount of the plasma that passes through the MPB a free parameter, Lc , is used. The same parameter in *Kallio's* model was used to determine how open or close the magnetosphere was assuming that Mars has a very weak internal dipole field. In his model, $Lc = 0$ represents the totally closed magnetosphere forming an impenetrable boundary while $Lc = 90$ implies no detectable boundary that can resist to flow of the plasma. A value in between 0 and 90 implies partial penetration of the solar wind plasma into the magnetosphere. In our model, this value is used as a test parameter which controls the plasma flux passing through the MPB. This control is achieved by the method *Kallio* employed, which is decreasing ϕ_{MPB} by subtracting a positive number from it. This positive number is chosen to be a function of Lc . This method is expressed mathematically in the following equation. An Lc value between 0 and 90 implies that the velocity

normal component of the flow becomes nonzero at the MPB.

$$\phi_{Lc,MPB}(\theta) = \phi_{MPB}(\theta) - \phi_{Lc}(\theta) \quad (4.11)$$

$$\phi_{Lc}(\theta) = 90e^{(-\theta/Lc)} \quad (4.12)$$

The positive function, Lc , in the above formula is chosen to be an exponential function (Equation 4.12). The decrease rate of $\phi_{Lc}(\theta)$ from 90 to 0 is determined by the Lc parameter and makes the function fulfill the boundary conditions $\phi_{Lc}(\theta)=90$ and $\phi_{Lc}(\theta)=0$. Note that because $\phi_{Lc}(\theta)$ is 0 for $\theta=90$, it does not affect the flow on the nightside.

Finally, the direction of the velocity vector is determined at the ultimate obstacle boundary which is an impenetrable surface. In mathematical terms, the ϕ_{OBS} angle creates a discontinuity forcing the velocity vector to be tangential over the obstacle boundary surface. Between these three boundaries the direction of the velocity vector is calculated by linear interpolation along the constant θ line on the dayside and along the constant x line on the nightside. Figure 4.6 illustrates the flow lines of the solar wind plasma through defined boundaries near Mars. In this figure Lc is 20, which is also the value chosen for the final model of the velocity field to be used in our overall solar wind interaction model. The decrease of ϕ_{MPB} is clearly seen in the second panel at the MPB which implies the partial plasma penetration through it.

The analytical proton velocity model adapted from *Kallio's* work has a solution for the flow direction both on the nightside and the dayside of the planet. However, it should be noted that the flow on the nightside, inside the magnetic pile up region above the ultimate boundary, is a first order approximation to a realistic flow on the nightside. It is applied due to the limitations of the *close enough* measurements to Mars in this region. The analytical expressions used for this description based on the need of the nightside convergence of the plasma that passes through the MPB on the

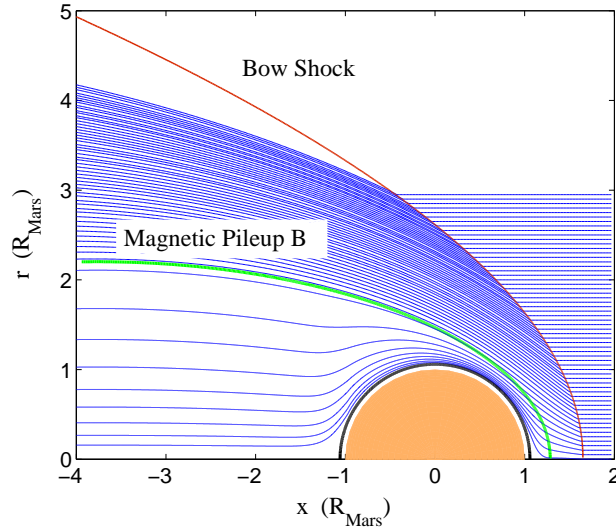


Figure 4.6: Direction of the flow velocity around Mars.

dayside and to reproduce nighttime plasma observations of Phobos-2 in the Martian tail [Kallio, 1996]. Since these 3-D nighttime plasma measurements are not enough to determine precisely the direction of the flow in the center tail, The nightside description of the flow in the center tail is the least realistic part of this model. However, the crustal sources that are proposed to reconnect to the draping IMF lines are located far away from the center tail but close to the terminator plane. Thus this region is represented well in the model, and reliable conclusions can still be derived from the current model.

In summary, in this section the proton velocity field near Mars is modeled by using analytical functions that reproduce the observations in different plasma regions near Mars. In our model, the same analytical functions used in Kallio's model are utilized to describe the magnitude of the proton velocity after updating their parameters with the most recent information. The magnetic field configuration of the Martian solar wind interaction is derived from this flow velocity model assuming that the magnetic field is frozen-in the proton flow.

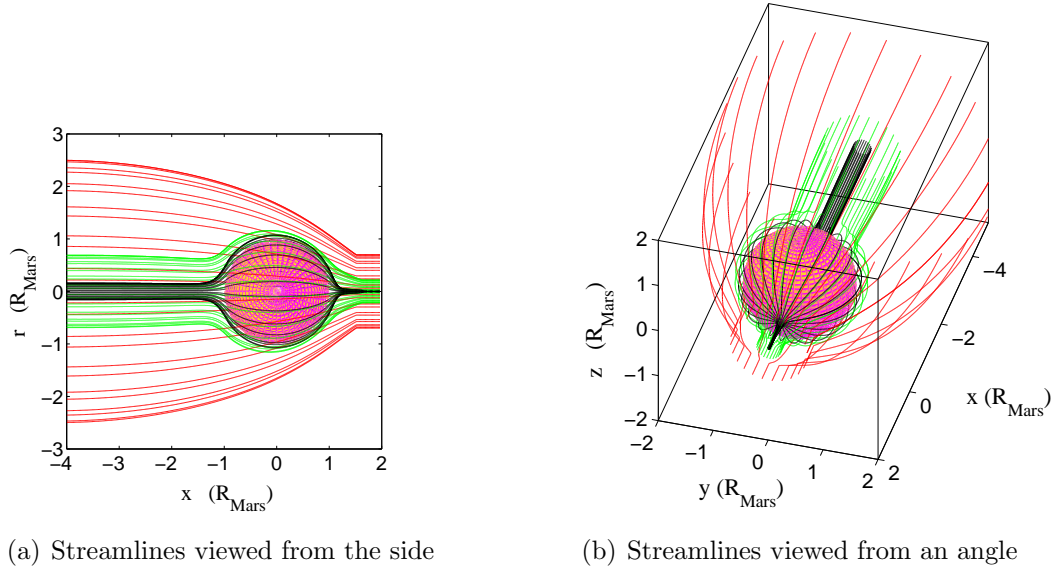


Figure 4.7: Path of the protons around Mars in the defined velocity field. Different colors represent the streamlines in different plasma regions: Red streamlines pass through the bow shock and remain in the magnetosheath. The blue lines pass through first the bow shock and then MPB and remain below the MPB. Similarly, green lines pass first the bow shock and then MPB but these lines are very close to the planet as they enter the magnetosheath at a point that is very close to subsolar point (a) View of the streamlines from the side of the planet. (b) View of the same streamlines in (a) from an angle..

4.4.3 Streamlines of the Protons around Mars

In this section, the paths of the solar wind protons are obtained, as they flow around Mars according to our velocity model.

Figure 4.7 shows these paths in color. We obtain each streamline by tracing the path of each proton which moves according to the velocity field defined in the previous section. Different colors represent the protons that lie in different plasma regions: Red streamlines represent the protons that pass through the bow shock and remain in the magnetosheath before they move far away from the planet. The boundary of the different plasma regions can be recognized by identifying the deviations in the paths of the individual protons. For instance, on the red lines the bow shock can

be identified by the point where the lines start bending on the dayside. The blue lines represent the streamlines that pass through first bow shock and then MPB and remain below the MPB. Similarly, green lines pass first the bow shock and then MPB but these protons moves very close to the planet as they enter the magnetosheath at a point that is very close to subsolar point. The second panel in Figure 4.7 shows the same streamlines from a different view angle for better visualization in 3-D.

4.4.4 Perturbed Solar Wind Magnetic Field

In this section, the perturbed solar wind magnetic field is derived from the proton flow in all plasma regions near Mars. This derivation is based on the assumption that magnetic field is frozen-in the solar wind flow. In other words, the solar wind flow is treated as conducting fluid and assumed to be flow dominated. In the introduction, the plasma beta was calculated as ~ 100 near Mars, which is a strong indication that solar wind plasma near Mars is flow dominated. Although this value may not remain constant everywhere during the solar wind interaction with Mars, it is assumed to be large enough in all plasma regions so that our assumption is valid.

The determination of the electric field in magnetized plasma is based on the generalized Ohm's law, given by the Equation 4.13.

$$\mathbf{E} = -\mathbf{u}_m \times \mathbf{B} - \frac{\mathbf{J} \times \mathbf{B}}{N_{e0}q_e} - \frac{\nabla \cdot \Psi_e}{N_{e0}q_e} + \bar{\eta} \cdot \mathbf{J} + \frac{m_e}{N_{e0}q_e} \frac{\partial \mathbf{J}}{\partial t} \quad (4.13)$$

Here, \mathbf{u}_m is the velocity of the fluid, \mathbf{J} is the current density, $\bar{\eta}$ is the receptivity tensor, N_{e0} electron number density, Ψ_e is the pressure tensor, m_e electron mass, q_e electron charge. If it is assumed that fluid is isotropic and both the Hall effect and ambipolar polarization are negligible, and time variations are small scale, the

generalized Ohm's law reduces to Equation 4.14.

$$\mathbf{J} = \sigma(\mathbf{E} + \mathbf{u}_m \times \mathbf{B}) \quad (4.14)$$

The simultaneous solution of Equation 4.14 with the Maxwell's equations yields Equation 4.15.

$$\frac{\partial \mathbf{B}}{\partial t} = \nabla \times (\mathbf{u}_m \times \mathbf{B}) + \frac{\nabla^2 \mathbf{B}}{\mu_0 \sigma} \quad (4.15)$$

For highly conducting plasma ($\sigma \gg 0$), Equation 4.15 yields the following expression (Equation 4.16).

$$\frac{\partial \mathbf{B}}{\partial t} = \nabla \times (\mathbf{u}_m \times \mathbf{B}) \quad (4.16)$$

By simple modification, the following expression can be derived from Equation 4.16.

$$\frac{d}{dt} \left(\int_A \mathbf{B}(\mathbf{r}, t) \cdot d\mathbf{A} \right) = 0 \quad (4.17)$$

Equation 4.17 is the mathematical definition of a frozen-in magnetic field condition. It implies that all particles and magnetic flux contained in a certain flux tube at a certain instant remain inside the same flux tube at all instants, independent from any motion of the flux tube. Another interpretation of this equation is that a particle that initially lies on a magnetic field line stays on the same line at all times. This feature of the plasma enables us to derive information about the plasma parameters from the deformation that occurs during the movement of plasma. Then, this information can be utilized to determine the perturbed solar wind magnetic field configuration around the planet.

Direction of the Magnetic Field

Note that line deformation (1-D deformation) in a magnetized plasma gives information about the orientation of the magnetic field. Let us place a number of fluid

elements on a magnetic field line in the solar wind and connect the positions of these elements to form a line, D_0 lying along the magnetic field line. If the ideal Ohm's law is valid, dt times later, connection of the fluid elements' positions will form a new line, D , which is the deformation of D_0 due to the movement of the fluid elements on the given velocity field. Since all fluid elements should still lie on the same field line, the orientation of D is also the orientation of the magnetic field at dt . In mathematical terms, the frozen-in magnetic field criteria means that if a vector say $\mathbf{e}(r_0, t_0)$ lies on a magnetic field line $\mathbf{B}(r_0, t_0)$ at $t = t_0$, in dt time period $\mathbf{e}(r_0, t_0)$ deforms to $\mathbf{e}(r, t)$ which lies on $\mathbf{B}(r, t)$. Formally then we have

$$\frac{\mathbf{B}(\mathbf{r}_0, t_0)}{|\mathbf{B}(\mathbf{r}_0, t_0)|} = \mathbf{e}(\mathbf{r}_0, t_0) \quad (4.18)$$

$$\frac{\mathbf{B}(\mathbf{r}, t)}{|\mathbf{B}(\mathbf{r}, t)|} = \mathbf{e}(\mathbf{r}, t) \quad (4.19)$$

Obtained using the above method, Figure 4.8 illustrates the draping of the solar wind magnetic field around Mars in 3-D. In this figure, x -axis point at the Sun, the velocity of the solar wind plasma is in $-x$ direction, and the magnetic field of the approaching solar wind is in y direction. The field lines show how magnetic field lines bend as they pass the planet. In order to obtain these lines, a number of protons are placed on two magnetic field lines at $x=2R_M$; one lies above the ecliptic plane and the other is below the ecliptic plane. The first two field lines on the dayside of the planet show these two field lines where the protons reside initially. Then, the paths of these protons are traced which move according to our velocity field model. Connecting the positions of the protons at different time instants yields the field lines in the figure. The protons that lie on the field line above the ecliptic plane move over the northern hemisphere and creates the field lines over the northern hemisphere while the protons that lie on the field line below the ecliptic plane move over the southern hemisphere creating the field lines over the southern hemisphere. As clearly seen in the figure,

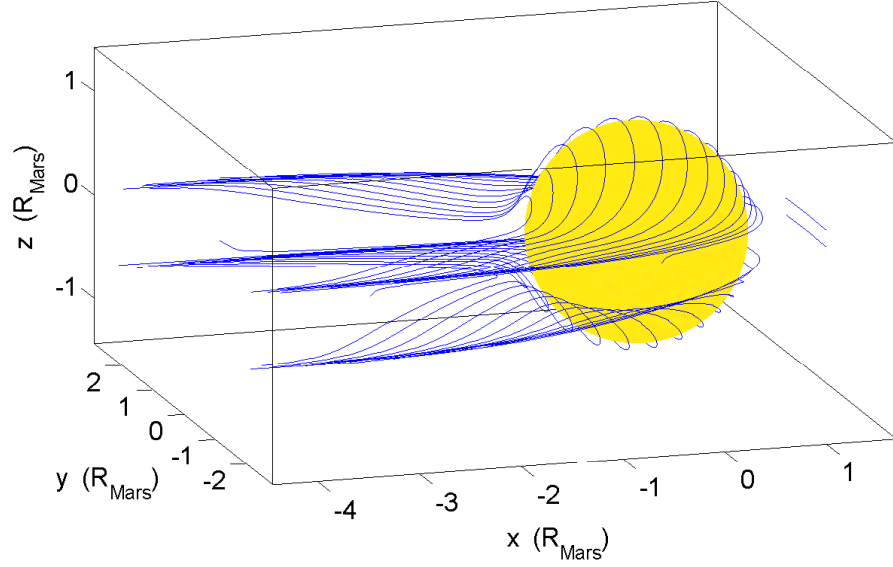


Figure 4.8: Draping perturbed solar wind field lines around Mars.

the magnetic field lines bend and slide over the poles of the planet. It should also be noted that since the velocity of the protons decrease in the magnetosheath and in the MP region, the protons that lie on the part of the field lines outside magnetosheath move faster resulting in the stretch of the field lines as they move close to the planet. Furthermore, the sharp decrease in the velocity at the MPB causes pileup of the magnetic field lines in front of this boundary. This pile up of the field lines results in a rise in the magnetic field strength, and it will be confirmed after the magnitude of the magnetic field is obtained in the following paragraphs.

Magnitude of the Magnetic Field

While line deformation (1-D) gives information about the direction, area (2-D) deformation provides information about the magnitude of the magnetic field in the plasma.

$$\frac{d}{dt} \left(\int_A \mathbf{B}(\mathbf{r}, t) \cdot d\mathbf{A} \right) = 0 \quad (4.20)$$

Let A define an area in plasma. If the ideal Ohm's law is valid everywhere,

the magnetic flux through A remains constant as it moves with the plasma in time, according to Equation 4.20. Furthermore, if it is assumed that the area is small compared to the scale of the change of the magnetic field, we can further assume that the magnetic field is constant over the surface and can thus calculate the strength of the magnetic field everywhere. Let $\mathbf{B}_A(r_0, t_0)$ be the average magnetic field at the time $t = t_0$ on the surface $A(r_0, t_0)$ with a normal $\mathbf{e}(r_0, t_0)$, and $\mathbf{B}(r, t)$ be the average magnetic field at $t = t$ on the surface $A(r, t)$ with a normal $\mathbf{e}(r, t)$. The quantity $A(r, t)\mathbf{e}(r, t)$ is the area formed by the deformation of $A(r_0, t_0)\mathbf{e}(r_0, t_0)$ after a time period $dt = t - t_0$.

$$\mathbf{B}(\mathbf{r}_0, t_0) \cdot [A(\mathbf{r}_0, t_0)\mathbf{e}(r_0, t_0)] = \mathbf{B}(\mathbf{r}, t) \cdot [A(\mathbf{r}, t)\mathbf{e}(r, t)] \quad (4.21)$$

$$B_A(\mathbf{r}_0, t_0)A(\mathbf{r}_0, t_0) = B_A(\mathbf{r}, t)A(\mathbf{r}, t) \quad (4.22)$$

Here $B_A(r_0, t_0)$ and $B_A(r, t)$ are the magnetic field magnitudes along the normals of $\mathbf{e}(r_0, t_0)$ and $\mathbf{e}(r, t)$, respectively. In order to obtain \mathbf{B} in three directions, similar equations can be written for three areas with normal vectors in three orthogonal directions. Let three perpendicular areas be $A_i(r_0, t_0)$, $A_j(r_0, t_0)$, $A_k(r_0, t_0)$ and let their normal vectors be $\mathbf{e}_i(r_0, t_0)$, $\mathbf{e}_j(r_0, t_0)$, $\mathbf{e}_k(r_0, t_0)$. These areas deform into new areas $A_i(r, t)$, $A_j(r, t)$, $A_k(r, t)$ and the normal vectors $\mathbf{e}_i(r_0, t_0)$, $\mathbf{e}_j(r_0, t_0)$, $\mathbf{e}_k(r_0, t_0)$ deform into $\mathbf{e}_i(r, t)$, $\mathbf{e}_j(r, t)$, $\mathbf{e}_k(r, t)$ as the fluid elements move in time. If the ideal Ohm's law is valid everywhere, the magnetic flux through the areas remain constant. Assuming that these areas are small compared to the scale change of the magnetic field and the magnetic field is constant over the surfaces, magnetic field strengths in three directions can be calculated by the following formulas.

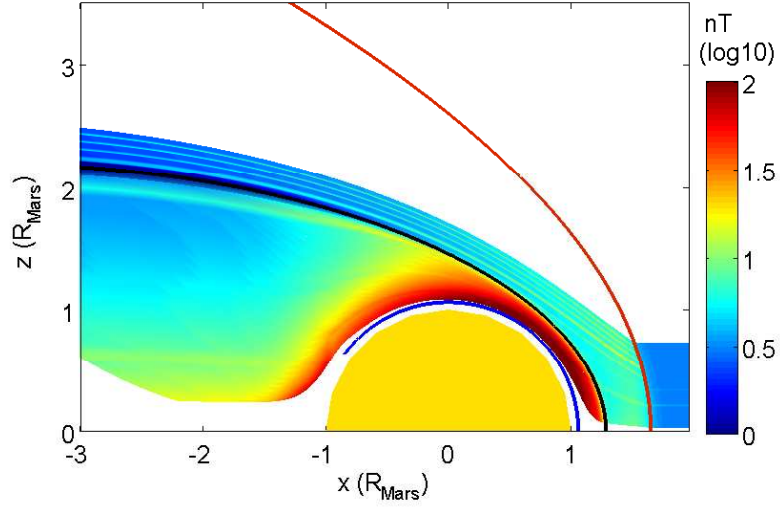


Figure 4.9: Magnitude of the perturbed solar wind field around Mars over the xz plane in the MSO coordinate system.

$$B_i(\mathbf{r}, t) = \frac{A_i(\mathbf{r}_0, t_0)}{A_i(\mathbf{r}, t)} B_i(\mathbf{r}_0, t_0) \quad (4.23)$$

$$B_j(\mathbf{r}, t) = \frac{A_j(\mathbf{r}_0, t_0)}{A_j(\mathbf{r}, t)} B_j(\mathbf{r}_0, t_0) \quad (4.24)$$

$$B_k(\mathbf{r}, t) = \frac{A_k(\mathbf{r}_0, t_0)}{A_k(\mathbf{r}, t)} B_k(\mathbf{r}_0, t_0) \quad (4.25)$$

Obtained using the above method, Figure 4.9 shows the strength of the perturbed solar wind magnetic field over a cross-section on the xz plane as it flows around a weakly magnetized Mars. In this figure, the color scale indicates the magnetic field magnitude. The x -axis points at the Sun, the velocity of the solar wind plasma is in $-x$ direction, and the magnetic field of the solar wind is in $-y$ direction with strength of 3 nT. Since the model has an axial symmetry only half of the cross-section is shown. All plasma boundaries near Mars are clearly identified in this figure. The increase in the magnetic field strength from 2 nT to ~ 10 nT at the bow shock is consistent with the observations. As expected, the pile up of the field lines in front of the MPB results in a sharp increase in the magnetic field magnitude. The maximum strength of the

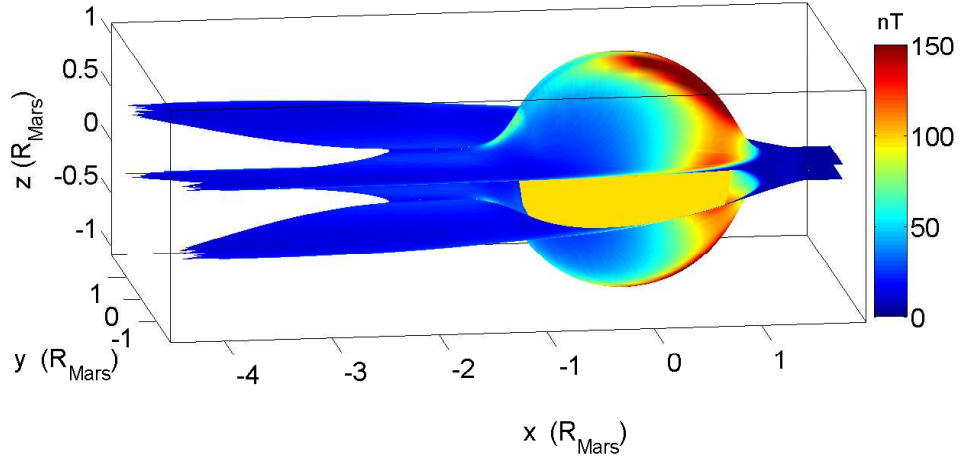


Figure 4.10: Magnitude of the magnetic field over a surface formed by the field lines in Figure 4.8.

magnetic field at the MPB is ~ 100 nT for an IMF strength of 3 nT. In Figure 4.9, the impenetrable obstacle boundary is distinguished by the absence of solar wind plasma beyond the boundary. Similarly, Figure 4.10 is obtained using the same method, and illustrates the magnetic field strength distribution over the surface formed by the field lines shown in Figure 4.8.

4.5 Results: Combined Global Field

1-D and 2-D deformations in the solar wind, which move according to our velocity model, provide a full description of the perturbed solar wind field around Mars. The axial symmetry in the velocity model results in a symmetry in the magnetic field with respect to a plane whose normal is perpendicular to both the solar wind velocity and IMF direction (evident in Figure 4.8 and 4.10). This feature enables us to reduce the numerical computation and save time and memory in the computation of the model. The perturbed solar wind magnetic field configuration around Mars

is thus obtained for the solar wind conditions under which the enhancements are observed. The strength of the solar wind magnetic field is chosen as 3 nT and its direction is chosen along $-y$. For these values, the draping direction of the IMF over the potential sources is westward and its strength is comparable to the strength of the crustal sources suitable for their reconnection. Moreover, the value of the free parameter, L_c , is adapted from *Kallio's* model for this case, which is 20.

Similarly, the Mars global field is obtained from the *Cain's* spherical harmonic expansion model [*Cain et al.*, 2003] for the planetary conditions under which the enhancements are observed. Mars northern hemisphere is in summer, i.e., L_s is 90 and Mars is tilted about 25° toward the Sun. Moreover, the subsolar point is at 45° N, which is the typical subsolar latitude at which the enhancements are observed.

Figure 4.11a shows Mars global field obtained from the 90-element spherical harmonic model superimposed to the external field which is the perturbed solar wind field. The second panel in Figure 4.11b shows the zoomed-in view of Figure 4.11a over the potential crustal sources. This location is also where reconnection is expected and the origin of the stretched field lines from the dayside to the nightside is located.

Finally, the Mars global internal magnetic field and the perturbed solar wind field are linearly superposed to approximate the overall magnetic field configuration near Mars. Figure 4.12a shows this combined field obtained from the two fields. Similarly, Figure 4.12b shows the zoomed-in view of Figure 4.12a over the potential crustal sources. As seen in this figure, over the regions where strong crustal sources are dominant, they close on themselves (which corresponds a region at around 180° E, 45° S below 600 km altitude in the body-fixed coordinate system). However, over the crustal sources which we propose to be the origin of the photoelectrons (the sources centered at around 150° E and 65° S), the crustal field strength is comparable to draping field strength at around 400 km altitude, and the two fields align anti-parallel. Therefore, over this region vector superposition causes cancelation of the

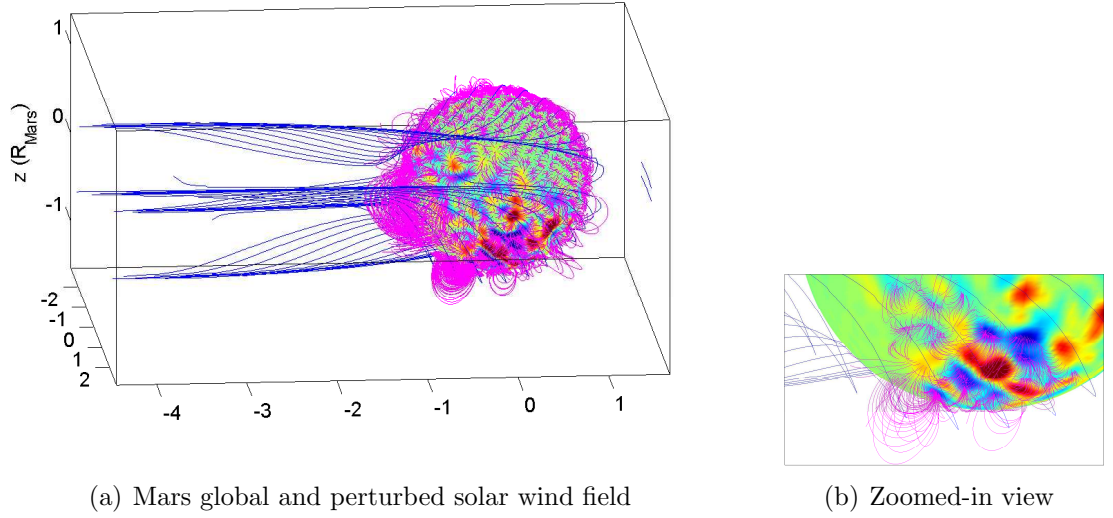


Figure 4.11: Two field line topologies shown in blue and magenta, which form the overall magnetic field around Mars resulting from the Martian solar wind interaction. (a) The blue lines are the perturbed solar wind field lines, obtained from *Kallio*'s model. The purple field lines are Mars global magnetic field lines, obtained from *Cain*'s spherical harmonic expansion model. Color indicates the map of the crustal fields at 400 km altitude and projected to the Martian surface. (b) Zoomed-in view of (a) over the potential crustal sources.

fields resulting in a drop in the field strength at this altitude. However, at low altitudes over the same region, crustal fields dominate and thus one end of the field lines connects to the surface where the crustal fields originate. The other end of the field lines connect to draping IMF lines at high altitudes as the IMF dominate at relatively high altitudes. These signatures in the magnetic field topology are the features of the reconnection, and simple vector superposition is therefore capable of reproducing these, letting us observe reconnection over the potential crustal sources. Therefore, as seen in Figure 4.12, the field lines originate from the potential crustal sources and stretch toward the tail. This result is consistent with our interpretation of the events and thus accounts for the events under the assumptions of our model.

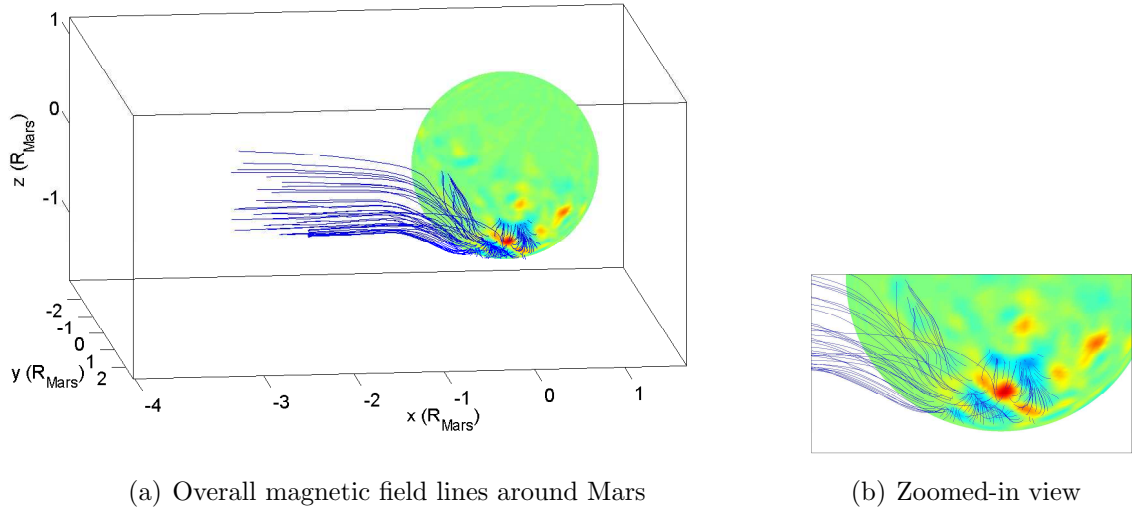


Figure 4.12: Overall magnetic field lines obtained from the vector superposition of Mars global field and perturbed solar wind field. Color indicates the map of the crustal fields at 400 km altitude and projected to the Martian surface. (b) Zoomed-in view of (a) over the potential crustal sources.

In conclusion, our simple semi-empirical-analytical model shows that reconnection of the crustal fields and the draping IMF is feasible over the sources centered at around 150° E and 65° S under the conditions observed at the time of the events. The observed electron enhancements are likely the transport of the photoelectrons along the reconnected field lines around Mars. Therefore, the results from the simple model are consistent with this interpretation. These results alone are not sufficient to conclude that our interpretation is the only mechanism underlying these events. A more physically realistic model is required for the accurate accounting of the observed phenomena. Therefore, in the next chapter, we introduce and investigate the application of MHD modeling to the Martian solar wind interaction and compare the results of the simulations with the conclusions obtained in this chapter.

Chapter 5

Magnetohydrodynamic Modeling Results

In this chapter, we present the results of a four-ion single-fluid MHD simulation of the Martian solar wind interaction that was applied for the physical conditions under which the electron flux enhancements were observed, to investigate the mechanisms responsible for these enhancement events. Furthermore, the simulation results from this MHD model, which describes the effects of crustal fields on the interaction, are compared to the results from our simple semi-empirical-analytical model developed in the previous chapter.

5.1 Introduction

As stated in the previous chapter, several models with varying degrees of complexity have been developed for the description of the Martian solar wind interaction. Studies of this interaction using MHD approaches date back more than a decade. A large-scale solar wind interaction with the ionosphere of non-magnetized planets is numerically simulated using a 2-D and 3-D MHD models for years [*Tanaka, 1997; Shinagawa and*

Bougher, 1999; *Liu et al.*, 2001]. Although the results from these models are in general agreement with the observations, effects of the crustal sources on the interaction can not be simulated using these models as the magnetic field of Mars is ignored in these models. 3-D ideal MHD simulations of the Martian magnetosphere, using a magnetized Mars, were carried out by *Ma et al.* [2002]. In this study, it is shown that the position of the ionopause depends on the location of the crustal sources, and magneto-cylinders form on the nightside. However, this model can not resolve the magnetic pileup boundary and can not make accurate predictions about the affect of the anomalies. Previous 3-D single fluid non-ideal simulations of the solar wind interaction with magnetized Mars by *Harnett and Winglee* [2003; 2005; 2006] include some non-ideal MHD physics such as Hall effects, capture the particle type effects occurring within the magnetosphere, and resolve the MPB. However, in these results, the spatial resolution was low and the model did not include mass loading effects.

In this chapter, the simulations from a four-species single fluid MHD model are analyzed. This model was developed by *Ma et al.* [2004] to describe the Martian solar wind interaction including the effect of the crustal magnetic sources. As stated previously, we aim to explore the physical explanation of the observed enhancement events: The results presented here are obtained from model calculations carried out by *Yingjuan Ma* for a special case (personal communication with Ma), which corresponds to the solar wind conditions and Mars orientations under which the enhancements are observed. Below, we only briefly describe the model; while detailed information about the model can be found in the dissertation of *Yingjuan Ma* and [*Ma et al.*, 2002; 2004].

5.1.1 MHD Modeling of Solar Wind Interaction with Mars

5.2 Model Details

In a four-species single-fluid MHD model results are obtained from the simultaneous-numerical solution of a set of transport equations (a number of continuity equations, one energy equation, and one momentum equation) with Maxwell's equations. These equations are derived from the well known Boltzmann equation which describes the dynamic behavior of a gas species in a fluid and can be written for each species in the fluid.

$$\frac{\partial}{\partial t} f(\mathbf{r}, \mathbf{v}, t) + (\mathbf{v} \cdot \nabla_{\mathbf{r}}) f(\mathbf{r}, \mathbf{v}, t) + \left(\frac{\mathbf{F}}{m} \cdot \nabla_{\mathbf{v}} \right) f(\mathbf{r}, \mathbf{v}, t) = \left[\frac{\partial f(\mathbf{r}, \mathbf{v}, t)}{\partial t} \right]_{\text{coll}} \quad (5.1)$$

$$\mathbf{F} = m\mathbf{G} + q(\mathbf{E} + \mathbf{v} \times \mathbf{B}) \quad (5.2)$$

In this equation, force can be replaced by the Lorentz and gravitational forces (Equation 5.2). The velocity distribution function, $f(\mathbf{r}, \mathbf{v}, t)d\mathbf{v}d\mathbf{r}$, describes the probable number of particles found at time t in the element $d\mathbf{r}$, possessing velocities between \mathbf{v} and $d\mathbf{v} + \mathbf{v}$. This function gives the full statistical information on all of the particles. However, without solving for $f(\mathbf{r}, \mathbf{v}, t)$, macroscopic quantities such as number density, mean velocity, temperature, and pressure can be deduced by multiplying Equation 5.1 with a function and integrating it over the entire velocity space. The three equations, obtained by using mass, momentum, and energy as the multiplication factor, give the continuity, momentum, and energy conservation equations,

respectively:

$$\frac{\partial n}{\partial t} + \nabla \cdot (n\mathbf{u}) = \frac{\delta n}{\delta t} \quad (5.3)$$

$$mn\left(\frac{\partial \mathbf{u}}{\partial t} + (\mathbf{u} \cdot \nabla)\mathbf{u} - \mathbf{G}\right) + \nabla \cdot \mathbf{P} - qn(\mathbf{E} + \mathbf{u} \times \mathbf{B}) = \frac{\delta M}{\delta t} \quad (5.4)$$

$$\frac{1}{\gamma - 1} \frac{\partial p}{\partial t} + \frac{1}{\gamma - 1} (\mathbf{u} \cdot \nabla)p + \frac{\gamma}{\gamma - 1} p(\nabla \cdot \mathbf{u}) + (\nabla \cdot \mathbf{h}) = \frac{\delta E}{\delta t} \quad (5.5)$$

Here, n is the number density, m is the mass, and \mathbf{u} is the average velocity of the fluid particle. The specific heat ratio γ is 5/3 assuming particles have no internal degrees of freedom. It is also assumed that collisions are dominant, the shearing stresses are negligible, and that the plasma is isotropic. In other words, the pressure tensor is defined as $\mathbf{P} = p\mathbf{I}$, where $p = \frac{1}{3}mn\langle c^2 \rangle$ and c is the random velocity, $\mathbf{c} = \mathbf{v} - \mathbf{u}$. Since the heat conductivity is not known well, the heat flux \mathbf{h} is ignored in the energy equation.

The last term in the Boltzmann equation represents the rate of change of the velocity distribution function due to both elastic and inelastic collisions. The transfer integrals for the elastic collision are listed in the first column of Table 5.1, where T is the temperature, ν_{st} is the non-resonant momentum transport collision frequency defined as $\nu_{st} = m_t [(m_s + m_t)\tau_{st}]^{-1}$, and τ_{st} is the velocity independent average collision time between the species s and t . These are obtained assuming that in steady-state equilibrium all species reach the same bulk velocity, and temperature and the total mass momentum and energy of the particles, s and t , are conserved.

For inelastic collisions, all particles are assumed to possess no internal degree of freedom, and energy thresholds for chemical reactions and ionization processes are assumed to be zero. The second column of Table 5.1 shows the transfer integrals for ions representing the source and loss terms due to ionization, charge exchange, and recombination. The production rate of ions is defined as S_s while the loss rate is L_s .

Table 5.1: Transfer integrals for elastic and inelastic collisions

	Elastic	Inelastic
$\frac{\delta n_s}{\delta t}$	0	$\frac{S_s - L_s}{m_s}$
$\frac{\delta M_s}{\delta t}$	$m_s n_s \sum_{t=\text{all}} \nu_{st}(\mathbf{u}_t - \mathbf{u}_s)$	$S_s(\mathbf{u}_{s0} - \mathbf{u}_s)$
$\frac{\delta E_s}{\delta t}$	$\sum_{t=\text{all}} \frac{m_s n_s \nu_{st}}{m_s + m_t} [3k(T_t - T_s) + m_t(\mathbf{u}_t - \mathbf{u}_s)^2]$	$\frac{k}{\gamma - 1} \frac{S_s T_{s0} - L_s T_s}{m_s} + \frac{1}{2} S_s(\mathbf{u}_{s0} - \mathbf{u}_s)^2$

as in Equations 5.6 and 5.7, respectively.

$$S_s = m_s n_{s'} (\nu_{\text{ph},s'} + \nu_{\text{ipm},s'} + \sum_{i=\text{ions}} k_{is'} n_i) \quad (5.6)$$

$$L_s = m_s n_s (\alpha_{r,s} n_e + \sum_{t'=\text{neutrals}} k_{st'} n_{t'}) \quad (5.7)$$

In these equations, s refers to an ion species while s' refers to neutral particle associated with the ion s . Moreover, $\nu_{\text{ph},s'}$ and $\nu_{\text{ipm},s'}$ are the photoionization and total impact ionization frequencies while $k_{is'}$ and $k_{st'}$ are charge exchange rates, and $\alpha_{r,s}$ is the recombination rate. Total transfer integrals of the collisions can be obtained by summing the integrals of the elastic and inelastic collisions.

Similar collision transfer integrals can be obtained and used in the transport equation for electrons. However, in the current model, simplified forms of the continuity and momentum equations 5.8 and 5.9 are utilized under the assumption of quasi-neutrality and massless electrons.

$$n_e = \sum_{i=\text{ions}} Z_i n_i \quad (5.8)$$

$$\nabla p_e + e n_e (\mathbf{E} + \mathbf{u}_e \times \mathbf{B}) = 0 \quad (5.9)$$

Using the above functions, ion transport equations are further simplified by assuming that all neutrals have the same temperature and bulk velocity, and all ion species have the same temperature and velocity. Under this assumption, only the

neutral-ion collision terms remain in the transfer equations as the net effect of the collisions between the ion species is zero and the effect of ion-massless electron collision is neglected. After defining the electric current density \mathbf{J} , total plasma pressure p , and total plasma density ρ as in Equations 5.10, 5.11, and 5.12

$$\mathbf{J} = \sum_{s=\text{ions}} eZ_s n_s \mathbf{u}_s - en_e \mathbf{u}_e \quad (5.10)$$

$$\rho = \rho_i + \rho_e \simeq \sum_{s=\text{ions}} \rho_s \quad (5.11)$$

$$p = p_i + p_e = \sum_{s=\text{ions}} p_s + p_e \quad (5.12)$$

the sum of continuity equations and the sum of momentum equations over all ion species yield Equations 5.13 and 5.14, respectively.

$$\frac{\partial \rho_s}{\partial t} + \nabla \cdot (\rho_s \mathbf{u}) = S_s - L_s \quad (5.13)$$

$$\begin{aligned} \rho \frac{\partial \mathbf{u}}{\partial t} + \rho(\mathbf{u} \cdot \nabla) \mathbf{u} + \nabla p - \mathbf{J} \times \mathbf{B} = \\ \rho G + \sum_{s=\text{ions}} \rho_s \sum_{t=\text{neutrals}} \nu_{st}(\mathbf{u}_n - \mathbf{u}) + \sum_{s=\text{ions}} S_s(\mathbf{u}_n - \mathbf{u}) \end{aligned} \quad (5.14)$$

The sum of electron and all ions energy equations yields Equation 5.15, assuming the velocity difference between the ions and electrons is small which is due to the presence of electric field between them.

$$\begin{aligned} \frac{1}{\gamma - 1} \frac{\partial p}{\partial t} + \frac{1}{\gamma - 1} (\mathbf{u} \cdot \nabla) p + \frac{\gamma}{\gamma - 1} p (\nabla \cdot \mathbf{u}) + \nabla \cdot \mathbf{h} = \\ \sum_{s=\text{ions}} \sum_{t=\text{neutrals}} \frac{\rho_s \nu_{st}}{m_s + m_t} [3k(T_n - T_i) + m_t(\mathbf{u}_n - \mathbf{u})^2] \\ + \frac{k}{\gamma - 1} \sum_{s=\text{ions}} \frac{S_s T_n - L_s T_i}{m_s} + \frac{1}{2} \sum_{s=\text{ions}} S_s(\mathbf{u}_n - \mathbf{u})^2 \\ + \frac{k}{\gamma - 1} [\sum_{s'} n_{s'} (\nu_{\text{ph},s'} + \nu_{\text{imp},s'}) T_n - \sum_{s=\text{ions}} n_s \alpha_{r,s} n_e T_e] \end{aligned} \quad (5.15)$$

where plasma velocity is:

$$\mathbf{u} = \frac{\rho_i \mathbf{u}_i + \rho_e \mathbf{u}_e}{\rho} \simeq \mathbf{u}_i \quad (5.16)$$

Maxwell's equations are included for the complete description of the MHD formulation: Assuming that conductivity is a constant (σ_0), taking the curl of the Ohm's law, and substituting the Faraday's and Ampere's law, the following induction equation is obtained. This equation governs the time evolution of the magnetic field in plasma.

$$\frac{\partial \mathbf{B}}{\partial t} = \nabla \times (\mathbf{u} \times \mathbf{B}) - \frac{1}{\sigma_0 \mu_0} \nabla \times (\nabla \times \mathbf{B}) \quad (5.17)$$

Moreover, the current density \mathbf{J} in the momentum transport equation (5.14) can be replaced by $\mathbf{J} = (\mu_0^{-1}) \nabla \times \mathbf{B}$, which can be obtained from Ampere's law by ignoring the displacement current.

Equations 5.13, 5.14, 5.15, and 5.17 constitute the self-consistent MHD equation set that is need to be solved to simulate the Martian solar wind interaction. (For detailed description see [Ma *et al.*, 2004]) The numerical solution of these equations is obtained by modifying BATS-R-US (Block Adaptive-Tree Solar-wind Roe-type Upwind Scheme) code which was first developed to simulate Earth's solar wind and then has been extended to model various comets, moon, and planets' solar wind interaction including Mars [Ma *et al.*, 2004] (Details of this approach and code can be found in [Hansen, 2001] and [Powell *et al.*, 1999]). In order to resolve the Martian ionosphere better, spherical grid structure is applied in the solution.

5.3 Results

Extensive computer resources necessary to run the model limit the number of cases that can be simulated. Therefore, in this section, we present the simulation results

obtained only for a special case for which the enhancement events are observed and compare the results to the MGS observations. The compact form of normalized set of equations solved in these runs is:

$$\frac{\partial \mathbf{W}}{\partial t} + (\nabla \cdot \mathbf{F})^T = \mathbf{Q} \quad (5.18)$$

where the state vector, flux tensor, and source term are defined as in the following equations (Equations 5.19, 5.20, 5.21), respectively. In these equations, the source terms are further simplified by assuming that ions and electrons have the same velocity, \mathbf{u} , and the velocity of the neutrals is zero, considering their small relative speed with respect to other species in the ionosphere.

$$\mathbf{W} = [\rho_i, \rho \mathbf{u}, \mathbf{B}, \varepsilon]^T \quad (5.19)$$

$$\mathbf{F} = [\rho_i \mathbf{u}, \rho \mathbf{u} \mathbf{u} + (p + \frac{B^2}{2}) \mathbf{I} - \mathbf{B} \mathbf{B}, \mathbf{u} \mathbf{B} - \mathbf{B} \mathbf{u}, \mathbf{u}(\varepsilon + p + \frac{B^2}{2}) - (\mathbf{B} \cdot \mathbf{u}) \mathbf{B}]^T \quad (5.20)$$

$$\mathbf{Q} = [S_i - L_i, \rho \mathbf{G} - \rho \nu \mathbf{u} - \mathbf{u}(L_1 + L_2 + L_3 + L_4), 0, \mathbf{Q}_e]^T \quad (5.21)$$

where the total energy density and energy source are

$$\varepsilon = \frac{1}{2}(\rho_1 + \rho_2 + \rho_3 + \rho_4)u^2 + \frac{1}{\gamma - 1}p + \frac{B^2}{2} \quad (5.22)$$

$$\begin{aligned} \mathbf{Q}_e = & \rho \mathbf{u} \cdot \mathbf{G} - \frac{1}{2}u^2(L_1 + L_2 + L_3 + L_4) - \rho u^2 \nu \\ & + \frac{kT_0}{\gamma - 1} \left(\sum_{i=1}^4 \frac{S_i}{m_i} \right) - \frac{p}{\gamma - 1} \left(\sum_{i=1}^4 \frac{L_i}{m_i} \right) / \left(\sum_{i=1}^4 \frac{\rho_i}{m_i} \right) \\ & - 4 \times 10^{-11} \sum_{t=1}^3 n_t \sum_{i=1}^4 \frac{\rho_i}{m_i} \exp[10(T_p - 6000)/T_p] \end{aligned} \quad (5.23)$$

Four major ion species present in the Martian environment are represented in the model. $\rho_1, \rho_2, \rho_3, \rho_4$ are the mass densities of H^+ , O_2^+ , O^+ , and CO_2^+ , respectively, where H^+ represents the solar wind, and the rest represents the Martian ionosphere.

S_1, S_2, S_3, S_4 and L_1, L_2, L_3, L_4 are the H^+ , O_2^+ , O^+ , CO_2^+ mass source and loss rates, respectively. These rates are calculated using the chemical reactions listed in Table 5.2. Ion neutral collision frequency, ν , is chosen to be 4×10^{-10} ($[O]$, $[CO_2]$, $[H]$ s^{-1}) and plasma conductivity, σ_0 is assumed to be infinity. The optical depth effect is approximated by including a cosine factor for the different solar zenith angles and by assuming average absorption coefficients of 2.6×10^{17} and 1.5×10^{17} cm^2 for CO_2 and O , respectively [Schunk and Nagy, 2000]. On the nightside, the solar flux is assumed to be 1.0×10^{-5} times the unattenuated solar radiation.

T_p is the plasma temperature and T_0 is the temperature of the newly generated ions, which is assumed to be equal to the local neutral atmosphere temperature. The last term in Equation 5.23, is added to keep the temperature close to the observed values in the ionosphere. n_i is the number density of neutral species corresponding the CO_2 , O and H , respectively. The neutral densities used in the calculations are based on the Viking neutral mass spectrometer and the retarding potential analyzer (RPA) data, and Mariner 6–7 observations (for details see [Ma et al., 2004] and references therein). The 90-degree harmonic expansion for the crustal magnetic fields, developed by Cain et al. [2003], is used to describe the Martian magnetic field.

The inner boundary is set at ~ 100 km altitude at which the O_2^+ , O^+ , and CO_2^+ densities are taken to be the photochemical equilibrium value. A reflective boundary is used for the flow which results in almost zero velocities near the inner boundary, as actually observed. The plasma temperature, which is sum of the electron and ion temperatures in this model, at the inner boundary is assumed to be two times the corresponding neutral temperature, and the pressure is set accordingly ($p = nkT$).

The results are presented in MSO coordinate system. Computational domain covers a space around Mars between the spherical surfaces at 100 km altitude and $1.7R_M$ altitude ($R_M=3396$ km, radius of Mars). Due to spherical grid structure, resolution changes from ~ 30 km at the lower boundary near the poles to ~ 900 km

Table 5.2: List of chemical reactions and rates considered in the model [Ma et al., 2004]

Chemical Reaction	Rate Coefficient	Reference
$\text{CO}_2 + h\nu \longrightarrow \text{CO}_2^+ + e$	$4.89 \times 10^{-7} \text{ s}^{-1}$	<i>Schunk and Nagy</i> [2000]
$\text{O} + h\nu \longrightarrow \text{O}^+ + e$	$1.81 \times 10^{-7} \text{ s}^{-1}$	<i>Schunk and Nagy</i> [2000]
$\text{H} + h\nu \longrightarrow \text{H}^+ + e$	$7.09 \times 10^{-8} \text{ s}^{-1}$	<i>J. Fox</i> [2004]
$\text{CO}_2^+ + \text{O} \longrightarrow \text{O}_2^+ + \text{CO}$	$1.64 \times 10^{-10} \text{ cm}^{-3} \text{ s}^{-1}$	<i>Schunk and Nagy</i> [2000]
$\text{CO}_2^+ + \text{O} \longrightarrow \text{O}^+ + \text{CO}_2$	$9.60 \times 10^{-10} \text{ cm}^{-3} \text{ s}^{-1}$	<i>Schunk and Nagy</i> [2000]
$\text{O}^+ + \text{CO}_2 \longrightarrow \text{O}_2^+ + \text{CO}$	$1.10 \times 10^{-9} (800/T_i)^{0.39} \text{ cm}^{-3} \text{ s}^{-1}$	<i>Fox and Sung</i> [2001]
$\text{O}^+ + \text{H} \longrightarrow \text{H}^+ + \text{O}$	$6.40 \times 10^{-10} \text{ cm}^{-3} \text{ s}^{-1}$	<i>Schunk and Nagy</i> [2000]
$\text{H}^+ + \text{O} \longrightarrow \text{O}^+ + \text{H}$	$5.08 \times 10^{-10} \text{ cm}^{-3} \text{ s}^{-1}$	<i>Fox and Sung</i> [2001]
$\text{O}_2^+ + e \longrightarrow \text{O} + \text{O}$	$7.38 \times 10^{-8} (1200/T_e)^{0.56} \text{ cm}^{-3} \text{ s}^{-1}$	<i>Schunk and Nagy</i> [2000]
$\text{CO}_2^+ + e \longrightarrow \text{CO} + \text{O}$	$3.10 \times 10^{-7} (300/T_e)^{0.5} \text{ cm}^{-3} \text{ s}^{-1}$	<i>Fox and Sung</i> [2001]

at the outer boundary.

As mentioned previously, the model is run for a special case, where the planet's rotation axis is tilted 25° toward the Sun, and the subsolar longitude is 230° E. This orientation of Mars and the crustal fields corresponds a geometry under which occurrence of the enchantments is the most probable. Moreover, for this case, the IMF is assumed to be in the $-y$ direction with a magnitude of 3 nT, and the solar wind velocity and density are selected to be 400 km-s^{-1} and 4 cm^{-3} , respectively. The upstream solar wind ion and electron temperatures are set to be 5×10^4 and 3×10^5 K. The solar wind parameters are set to these values in order to closely approximate the enhancement observation conditions. After the calculations were carried out by *Yingjuan Ma* for the specified conditions, the plasma densities, magnetic field, plasma bulk velocity, and solar wind thermal pressure were provided. First, the general features of the Martian solar wind interaction such as the location of the plasma boundaries, magnetic field draping, total field pressure and plasma distribution around Mars are examined.

The color in Figure 5.1a and 5.1b shows the calculated magnetic field strength

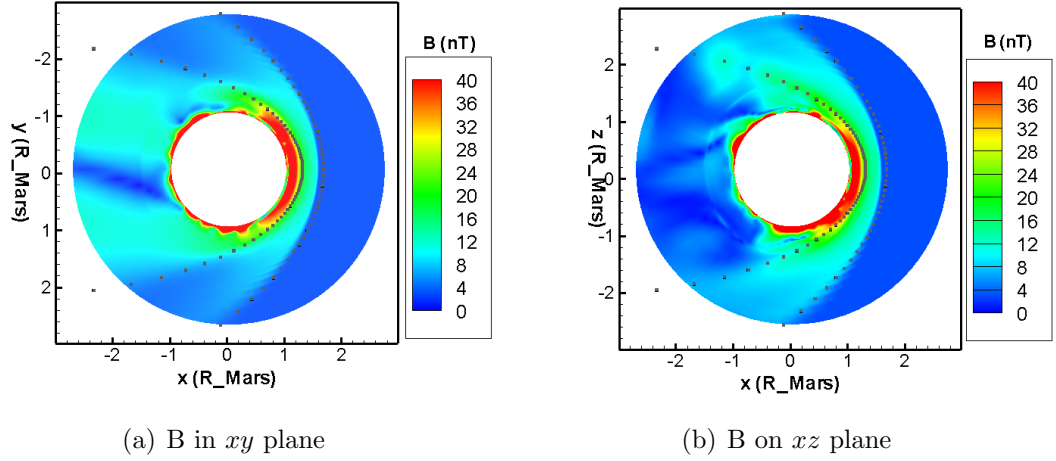


Figure 5.1: Strength of the calculated magnetic field on the equatorial (xy plane) and on the noon-midnight (xz plane) planes.

in the equatorial plane (xy plane in MSO) and in the noon-midnight meridional plane (xz plane in MSO), respectively. The black dotted lines indicate the bow shock and the MPB boundary locations, estimated by *Vignes et al.* [2000] using the MGS observations. As seen in the figures, these curves match well with the plasma boundaries obtained from the simulations. Strength of the magnetic field increases from 3 nT to 8–9 nT at the bow shock and further increases at the MPB exceeding 40 nT at this boundary. This trend is typically what is observed at Mars and similar to what is obtained from our analytical model in Chapter 4, but overestimating the field strength at the MPB (see Figure 4.9). Moreover, the general features of the Martian plasma environment such as the draping of the IMF, the presence of minimagnetospheres and induced magnetic field in the ionosphere are evident in the results.

Similarly, Figure 5.2a and 5.2b show plasma velocity strength in the equatorial plane (xy plane in MSO) and in the noon-midnight meridional plane (xz plane in

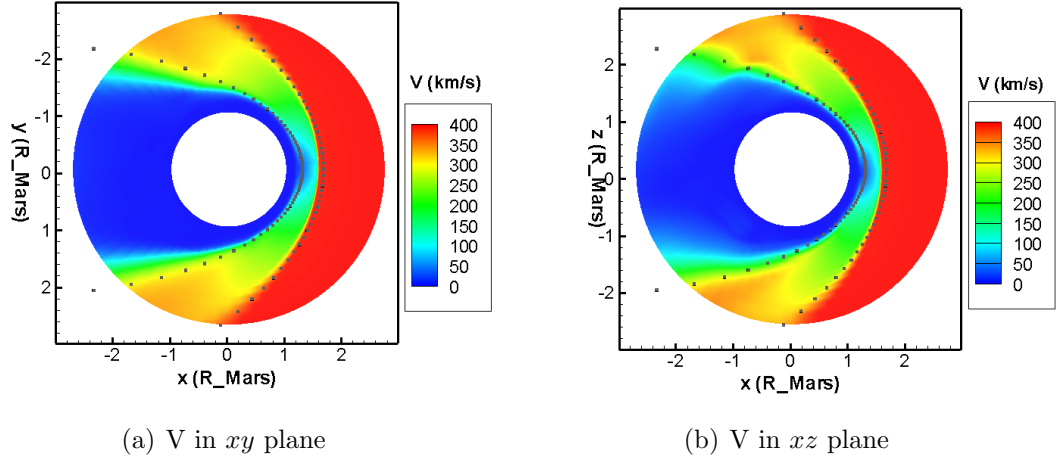


Figure 5.2: Strength of the calculated velocity field on the equatorial (xy plane) and on the noon-midnight (xz plane) planes.

MSO), respectively. As seen in these figures, flow speed drops to one-fourth of its upstream value at the bow shock near the subsolar point and further decreases to one tenth of its speed in the solar wind at the MPB. These values are consistent with the results from our analytical model presented in Chapter 4, which mainly based on the satellite observations. Therefore, the global structure of the calculated interaction from the current model is in general agreement with the previous results and satellite observations. Figure 5.3 shows the calculated ion and electron densities for the subsolar 0° N, 45° N, 45° S, and 70° N. In these profiles, the dependency of the ion distribution with respect to SZA is evident. Comparison of these results to the calculated profiles presented in [Ma *et al.*, 2004] shows good agreement. In their study, Ma *et al.* [2004] compare these profiles with the observations and show that they exhibit good agreement above 140 km while exhibiting disagreement at low altitudes. The main reason for this disagreement is explained as the optical depth approximations used in the model (cosine factor at high zenith angles). The magnetic

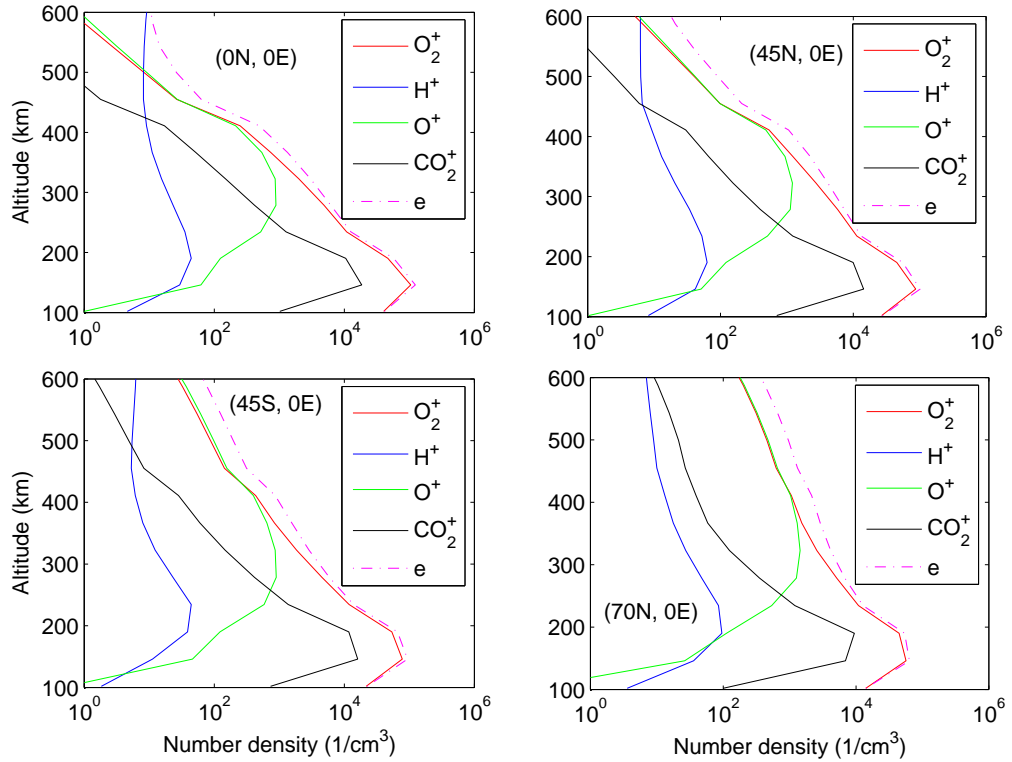


Figure 5.3: The calculated ion and electron density profiles from the model results for the subsolar 0° N, 45° N, 45° S, and 70° N.

field configuration over the proposed crustal sources are investigated in this section in order to check the validity of the conclusions derived from the semi-empirical-analytical model in the previous chapter (Chapter 4). Figure 5.4 shows the geometry of MGS orbit, orientation of Mars, relative position of the crustal sources for the case the model is run, and the resulting magnetic field lines over the proposed crustal sources obtained from the model. The black solid line shows the Mars' rotation axis which is tilted by 25° toward the Sun (northern hemisphere is in summer). The purple circle indicates the orbit of MGS at 400 km altitude, and the region marked on the orbit shows the enhancement observation site. The color map is the radial component of the crustal magnetic fields calculated from the model on a spherical surface at 300 km altitude. The thin black lines drawn close to Mars illustrate the

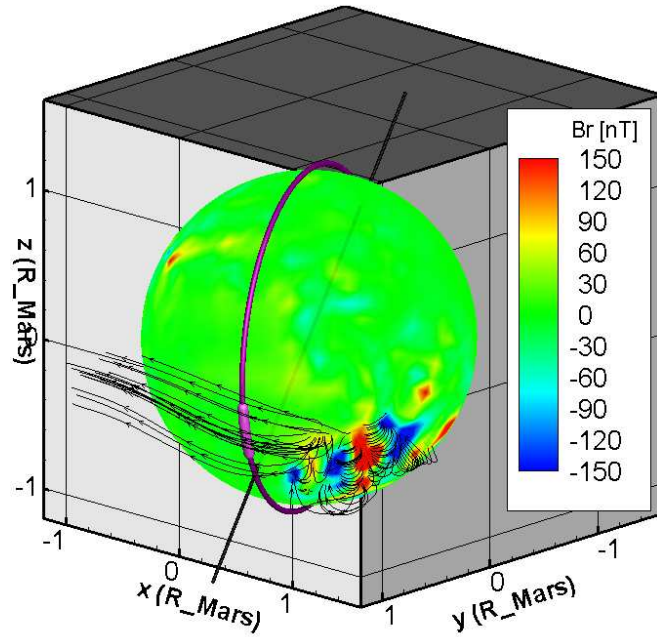


Figure 5.4: The magnetic field lines in black are drawn over the proposed crustal sources including the geometry of MGS orbit, orientation of Mars and relative position of the crustal sources for the case the model is run. The black solid line shows the Mars rotation axis which is tilted by 25° toward the Sun. The purple circle indicates the orbit of MGS, and the region marked on the orbit shows the enhancement observation site. The color map is the radial component of the crustal magnetic fields calculated from the model and plotted over a spherical surface at 300 km altitude.

magnetic field lines obtained from the current model results over the source region. As it is evident in this figure, reconnection with the draping IMF occurs over these magnetic sources, and the reconnected field lines stretch toward the tail due to the solar wind plasma flow around the planet. Since these local crustal fields are proposed to be the origin of the photoelectrons, the low-energy electrons may follow these lines to the nightside of Mars. This result is consistent with our interpretation of the phenomena. The physical conditions that the MHD model was run are exactly same as the conditions that the previous model is developed. (Mars's rotation axis is tilted by 25° and the subsolar longitude is 230° E. The solar wind parameters are same for

both models). Therefore, the results from these two models can reliably be compared for consistency. The similarity of the field line topologies in Figures 5.4 and 4.12a is evident, confirming the conclusions derived from our simple analytical model.

5.4 Summary

MHD models are in general adequate to simulate and investigate the global interaction of the planets with the solar wind. This work is the first effort to reproduce a local transient event, the electron flux enhancement on the nightside of Mars, using an MHD simulation. The current four-ion single fluid MHD model, developed by *Ma et al.* [2004], numerically solves a number of continuity equations for each ion species, one energy equation, one momentum equation, and Maxwell's equations to describe the Martian solar wind interaction. The model is run for a special case, where the planet's rotation axis is tilted 25° toward the Sun, and the subsolar longitude is 230° E. This orientation of Mars and the crustal fields corresponds a geometry under which occurrence of the enhancements is the most probable. Moreover, for this case, the solar wind parameters are set to values which closely approximate the enhancement observation conditions. The calculations were carried out by Yingjuan Ma for the specified conditions, and the provided results show good agreement with the global observations of the Martian solar wind interaction as well as the crustal field affects in the interaction. Moreover, investigation of the field line configuration showed that reconnection occurs between the proposed crustal sources and the draping IMF for the physical conditions of the observed enhancements. This result is consistent with our physical interpretation of the events and conclusions derived from the semi-empirical-analytical model in the previous chapter.

Chapter 6

Conclusion

6.1 Summary of the Contributions

In this dissertation, we have reported a novel transient phenomenon observed in the Mars Global Surveyor electron omni-directional flux data over a specific geographical region (at around 70° S and between 30° E and 150° E) on the nightside of Mars. As MGS passes over this region from north to south on the nightside, the low-energy omnidirectional electron fluxes below a few hundred eV exhibit sharp enhancements, an increase of approximately two orders of magnitude over the ambient flux levels. This particle enhancement event is one of the local events observed at Mars likely induced by the strong crustal magnetic sources on the surface during the planet's interaction with the solar wind.

The statistical and spectral analyses of the electron flux enhancements have revealed three critical features of the events: (i) The enhancements are periodic both on a Martian year and a ~ 25 day time scale. (ii) The enhancement spectra are distinct in nature among the spectra of previously observed transient events on the nightside of Mars, such as auroras, strip-like plasma structure along the wake boundary or plasma spikes. (iii) The events have common signatures in the magnetic field distribution at

time of these events, implying a significant current in the azimuthal direction. The x component of the magnetic field in the MSO system changes from -20 nT to 20 nT, y component has an approximately -7 nT offset, and z component remains below 5 nT during the events. The x components have sign reversals which coincide with the center points of the enhancements along the orbit and constitute the major component of the induced current due to these events. This significant current in the azimuthal direction is also confirmed by modeling the current sources responsible for the observed magnetic field perturbations.

The low-energy electron enhancement phenomena have been interpreted as the transportation of photoelectrons above the crustal magnetic sources on the dayside to the magnetotail on the nightside of Mars along the lines of reconnected Interplanetary Magnetic Field (IMF). The draping direction of the IMF at the time of the enhancements are estimated using the dayside magnetic field data over the northern hemisphere where crustal fields are absent. The estimation results have showed that at the time of the events the draped IMF is mostly oriented westward and its strength ranges from 20 and 60 nT. The crustal sources located at 65° S, 150° E have been proposed to be the origin of the low-energy electrons seen in the enhancements. This source location is closest to the enhancements and most active in terms of auroral events. Moreover, the sources in this location are oriented eastward and their magnitude is approximately 50 nT at 400 km altitude. The opposite alignment of the draped IMF with respect to these magnetic sources and similarity of the field strengths confirms the existence of favorable conditions for their reconnection at the time of the events. The seasonal nature of the events is explained by the seasonal variation of the draped IMF direction. The short-term periodicity, on a ~ 25 day scale, seen in both the draped IMF direction and the occurrence times of the enhancements implies the role of the IMF and its orientation. SZA values below 110° over the proposed crustal sources at the time of the events showed that these sources

are illuminated by the Sun during the enhancements, which is a requirement of our interpretation of the phenomena.

In order to explore the origin of this phenomenon, a semi-empirical-analytical model is developed, describing the magnetic field configuration of the solar wind interaction with Mars. In this model, crustal fields are represented by spherical harmonic expansion, and the perturbed solar wind field is derived from the deviation of a proton flow around Mars assuming that Mars is absent of either global or local crustal magnetic fields. Overall magnetic field is obtained from the vector superposition of the crustal fields and perturbed solar wind field. Results from the model showed that, under the conditions observed at the time of the events, reconnection of the crustal magnetic fields with the draping IMF is feasible over the proposed sources at around 150° E and 65° S. This result is consistent with our interpretation but not sufficient to conclude that our explanation of the phenomenon is the only and actual mechanism responsible for the events. Therefore, physically more realistic modeling, such as MHD or hybrid modeling, is needed and attempted.

Finally, simulations from a four-ion single-fluid MHD model, developed by *Ma et al.* [2004], of a self-consistent description of the Martian solar wind interaction including the effect of the crustal magnetic sources, have been investigated and compared with the previous conclusions from the semi-empirical-analytical model. The simulation results of this MHD model presented in this dissertation are obtained from the calculations carried out by Yingjuan Ma for a special case, which corresponds to the solar wind conditions and Mars orientations under which the enhancements are observed. The four-ion single fluid MHD description of the Martian solar wind interaction is in general good agreement with the global magnetic and plasma observations around Mars. Comparison of the field line configurations from this MHD model and the analytical model over the proposed crustal sources showed that reconnection between these crustal fields with the draping IMF occur for the physical

conditions that the enhancements are observed in both models, which is consistent with our interpretation of the phenomena.

6.2 Suggestions for Future Research

In this dissertation, a physical explanation for the observed electron enhancement events is sought with the analysis of all available electron flux and magnetic field data from MGS. More accurate description of the phenomena is possible by the collective analysis of similar observations from all other sources. Additionally, analysis of the pitch angle distribution of electrons along with the magnetic field data during the events may significantly contribute to our current understanding of the phenomena. The direction of the electron motion about the local magnetic field can be derived from the pitch angle distribution and may help confirming the validity of our interpretation of the events. Naturally, other charged particle distributions, such as the planetary ions and the solar wind protons, recorded in the vicinity of the enhancement observation site may also help to fully understand the mechanism behind the events. The search for the correlation between the intensity of the electron flux enhancements and solar wind parameters may provide more information about the characteristics of the events and provide better insight of the source of the phenomena. For this research, the solar wind parameters measured at Earth can accordingly be expanded to the orbit of Mars and be utilized in such a correlation analysis.

The semi-empirical-analytical model developed for the magnetic field configuration of the Martian solar wind interaction can be improved in several ways in order to obtain a more realistic flow description around Mars. First of all, asymmetric nature of a realistic proton flow can be represented by modifying the analytical expression of the flow velocity. Resulting asymmetry in the plasma boundaries can also be represented by defining more boundaries. In this model, it is assumed that the Hall

effect is negligible and thus the magnetic field is frozen into the proton flow. However, by including the Hall effect, the magnetic field can be assumed to be frozen into the electron flow. Moreover, same condition for the magnetic field and electron flow can also be achieved by defining separate velocity fields for all major charged particles, as the electron velocity is connected to all other heavy ions. The consequence of this modification would be a change in the velocity distribution and probably an increase in the velocity in the tail which also influence the magnetic draping configuration in the tail. It is known that the variation in the solar wind conditions may significantly influence the interaction. The effect of each solar wind parameter can be included in the analytical definition of the velocity field. All these modifications in the model require more empirical information and data analysis.

The semi-empirical-analytical model developed and the MHD model analyzed in this dissertation successfully reproduce the general features of the Martian solar wind interaction and the results are in general consistent with the observations. Moreover, these two global interaction models predict the reconnection of the crustal fields with the draping IMF under the physical conditions that the enhancements are observed. However, all model analyses included in this dissertation are conducted under the nominal solar wind conditions. Systematic investigation of the effects of each solar wind parameter on the Martian solar wind interaction should also be undertaken which may reveal critical information about the source of the enhancement events. Further exploration of the governing physical processes during the observed events utilizing empirical data along with theoretical and numerical study is essential to the long term goal of achieving an accurate understanding of the solar wind interaction with Mars.

Appendix A

Spherical Harmonic Expansion of Global Magnetic Fields

A magnetic field configuration can be expressed by a concise formula with adjustable parameters assuming steady-state and current free conditions. Maxwell's equations for magnetic fields are

$$\nabla \cdot \mathbf{B} = 0 \quad (\text{A.1})$$

$$\nabla \times \mathbf{B} = \mu_0 \epsilon_0 \frac{\partial \mathbf{E}}{\partial t} + \mu_0 \mathbf{i} \quad (\text{A.2})$$

If it is assumed that the system is in steady-state ($\partial/\partial t = 0$) and there is no current source ($\mathbf{i} = 0$) in the region of interest, Equation A.2 becomes

$$\nabla \times \mathbf{B} = 0 \quad (\text{A.3})$$

If the curl of a magnetic field is zero, that magnetic field can be expressed as the gradient of a scalar potential function, V .

$$\mathbf{B} = -\nabla V \quad (\text{A.4})$$

Using Equation A.1, Laplace's equation is obtained as follows.

$$\nabla \cdot \mathbf{B} = -\nabla^2 V = 0 \quad (\text{A.5})$$

Solution of this equation (Equation A.5) in spherical coordinates can be obtained using separation of variables.

$$V(r, \theta, \phi) = R \sum_{n=1}^N \sum_{m=0}^n \left(\frac{R}{r} \right)^{n+1} [g_n^m \cos(m\phi) + h_n^m \sin(m\phi)] P_n^m(\cos \theta) \quad (\text{A.6})$$

where r is the radius, θ is the colatitude, and ϕ is the east longitude in the spherical coordinate system. R is the radius of a reference spherical surface. n and m are separation constants which must be integers in this representation. The sum over n extends to infinity for the complete description of the magnetic field, but for practical reasons it extends to a finite value which also determined the highest degree (N) and the resolution of the expansion. $n = 0$ term is excluded in the sum, as there is no monopole for the magnetic field. P_n^m is the Schmidt normalized associated Legendre function with degree n and order m . g_n^m and h_n^m are called the spherical harmonic coefficients. From $\mathbf{B} = -\nabla V$, each spherical component of the magnetic field can be

expressed as follows:

$$B_r = -\frac{\partial V}{\partial r} \quad (\text{A.7})$$

$$= \sum_{n=1}^N \sum_{m=0}^n (n+1) \left(\frac{R}{r}\right)^{n+2} [g_n^m \cos(m\phi) + h_n^m \sin(m\phi)] P_n^m(\cos \theta) \quad (\text{A.8})$$

$$B_\theta = -\frac{1}{r} \frac{\partial V}{\partial \theta} \quad (\text{A.9})$$

$$= -\sum_{n=1}^N \sum_{m=0}^n \left(\frac{R}{r}\right)^{n+2} [g_n^m \cos(m\phi) + h_n^m \sin(m\phi)] \frac{\partial P_n^m(\cos \theta)}{\partial \theta} \quad (\text{A.10})$$

$$B_\phi = -\frac{1}{r \sin \theta} \frac{\partial V}{\partial \phi} \quad (\text{A.11})$$

$$= -\sum_{n=1}^N \sum_{m=0}^n \left(\frac{m}{\sin \theta}\right) \left(\frac{R}{r}\right)^{n+2} [-g_n^m \sin(m\phi) + h_n^m \cos(m\phi)] P_n^m(\cos \theta) \quad (\text{A.12})$$

In this equation, P_n^m can be calculated from

$$P_n^m(\cos \theta) = (-1)^m (\sin \theta)^m \frac{d^m}{d(\cos \theta)^m} P_n(\cos \theta) \quad (\text{A.13})$$

where

$$P_n(\cos \theta) = \frac{1}{2^n n!} \frac{d^n}{dx^n} [(\cos \theta)^2 - 1]^n \quad (\text{A.14})$$

Bibliography

- [1] Acuña, M. H., et al. (1992), Mars Observer magnetic fields investigation, *J. Geophys. Res.*, *97*(E5), 7799-7814.
- [2] Acuña, M. H., et al. (1998), Magnetic field and plasma observations at Mars: Initial results of Mars Global Surveyor mission, *Science*, *279*, 1676-1680.
- [3] Acuña, M. H., et al. (1999), Global distribution of crustal magnetization discovered by the Mars Global Surveyor MAG/ER experiment, *Science*, *284*, 790-793.
- [4] Acuña, M. H., et al. (2001), Magnetic field of Mars: Summary of results from the aerobraking and mapping orbits, *J. Geophys. Res.*, *106*(E10), 23,403-23,417.
- [5] Albee, A. L., R.E. Arvidson, F. Palluconi, and T. Thorpe (2001), Overview of the Mars Global Surveyor mission, *J. Geophys. Res.*, *106*(E10), 23,291.
- [6] Bertaux, J. L., F. Leblanc, O. Witasse, E. Quemerais, J. Lilensten, A. S. Stern, B. Sandel, and O. Korablev (2005), Discovery of aurora on Mars, *Nature*, *435*, 790-794.
- [7] Birn, J., et al. (2001), Geospace environmental modeling (GEM) magnetic reconnection challenge, *J. Geophys. Res.*, *106*, 3715- 3719.
- [8] Biskamp, D. (2000), Magnetic Reconnection in Plasmas, *Cambridge University Press*.

- [9] Brace, L., R. Theis, H. Mayr, S. Curtis, and J. Luhmann (1982), Holes in the Nightside Ionosphere of Venus, *J. Geophys. Res.*, *87*(A1), 199-211.
- [10] Brain, D. A., F. Bagenal, M. H. Acuña, and J. E. P. Connerney (2003), Martian magnetic morphology: Contributions from the solar wind and crust, *J. Geophys. Res.*, *108*(A12), 1424.
- [11] Brain, D. A., J. S. Halekas, L. M. Peticolas, R. P. Lin, J. G. Luhmann, D.L. Mitchell, G. T. Delory, S. W. Bougher, M. H. Acuña, and H. Rème (2006), On the origin of aurorae on Mars, *Geophys. Res. Lett.*, *33*(1), L01201.
- [12] Brain, D. A., D. L. Mitchell, and J. S. Halekas (2006), The magnetic field draping direction at Mars from April 1999 through August 2004, *Icarus*, *182*(2), 464-473.
- [13] Brecht, S. H. (1997), Hybrid Simulations of the Magnetic Topology of Mars, *J. Geophys. Res.*, *102*, 4743.
- [14] Cain, J. C., B. R. Ferguson, D. Mozzoni (2003), An n=90 internal potential function of the Martian crustal magnetic field, *J. Geophys. Res.*, *108*(E2), 5008.
- [15] Chen, R. H., T. E. Cravens, and A. F. Nagy (1978), The Martian ionosphere in light of the Viking observations, *J. Geophys. Res.*, *83*, 3871.
- [16] Cloutier, P. A., et al.(1999), Venus-like interaction of the solar wind with Mars, *Geophys. Res. Lett.*, *26*, 2685.
- [17] Connerney, J. E. P., M. H. Acuña, P. J. Wasilewski, N. F. Ness, H. Rème, C. Mazelle, D. Vignes, R. P. Lin, D. L. Mitchell, and P. Cloutier (1999), Magnetic lineations in the ancient crust of Mars, *Science*, *284*, 794-798.
- [18] Connerney, J. E. P., M. H. Acuña, P. J. Wasilewski, G. Kletetschka, N. F. Ness, H. Rème, R. P. Lin, and D. L. Mitchell (2001), The global magnetic field of Mars and implications for crustal evolution, *Geophys. Res. Lett.*, *28*(21), 4015-4018.

- [19] Crider, D. H., D. Vignes, A. M. Krymskii, T. K. Breus, N. F. Ness, D. L. Mitchell, J. A. Slavin, and M. H. Acuña (2003), A Proxy for Determining Solar Wind Dynamic Pressure at Mars using Mars Global Surveyor Data, *J. Geophys. Res.*, *108*(A12), 1461.
- [20] Crider, D. H. (2004), The influence of crustal magnetism on the solar wind interaction with Mars: recent observations, *Adv. Space Res.*, *33*, 152-160.
- [21] Crider, D. H., M. H. Acuña, J. E. P. Connerney, D. Vignes, N. F. Ness, A. M. Krymskii et al. (2002), Observations of the latitude dependence of the location of the martian magnetic pileup boundary, *Geophys. Res. Lett.*, *29*, 11.
- [22] Crider, D., M. H. Acuña, J. E. P. Connerney et al. (2001), Magnetic field draping around Mars: Mars global surveyor results, *Adv. Space Res.*, *27*, 1831-1836.
- [23] Crider, D. et al. (2000), Evidence of electron impact ionization in the magnetic pileup boundary at Mars, *Geophys. Res. Lett.*, *27*(1), 45.
- [24] Dolginov, S., Y. Yeroshenko, and L. Zhuzgov (1976), The Magnetic Field of Mars According to the Data From the Mars 3 and Mars 5, *J. Geophys. Res.*, *81*(19), 3353-3362.
- [25] Dolginov, S. (1986), Comments on "The Magnetic Field of Mars: Implications from Gas Dynamic Modeling" by C. T. Russell, J. C. Luhmann, J. R. Spreiter, and S. S. Stahara, *J. Geophys. Res.*, *91*(A11), 12143-12148.
- [26] Drake, J. F., M. A. Shay, W. Thongthai, and M. Swisdak (2005), Production of Energetic Electrons during Magnetic Reconnection, *Phys. Rev. Lett.*, *94*, 095001.
- [27] Drake, J. F., M. Swisdak, H. Che, and M. A. Shay (2006), Electron acceleration from contracting magnetic islands during reconnection, *Nature*, *443*, 553-556.

- [28] Dubinin, E., et al. (2006a), Solar wind plasma protrusion into the martian magnetosphere: ASPERA-3 observations, *Icarus*, 182, 343-349.
- [29] Dubinin, E., et al. (2006b), Plasma morphology at Mars. ASPERA-3 observations, *Space Sci. Rev.*, 126, 209-238.
- [30] Dubinin, E., et al. (2006c), Electric fields within the martian magnetosphere and ion extraction: ASPERA-3 observations, *Icarus*, 182, 337-342.
- [31] Dungey, J.W. (1961), Interplanetary Magnetic Field and the Auroral Zones, *Phys. Rev. Lett.*, 6, 47-48.
- [32] Fedorov, A., et al. (2006), Structure of the Martina wake, *Icarus*, 182, 329-336.
- [33] Ferguson, B. B., J. C. Cain, D. H. Crider, D. A. Brain, and E. M. Harnett (2005), External fields on the nightside of Mars at Mars Global Surveyor mapping altitudes, *Geophys. Res. Lett.*, 32, L16105.
- [34] Fjeldbo, W.C., G. Fjeldbo, and V. R. Eshleman (1996), Models of the atmosphere of Mars based on the Mariner-4 occultation experiment, *J. Geophys. Res.*, 71, 2307.
- [35] Fox, J. L. (1993), The production and escape of nitrogen atoms on Mars, *J. Geophys. Res.*, 98, 3297.
- [36] Frahm, R. A., et al. (2006a), Carbon dioxide photoelectron energy peaks at Mars, *Icarus*, 182, 371-382.
- [37] Frahm, R. A., et al. (2006b), Locations of atmospheric photoelectron energy peaks within the Mars environment, *Space Sci. Rev.*, 126, 389-402.
- [38] Giovanelli, R. G. (1946), A theory of chromospheric flares, *Nature*, 158:81-82.

- [39] Gosling, J. T., R. Skoug, D. J. McComas, and C. W. Smith (2005), Direct evidence for magnetic reconnection in the solar wind near 1 AU, *J. Geophys. Res.*, *110*, A01107.
- [40] Halekas, J. S., D. A. Brain, R. J. Lillis, M. O. Fillingim, D. L. Mitchell, and R. P. Lin (2006), Current sheets at low altitudes in the Martian magnetotail, *Geophys. Res. Lett.*, *33*, L13101.
- [41] Hanson, W. B., S. Sanatini, and D. R. Zuccaro (1977), The Martian ionosphere as observed by the Viking retarding potential analyzer, *J. Geophys. Res.*, *82*, 4351.
- [42] Harnett, E. M. and R. M. Winglee (2003), The Influence of a Mini-magnetopause on the Magnetic Pileup Boundary of Mars, *Geophys. Res. Lett.*, *30*20, 2074.
- [43] Harnett, E. M., and R. M. Winglee (2005), Three-dimensional fluid simulations of plasma asymmetries in the Martian magnetotail caused by the magnetic anomalies, *J. Geophys. Res.*, *110*, A07226.
- [44] Harnett, E. M., and R. M. Winglee (2006), Three-dimensional multifluid simulations of ionospheric loss at Mars from nominal solar wind conditions to magnetic cloud events, *J. Geophys. Res.*, *111*, A09213.
- [45] Hesse, M., M. Kuznetsova, and J. Birn (2004), The role of electron heat flux in guidefield magnetic reconnection, *Phys. Plasmas*, *11*, 5387-5397.
- [46] Kallio, E., H. Koskinen, S. Barabash, R. Lundin, O. Norberg and J. G. Luhmann (1993), 3D plasma observations near Mars, *Geophys. Res. Lett.*, *20*, 2339.
- [47] Kallio, E., H. Koskinen, S. Barabash, R. Lundin, O. Norberg and J. G. Luhmann (1994), Proton Flow in the Martian Magnetosheath, *J. Geophys. Res.*, *99*, 23547.

- [48] Kallio, E. (1996), An Empirical Model of the Solar Wind Flow Around Mars, *J. Geophys. Res.*, *101*, 11133.
- [49] Kilore, A.J., D. L. Cain, G. S. Levy et al. (1965), Occultation experiment: results of the first direct measurements of Mars atmospheres and ionospheres, *Science*, *149*, 1243.
- [50] Krymskii, A. M., T. K. Breus, N. F. Ness, M. H. Acuña, J. E. P. Connerney, D. H. Crider, D. L. Mitchell, and S. J. Bauer (2002), Structure of the magnetic field fluxes connected with crustal magnetization and topside ionosphere at Mars, *J. Geophys. Res.*, *107*(A9), 1245.
- [51] Krymskii, A. M., T. K. Breus, N. F. Ness, D. P. Hinson, and D. I. Bojkov (2003), Effect of crustal magnetic fields on the near terminator ionosphere at Mars: Comparison of in situ magnetic field measurements with the data of radio science experiments onboard Mars Global Surveyor, *J. Geophys. Res.*, *108*(A12), 1431.
- [52] Krymskii A. M., N. F. Ness, D. H. Crider, T. K. Breus, M. H. Acuña, D. P. Hinson (2004), Solar wind interaction with the ionosphere/atmosphere and crustal magnetic fields at Mars: Mars Global Surveyor Magnetometer/Electron Reflectometer, radio science, and accelerometer data, *J. Geophys. Res.*, *109*, A11306.
- [53] Liu, Y., A. F. Nagy, P. T. Clinton, D. L. Groth, L. DeZeeuw and T. I. Gombosi (1999), 3D multi-fluid MHD Studies of the Solar Wind Interaction with Mars, *Geophys. Res. Lett.*, *26*, 2689.
- [54] Liu, Y, A. F. Nagy, T. I. Gombosi, D. L. DeZeeuw and K. G. Powell (2001), The Solar Wind Interaction with Mars: Results of Three-dimensional Three-species MHD Studies, *Adv. Space Res.*, *27*, 1837.

- [55] Luhmann, J.G. and J.U. Kozyra (1991), Dayside Pickup Oxygen Ion Precipitation at Venus and Mars: Spatial Distributions, Energy Deposition, and Consequences, *J. Geophys. Res.*, *96*, 5457.
- [56] Luhmann, J. G. (1986), The solar wind interaction with Venus, *Space Sci. Rev.*, *44*, 241.
- [57] Luhmann, J. G, C. T. Russell, L. H. Brace, and O. L. Vaisberg (1992), The intrinsic magnetic field and solar wind interaction of Mars, in *MARS, University of Arizona Press*, edited by H. Kieffer, B. Jakosky, C. Snyder, M. Mathews, 1090.
- [58] Luhmann, J. G. and L. H. Brace (1991), Near-Mars space, *Rev. Geophys.*, *29*, 121.
- [59] Lundin, R. and E. M. Dubinin (1992), Phobos-2 Results on the Ionospheric Plasma Escape from Mars, *Adv. Space Res.*, *12*(9), 255.
- [60] Lundin, R. , E. M. Dubinin, H. Koskinen, O. Norberg, N. Pissarenko, and S. W. Barabash (1991), On the momentum transfer of the solar wind Martian topside ionosphere , *Geophys. Res. Lett.*, *18*(6), 1059.
- [61] Ma, Y., A. A. F. Nagy, K. C. Hansen, D. L. DeZeeuw, T. I. Gombosi and K. G. Powell (2002), 3D Multi-fluid MHD Studies of the Solar Wind Interaction with Mars in the Presence of Crustal Fields, *J. Geophys. Res.*, *107*.
- [62] Ma, Y., A. F. Nagy, I. V. Sokolov and K. C. Hansen (2004), 3D, Multispecies, High Spatial resolution MHD Studies of the Solar Wind Interaction with Mars, *J. Geophys. Res.*, *109*, A07211.
- [63] Marubashi, K., J. M. Grebowsky, H. A. Taylor et al. (1985), Magnetic Field in the Wake of Venus and the Formation of Ionospheric Holes, *J. Geophys. Res.*, *90*, 1385.

- [64] Mitchell, D. L., R. P. Pin, C. Mazelle, H. R'eme, P. A. Cloutier, J. E. P. Connerney, M. H. Acuña, and N. F. Ness (2001), Probing Mars' crustal magnetic field and ionosphere with the MGS Electron Reflectometer, *J. Geophys. Res.*, *106*(E10), 23,419-23,427.
- [65] Mozer, F. S., S. D. Bale, J. P. McFadden, and R. B. Torbert (2005), New features of electron diffusion regions observed at subsolar magnetic field reconnection sites, *Geophys. Res. Lett.*, *32*, 24102.
- [66] Nagy, A. F., D. Winterhalter, K. Sauer (2004), Plasma environment of Mars, *Space Sci. Rev.*, *111*, 33-114.
- [67] Ness, N. F., M. H. Acuña, J. E. P. Connerney, A. J. Kliore, T. K. Breus, A. M. Krymskii, P. Cloutier, and S. J. Bauer (2000a), Effects of magnetic anomalies discovered at Mars on the structure of the Martian ionosphere and solar wind interaction as follows from radio occultation experiments, *J. Geophys. Res.*, *105*(A7), 15,991-16,004.
- [68] Ness, N. F. et al. (2000b), Effects of Magnetic Anomalies Discovered at Mars on the Structure of the Martian Ionosphere and Solar Wind Interaction as Follows from Radio Occultation Experiment, *J. Geophys. Res.*, *105*, 15991.
- [69] Neugebauer, M., C. W. Snyder (1966), Mariner 2 Observations of the Solar Wind, Average Properties, *J. Geophys. Res.*, *71*, 4469.
- [70] Ong, M., J. Luhmann, C. Russell, R. Strangeway, and L. Brace (1991), Venus Ionospheric "Clouds": Relationship to the Magnetosheath Field Geometry, *J. Geophys. Res.*, *96*(A7), 11133-11144.
- [71] Parker, E. N. (1963), Interplanetary Dynamical Processes, *Wiley-Interscience*, New York.

- [72] Paschmann, G., B. U. O. Sonnerup, I. Papamastorakis, N. Sckopke, G. Haerendel, S. J. Bame, J. R. Asbridge, J. T. Gosling, C. T. Russell, R. C. Elphic (1979), Plasma acceleration at the Earth's magnetopause: Evidence for magnetic reconnection, *Nature*, *282*, 243-246.
- [73] Perez de Tejada H. (2000), Acceleration of ionospheric plasma clouds in the Venus ionosheath, *Planetary and Space Science*, *48*(9), 871-883(13).
- [74] Phillips, J. L. and D. J. McComas (1991), The magnetosheath and magnetotail of Venus, *Space Sci. Rev.*, *55*, 1-80.
- [75] Priest, E., and T. Forbes (2000), Magnetic Reconnection: MHD Theory and Applications, *Cambridge Univ. Press*, New York.
- [76] Purucker, M., D. Ravat, H. Frey, C. Voorhies, T. Sabaka, and M. Acuña (2000), An altitude normalized magnetic map of Mars and its interpretation, *Geophys. Res. Lett.*, *27*(16), 2449-2452.
- [77] Riedler, W., et al. (1989), Magnetic Fields Near Mars: First Results, *Nature*, *341*, 604.
- [78] Rosenbauer, H., N. Shutte, I. Apathy, A. Galeev, K. Gringauz, H. Gruenwaldt, P. Hemmerich, K. Jockers, P. Kiraly, G. Kotova, S. Livi, E. Marsh, A. Richter, W. Riedler, A. Remizov, R. Schwenn, K. Schwingenschuh, M. Steller, K. Szego, M. Verigin, and M. Witte (1989), Ions of martian origin and plasma sheet in the martian magnetotail: Initial results of TAUS experiment, *Nature*, *341*, 612.
- [79] Russell, C. T. and O. Vaisberg (1983), The interaction of the solar wind with Venus, *IN: Venus (A83-37401 17-91)*, University of Arizona Press, 873-940.
- [80] Russell, C.T., J. G. Luhmann, J. R. Spreiter et al. (1984), The magnetic field of Mars: implications from gas dynamic modeling, *J. Geophys. Res.*, *89*, 2997.

- [81] Russell, C. T. (1993), Planetary magnetospheres, *Rep. Prog. Phys.*, *56*, 687-732.
- [82] Schindler, K., M. Hesse, and J. Birn. (1988), General magnetic reconnection, parallel electric fields, and helicity, *J. Geophys. Res.*, *93*, 5547-5557.
- [83] Schunk, R. W. and A. F. Nagy (2000), Ionospheres, *Cambridge University Press*.
- [84] Schwingenschuh, K. et al. (1992), The Martian Magnetic Field Environment: Induced or Dominated by an Intrinsic Magnetic Field, *Adv. Space Res.*, *12*(9), 213.
- [85] Shinagawa, H., and S. W. Bougher (1999), A two-dimensional MHD model of the solar wind interaction with Mars, *Earth Planets Space*, *51*, 55.
- [86] Slavin, J. A., K. Schwingenschuh, W. Riedler, and Y. Yeroshenko (1991), The Solar Wind Interaction with Mars: Mariner 4, Mars 2, Mars 3, Mars 5 and Phobos 2 Observations of Bow Shock Position and Shape, *J. Geophys. Res.*, *96*, 11235.
- [87] Sonnerup, B. U. O (1979), Magnetic field reconnection, *Solar System Plasma Physics*, *3*, 47-108.
- [88] Soobiah, Y., et al. (2006), Observations of magnetic anomaly signatures in Mars Express ASPERA-3 ELS data, *Icarus*, *182*, 396-405.
- [89] Spreiter, J. R. and A. Y. Alksne (1969), Plasma flow around the magnetosphere, *Rev. Geophys.*, *7*, 11-50.
- [90] Spreiter, J. R. and S. S. Stahara (1992), Computer modeling of solar wind interaction with Venus and Mars, in *Venus and Mars: Atmospheres, Ionospheres and Solar Wind Interactions*, edited by J. Luhmann, M. Tatralay, and R. Pepin, *Geophys. Monogr. Ser.*, *66*, AGU, Washington, D. C.
- [91] Spreiter, J. R. and S. S. Stahara (1980), A New Predictive Model for Determining Solar Wind - Terrestrial Planet Interactions, *J. Geophys. Res.*, *85*(6), 769.

- [92] Tanaka, T. (1993), Configurations of the solar wind flow and magnetic field around the planets with no magnetic field: Calculation by a new MHD simulation scheme, *J. Geophys. Res.*, *98*, 17,251.
- [93] Tanaka, T., and K. Murawski (1997), Three-dimensional MHD simulation of the solar wind interaction with the ionosphere of Venus: Results of two-component reacting plasma simulation, *J. Geophys. Res.*, *102*(A9), 19,805.
- [94] Van Allen, J. A. and F. Bagenal (1999), The New Solar System. Edited by J. Kelly Beatty, Carolyn Collins Peterson, and Andrew Chaikin. Sky Publishing Corporation, Cambridge University Press, 39.
- [95] Verigin, M. I., K. I. Gringauz, N. M. Shutte, S. A. Haider, K. Szego, P. Kiraly, A. F. Nagy, and T. I. Gombosi (1991), On the possible source of the ionization in the nighttime Martian ionosphere: 1. PHOBOS 2 harp electron spectrometer measurements, *J. Geophys. Res.*, *96*, 19,307-19,313.
- [96] Verigin, M. I., et al. (1991), Ions of Planetary Origin in the Martian Magnetosphere (Phobos 2/Taus Experiment), *Planetary Space Sci.*, *39*, 131.
- [97] Verigin, M. I., K. I. Gringauz, G. A. Kotova, A. P. Remizov, N. M. Shutte, A. Richter, W. Riedler, K. Schwingenschuh, K. Szego, I. Apathy and M. Tatralay (1993), The Dependence of the Martian Magnetopause and Bow Shock on Solar-Wind Ram Pressure According to Phobos 2 TAUS Ion Spectrometer Measurements, *J. Geophys. Res.*, *98*, 1303.
- [98] Vignes, D., et al. (2000), The solar wind interaction with Mars: Locations and shapes of the Bow Shock and Magnetic Pile-up Boundary from the observations of the MAG/ER experiment onboard Mars Global Surveyor, *Geophys. Res. Lett.*, *27*, 49.

- [99] Vignes, D., M. H. Acuña, J. E. P. Connerney, D. H. Crider, H. Rème, and C. Mazelle (2002), Factors controlling the location of the Bow Shock at Mars, *Geophys. Res. Lett.*, 29(9), 1328.
- [100] Wallis, M. K, and A. D. Johnstone (1983), Implanted ions and the draped cometary field, *Cometary Exploration*, Budapest, Hungary, 307.
- [101] Yeroshenko, Y., W. Riedler, K. Schwingenschuh, J. G. Luhmann, M. Ong and C. T. Russell (1990), The Magnetotail of Mars: Phobos 2 Observations, *Geophys. Res. Lett.*, 17(6), 885-888.
- [102] Zhang, T., J. G. Luhmann, and C. T. Russell (1991), The Magnetic Barrier at Venus, *J. Geophys. Res.*, 96(A7), 11145-11153.